

# Cubic Polynomial Maps with Periodic Critical Orbit, Part III: Tessellations and Orbit Portraits

Araceli Bonifant and John Milnor

March 13, 2025

## Abstract

We study the parameter space  $\mathcal{S}_p$  for cubic polynomial maps with a marked critical point of period  $p$ . We will outline a fairly complete theory as to how the dynamics of the map  $F$  changes as we move around the parameter space  $\mathcal{S}_p$ . For every escape region  $\mathcal{E} \subset \mathcal{S}_p$ , every parameter ray in  $\mathcal{E}$  with rational parameter angle lands at some uniquely defined point in the boundary  $\partial\mathcal{E}$ . This landing point is necessarily either a parabolic map or a Misiurewicz map. The relationship between parameter rays and dynamic rays is formalized by the *period  $q$  tessellation* of  $\mathcal{S}_p$ , where maps in the same face of this tessellation always have the same period  $q$  orbit portrait.

## Contents

1	Introduction	2
2	Dynamic Rays and Parameter Rays	3
3	Tessellations and Orbit Portraits.	25
4	Around a Parabolic Point	58
5	Counting	85
6	Misiurewicz Maps and Similarity	92
A	Parabolic Landing Stability (in some cases)	95
B	Embedded Trees	99

**Keywords:** cubic polynomials, parameter rays, tessellations, dynamic rays, Misiurewicz maps, parabolic maps, escape region, wake, primary edge, secondary edge, orbit portraits.

**Mathematics Subject Classification (2020):** 37F10, 30C10, 30D05.

# 1 Introduction

Let  $\mathcal{S}_p$  be the space of all monic centered cubic polynomial maps  $F$  with a **marked critical point**  $a = a_F$  of period  $p \geq 1$ . If  $v = F(a)$  is the corresponding critical value, then we obtain the normal form

$$F(z) = F_{a,v}(z) = z^3 - 3a^2z + (2a^3 + v). \quad (1)$$

It will be convenient to identify  $\mathcal{S}_p$  with the smooth affine curve consisting of all pairs  $(a, v) \in \mathbb{C}^2$  such that  $a$  has period exactly  $p$  under iteration of  $F$ . Compare Parts I and II of this paper ([M4] and [BKM]). In other words, we identify the map  $F = F_{a,v} \in \mathcal{S}_p$  with the pair  $(a, v) \in \mathbb{C}^2$ . Each  $\mathcal{S}_p$  is connected (see [AK]), and consists of a compact connected **connectedness locus**, together with a finite number of **escape regions**, each conformally isomorphic to a punctured disk. The genus of  $\mathcal{S}_p$  (or of the smoothly compactified curve  $\overline{\mathcal{S}}_p$ ) grows quite rapidly with  $p$ . (Compare §5.)

This paper will outline a fairly complete theory as to how the dynamics of the map  $F$  changes as we move around the parameter space  $\mathcal{S}_p$ . However there are many questions that we have been unable to answer: We will be grateful for any comments or suggestions.

Here is a brief description of what follows. Section 2 contains many definitions and basic properties. It first describes **dynamic rays**, which lie in the complement of the filled Julia set of a map in  $\mathcal{S}_p$ , and **parameter rays**, which lie in the various escape regions of  $\mathcal{S}_p$ . In particular, it shows that every parameter ray with a rational parameter angle lands at a map which is either parabolic or Misiurewicz depending on whether its angle is **co-periodic** or not (See Definition 2.4 and Theorem 2.7). The **kneading invariant** of an escape region is described in Definition 2.20 through Remark 2.23. Hyperbolic components are discussed in Remark 2.26. Copies of the quadratic Mandelbrot set in parameter space in Remark 2.21, some basic conjectures and questions in Remarks 2.28 and 2.29. The section concludes with a discussion of **dual** critically periodic points in Remark 2.30.

Section 3 describes a dynamically useful tessellation  $\mathbf{Tes}_q(\overline{\mathcal{S}}_p)$  of the smoothly compactified parameter curve  $\overline{\mathcal{S}}_p$ . Here  $p$  and  $q$  can be any positive integers. The **edges** of this tessellation are the parameter rays of co-period  $q$ , leading from an **ideal vertex** to a **parabolic vertex**. Each face  $\mathcal{F}$  of the tessellation determines a period  $q$  **orbit portrait** which describes which dynamic rays of period  $q$  land at the same point of the Julia set for maps in  $\mathcal{F}$ . There is a basic distinction between three different kinds of edge: As we cross a **primary edge** the change in orbit portrait is strictly monotonic, so that the orbit portrait on one side is a proper subset of the orbit portrait on the other side. In the case of a **secondary edge** the change is strictly non-monotonic, so that neither orbit portrait contains the other. Finally, for an **inactive edge**, there is no change in orbit portrait. (Conjecturally the inactive edges are precisely the **dead end edges**, with no other edge sharing the same parabolic landing point.) See Definition 3.24, Theorem 3.26 and Conjecture 3.27. We give a detailed study of just how the orbit portrait changes as we cross an edge of the tessellation. The concept of wake is closely related. A hyperbolic component  $H$  of Type D has a **wake**  $W$  if  $H$  is contained in a simply connected open set  $W \subset \mathcal{S}_p$ , which is bounded by two parameter rays which land at a parabolic boundary point of  $H$ , and which lie in the same escape region. (See Definition 3.17.)

Section 4 provides a description of how the period  $q$  orbit portrait changes as we circle around a parabolic vertex  $\mathfrak{p}$  of  $\mathbf{Tes}_q(\overline{\mathcal{S}}_p)$ . There are three cases to consider, according as the number of parameter rays landing at  $\mathfrak{p}$  is two, three, or four. (There is no change in the orbit portrait if there is only one ray landing; and conjecturally there are no cases with more than four rays landing.) We distinguish between *background relations* which hold for every map close to  $\mathfrak{p}$  and *distinguishing relations* which hold only for some maps near  $\mathfrak{p}$ . In all of the cases we have seen, the distinguishing relations are completely determined by the angles of the parameter rays landing at  $\mathfrak{p}$ . In the four ray case, we discuss rabbit and non-rabbit examples. (See Remark 4.11.)

Section 5 counts the number of vertices, edges, and faces in each tessellation  $\mathbf{Tes}_q(\overline{\mathcal{S}}_p)$ . We give explicit formulas for the number of edges, and (conjecturally at least) for the number of parabolic vertices. We also give a formula for the number of type B components of the curve  $\mathcal{S}_p$ . (See Theorem 5.4.)

Section 6 provides a more detailed description of the Misiurewicz case with special emphasis in Tan Lei similarity in Conjecture 6.1.

Appendix A proves a stability theorem for the landing of parameter rays as we approach a suitably restricted parabolic limit.

Appendix B describes weak Hubbard trees.

The exposition will be continued in Part IV of this paper (see [BM]).

**Acknowledgments:** We are grateful to Jan Kiwi for very useful comments, and to Scott Sutherland for help with many problems. Some of the exploration in this paper was done with the program Dynamics Explorer from Source Forge <https://sourceforge.net/u/bwboyd/profile/>. We are thankful to Suzanne and Brian Boyd for helping us to adapt some of our programs to their Dynamics Explorer platform.

## 2 Dynamic Rays and Parameter Rays

The theory of *dynamic rays*  $\mathcal{R}$  in the basin of infinity  $\mathbb{C} \setminus K(F)$  for a monic polynomial map  $F$  is classical and well understood. (Here  $K(F)$  denotes the filled Julia set of  $F$ .) In particular, each dynamic ray is an orthogonal trajectory to the family of equipotentials  $\mathbf{g}_F(z) = \text{constant}$ . Here  $\mathbf{g}_F : \mathbb{C} \rightarrow \mathbb{R}$  is the associated dynamic Green's function, defined by

$$\mathbf{g}_F(z) = \lim_{n \rightarrow \infty} \frac{1}{d^n} \log^+ |F^{on}(z)| ,$$

where  $d \geq 2$  is the degree of  $F$ . Each such ray  $\mathcal{R}$  has a well defined angle  $\theta \in \mathbb{R}/\mathbb{Z}$ . If  $\theta$  is rational, then the ray will land at a well defined point of the Julia set  $\partial K(F)$ ; unless it crashes into a critical or precritical point of  $F$ . (See Remark 2.3.)

More explicitly, we can label these rays, using the *Böttcher coordinate*  $\mathfrak{B}_F(z) \in \mathbb{C} \setminus \overline{\mathbb{D}}$ , which is well defined, for  $z$  large, with

$$\mathfrak{B}_F(F(z)) = \mathfrak{B}_F(z)^d, \quad \text{and with} \quad \mathfrak{B}_F(z) = z + O(1/z) \quad \text{as} \quad |z| \rightarrow \infty .$$

Then

$$\mathbf{g}_F(z) = \log |\mathfrak{B}_F(z)|$$

for any  $z$  in the region where  $\mathfrak{B}_F$  is defined (See [M3, Definition 9.6]). The unique dynamic ray through  $z$  can then be labeled as  $\mathcal{R}_F(\theta) \subset \mathbb{C} \setminus K(F)$ , where  $\theta \in \mathbb{R}/\mathbb{Z}$  is the argument of the complex number  $\mathfrak{B}_F(z)$  and  $K(F)$  is the Julia set. Note that

$$F(\mathcal{R}_F(\theta)) = \mathcal{R}_F(d\theta).$$

Each dynamic ray  $\mathcal{R}_F(\theta)$  can be parametrized by the Green's function  $\mathbf{g}(z)$ .

If the Julia set is connected, the Böttcher coordinate maps the complement  $\mathbb{C} \setminus K(F)$  holomorphically onto the region  $|\mathfrak{B}_F(z)| > 1$ ; and every ray can be described as a function

$$\mathbf{g} \mapsto \mathbf{r}(\mathbf{g}) = \mathbf{r}_{F,\theta}(\mathbf{g}) \tag{2}$$

which is defined and real analytic as a function of the three variables:  $F$  in parameter space,  $\theta \in \mathbb{R}/\mathbb{Z}$ , and  $\mathbf{g} \in (0, +\infty)$ . Furthermore, each ray tends to infinity in  $\mathbb{C}$  as  $\mathbf{g} \rightarrow \infty$ , and tends to the Julia set as  $\mathbf{g} \rightarrow 0$ .

On the other hand, the theory of parameter rays in the parameter space  $\mathcal{S}_p$  has some special features that require explanation. Each  $\mathcal{S}_p$  has some finite number of *escape regions*  $\mathcal{E}_h$  consisting of maps  $F$  such that the free critical point  $-a$  has unbounded orbit. The complement  $\mathcal{S}_p \setminus \bigcup_h \mathcal{E}_h$  is the *connectedness locus*, which is compact and connected and consists of those maps which have connected Julia set. Each  $\mathcal{E}_h$  is conformally isomorphic to the punctured open disk  $\mathbb{D} \setminus \{0\}$ . Concentric circles in  $\mathbb{D}$  correspond to *equipotentials*, where the parameter Green's function

$$\mathbf{G}(F) = \mathbf{g}_F(2a_F) = \log |\mathfrak{B}(2a_F)| = \lim_{n \rightarrow \infty} \frac{1}{3^n} \log^+ |F^{\circ n}(-a)|$$

takes some constant value (see [M3, Definition 9.6]). The orthogonal trajectories of these equipotentials, corresponding to radial line segments in the disk, are called *parameter rays*  $\mathfrak{R}$  in  $\mathcal{E}_h$ . The angle  $\theta$  of the dynamic ray passing through  $2a$  is called the *co-critical angle* of  $F$ .

**Remark 2.1 (Multiplicity of an Escape Region).** In general, a parameter ray is not uniquely determined by its parameter angle. Each escape region  $\mathcal{E}_h$  has a well defined multiplicity  $\mu_h \geq 1$ ; and each parameter angle corresponds to  $\mu_h$  different parameter rays, which are evenly spaced around the region. (Compare [BKM] where it is shown that  $\mu_h$  is always a power of two.) Most of the escape regions we discuss explicitly have multiplicity  $\mu_h = 1$ . In particular, if  $p \leq 3$  then every escape region in  $\mathcal{S}_p$  has multiplicity one.

However, when  $p \geq 4$ , there are certainly escape regions with multiplicity  $\mu > 1$ . Here is an example: According to [BKM, Table 6.4] there are two escape regions in  $\mathcal{S}_4$  with kneading invariant  $(0, 0, 1, 0)$  (see Definition 2.20 below); and each of these has multiplicity two. (The two are 180 degree rotations of each other.) A careful study of Figure 11 of [BKM] shows that each of these two regions is surrounded by a circle of 26 neighboring escape regions, most of which have multiplicity one. For each parameter ray in one of these two regions there is another ray with the same angle. Two such rays usually land near quite different escape regions, so there is presumably no close relationship between the two landing points.

More explicitly (see [BKM]), in the case  $\mu > 1$  we will need a conformal isomorphism

$$\mathcal{E}_h \xrightarrow{\cong} \mathbb{C} \setminus \overline{\mathbb{D}}$$

given by choosing a smooth branch  $F \mapsto \sqrt[\mu]{\mathfrak{B}_F(2a_F)}$  of the  $\mu$ th-root of the Böttcher coordinate  $\mathfrak{B}_F$  evaluated at  $2a = 2a_F$ . The choice of the  $\mu$ -root is called an **anchoring** of the escape region  $\mathcal{E}_h$ . We then define **parameter angle**  $\phi(F)$  as

$$\phi(F) = \arg\left(\sqrt[\mu]{\mathfrak{B}_F(2a_F)}\right) \in \mathbb{R}/\mathbb{Z}.$$

This angle  $\phi(F)$ , measured in the escape region  $\mathcal{E}_h$ , is simply a label with no invariant dynamical meaning, since it depends on the choice of anchoring. However the **co-critical angle**

$$\theta(F) = \arg(\mathfrak{B}_F(2a_F)) \in \mathbb{R}/\mathbb{Z},$$

measured in the dynamical plane, is invariantly defined, and is related to the parameter angle by the equation

$$\theta(F) = \mu \phi(F). \quad (3)$$

Of course in the special case  $\mu = 1$ , the parameter angle can be identified with the co-critical angle.

**Definition 2.2.** For any specified angle  $\phi_0$ , the set consisting of all  $F \in \mathcal{E}_h$  with parameter angle  $\phi(F) = \phi_0$ , is called a **parameter ray**  $\mathfrak{R}_{\mathcal{E}_h}(\phi_0)$ . Note that

$$F \in \mathfrak{R}_{\mathcal{E}_h}(\phi) \implies 2a_F \in \mathcal{R}_F(\mu\phi) = \mathcal{R}_F(\theta). \quad (4)$$

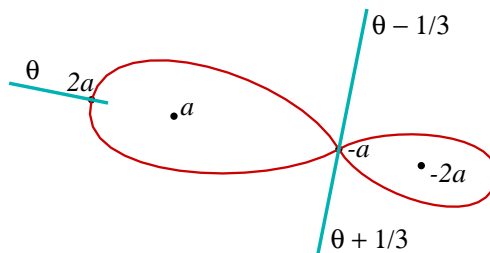


Figure 1: Sketch of the dynamic plane for a map  $F$  which lies on a parameter ray of angle  $\theta$  in some escape region  $\mathcal{E}_h$ . Here  $a = a_F$  is the marked (periodic) critical point;  $-a$  is the free critical point; and the figure eight curve represents the equipotential  $\mathbf{g}_F(z) = \text{constant} = \mathbf{g}_F(-a) = \mathbf{g}_F(2a)$ . Note that the two **co-critical points**  $2a$  and  $-2a$  satisfy  $F(2a) = F(-a)$  and  $F(-2a) = F(a)$ . The filled Julia set  $K(F)$  is the disjoint union of parts in the left lobe and parts in the right lobe; and hence is not connected. Since some neighborhood of  $2a$  maps bijectively outside the figure eight curve, the dynamic  $\theta$  ray for  $F$  extends smoothly at least a little past  $2a$ .

(Compare Figure 1.) Note that the parameter angle remains constant as  $F$  varies along any parameter ray. In fact our parameter rays are special cases of stretching rays,

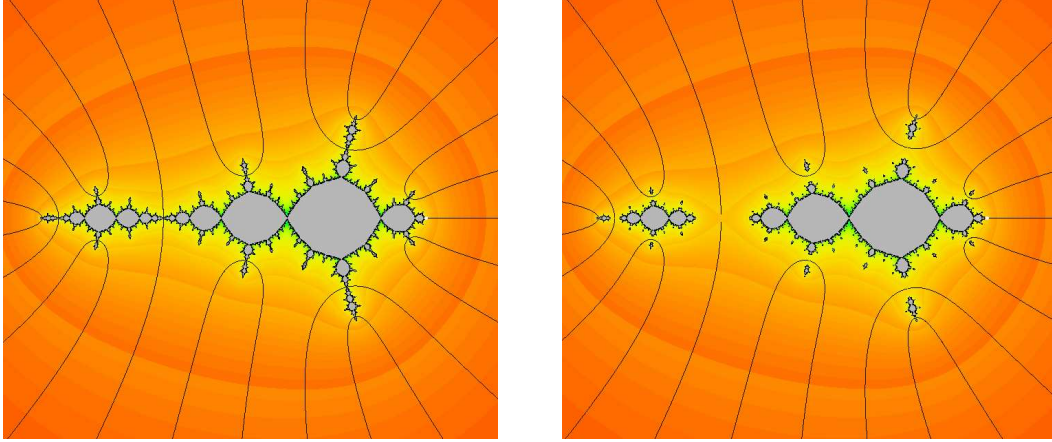


Figure 2: On the left, the Julia set for the landing map  $F_0$  of the zero parameter ray in the “basilica” escape region of  $\mathcal{S}_2$ . The dynamic rays of angle  $n/27$  are shown. On the right, the Julia set for a map  $F$  on the zero parameter ray for this basilica region.

as defined by Branner and Hubbard [BH1]. The different maps along a stretching ray are quasi-conformally conjugate, under a conjugacy which multiplies the Green’s function by a constant, but preserves the dynamic angle.

**Remark 2.3 (Disconnected Julia Sets).** In any escape region, we are dealing with Julia sets which are not connected, so we have to be careful in the discussion of dynamic rays. As we follow a dynamic ray from infinity, it will remain smooth and well defined as long as we are outside the figure eight equipotential curve. But two rays crash together at  $-a$  (as illustrated in Figure 1). Furthermore,  $-a$  has countably many iterated pre-images inside the figure eight, and in many cases two rays will crash together at each of these. (Compare Figure 2 for many examples of this.) However, there are also cases where only one ray crashes at a pre-critical point. (Compare Figure 7-right for two examples of such “dead end” rays.) Note that the set of all pre-critical points converges to the filled Julia set in the following sense: Given any neighborhood  $N$  of  $K(F)$ , there are only finitely many pre-critical points outside of  $N$ .

These critical and precritical points are precisely the critical points of the Green’s function in  $\mathbb{C} \setminus K(F)$ . It is often convenient to parametrize each dynamic ray as a smooth function  $\mathbf{g} \mapsto \mathbf{r}(\mathbf{g})$  of the Green’s function. For a generic choice of ray, this function  $\mathbf{r}(\mathbf{g})$  is defined for all  $\mathbf{g} > 0$ . However in the countably many exceptional cases where the ray crashes into a critical or precritical point  $z_0$ , the function  $\mathbf{r}(\mathbf{g})$  is defined only for  $\mathbf{g} > \mathbf{g}(z_0)$ . Note that  $\mathbf{r}(\mathbf{g})$  can be considered as a real analytic function, not only of  $\mathbf{g}$ , but also of the map  $F \in \mathcal{S}_p$  and of the dynamic angle  $\phi$ , throughout the interior of the region where it is defined.

Another key idea is the following.

**Definition 2.4 (Co-periodic Angles).** An angle  $\theta \in \mathbb{R}/\mathbb{Z}$  will be called *co-periodic* of *co-period*  $q \geq 1$  if either  $\theta + 1/3$  or  $\theta - 1/3$  is periodic of period  $q$  under angle tripling. The elements of the associated periodic orbit can be listed as

$$\{\theta_1, \theta_2, \dots, \theta_q\} \quad \text{where} \quad \theta_j = 3^j \theta \quad \text{for} \quad 1 \leq j \leq q. \quad (5)$$

Thus  $\theta_1 \mapsto \theta_2 \mapsto \cdots \mapsto \theta_q \mapsto \theta_1$  under angle tripling. In other words, if we think of  $j$  as a residue class modulo  $q$ , then  $\theta_{j+1} = 3\theta_j$  in all cases. Here  $\theta_q$  is always equal to  $\theta \pm 1/3$  for some choice of sign.

It will be convenient to use the term **triad** for any triple of angles  $(\theta, \theta_q, \widehat{\theta})$ , such that both  $\theta$  and  $\widehat{\theta} = \theta \mp 1/3$  are co-periodic, while  $\theta_q = 3^q\theta = 3^q\widehat{\theta}$  is periodic. Thus the three angles  $\theta, \theta_q$  and  $\widehat{\theta}$  are evenly spaced around the circle, and all three map to  $\theta_1$  under tripling. However  $\theta_q$  is the only one of the three which is periodic. We will describe the two co-periodic angles in a triad (or the associated dynamics rays) as **twin co-periodic angles** (or **twin rays**).

If  $F$  is a map belonging to a parameter ray  $\mathfrak{R}$  of angle  $\theta$  in some escape region, then in the dynamic plane for  $F$  the rays of angle  $\theta_q$  and  $\widehat{\theta}$  will crash together at the escaping critical point  $-a$ , while the dynamic ray of angle  $\theta$  will pass through the co-critical point  $2a$ . (Compare Figure 1.) But note that  $\theta$  is not uniquely determined by the  $\theta_j$ . In fact the correspondence  $\theta \mapsto \theta_1$  is two-to-one. (Compare Lemma 4.1.)

**Remark 2.5 (Notational convention).** The smallest common denominator for angles of period  $q$  under tripling will be denoted by

$$d = d(q) = 3^q - 1.$$

In fact the angles of the form  $\theta = m/d$  where  $m$  is an integer modulo  $d = d(q)$  are precisely those which satisfy  $3^q\theta \equiv \theta$  modulo  $\mathbb{Z}$ . Similarly every angle  $\theta$  of co-period  $q$  can be written as a fraction of the form  $\theta = m/(3d)$ . Here two conditions must be satisfied:

- (1)  $m$  must be congruent to either one or two modulo three, and
- (2) it must not be possible to write  $\theta$  in this form for any smaller value of  $q$ .

(As an example, it might seem that  $\frac{13}{3d(3)}$  has co-period three. However the computation

$$\frac{13}{3d(3)} = \frac{13}{78} = \frac{1}{6} = \frac{1}{3d(1)}$$

shows that it actually has co-period one.)

It is not hard to check that a fraction  $0 < m/n < 1$  in lowest terms is co-periodic of some co-period if and only if  $n$  is divisible by three but not by nine.

**Definition 2.6 (Parabolic Maps and Misiurewicz Maps).** A map  $F \in \mathcal{S}_p$  will be called **parabolic** if it has a (necessarily unique) parabolic orbit. The **ray period**  $q$  of a parabolic map is the period of any dynamic ray which lands at a parabolic point. This is always equal to the period of the cycle of parabolic basins; but it may be a multiple of the period of the parabolic point itself. (Compare [M3, Thm. 18.13].)

Imitating the terminology of Douady and Hubbard for quadratic maps, we will say that  $F$  is a **Misiurewicz map** if the orbit of the free critical point  $-a_F$  is eventually periodic repelling.

**Note.** For simplicity in the exposition from now on we will assume that  $\mu = 1$ , and denote by  $\theta$  the angle corresponding to both, the parameter ray  $\mathfrak{R}(\phi)$  and dynamical ray  $\mathcal{R}(\theta)$ . The reader should be aware that when dealing with an escape region of multiplicity  $\mu > 1$  adjustments should be made according to equation (3).

**Theorem 2.7 (Landing Theorem).** *Every parameter ray  $\mathfrak{R}$  with rational parameter angle  $\theta$  lands at a uniquely defined map  $F = F_{\mathfrak{R}}$  which belongs to the boundary of its escape region in  $\mathcal{S}_p$ . There two possible cases:*

**Case 1: Parabolic Maps.** *If the angle  $\theta$  is co-periodic of co-period  $q$ , then the free critical orbit for  $F_{\mathfrak{R}}$  converges to a parabolic orbit of ray period  $q$ . (For a more detailed description, see Lemma 2.16, and for examples, see Figures 3 and 9 as well as Figures 22 and 23.)*

**Case 2: Misiurewicz Maps.** *If  $\theta$  is rational but not co-periodic, then the free critical orbit for  $F_{\mathfrak{R}}$  is eventually periodic repelling. In this case the dynamic  $\theta$  ray lands at the co-critical point  $2a$ ; and the non-periodic rays of angle  $\theta \pm 1/3$  both land at  $-a$ . (Compare Figures 5 and 29.) As a special case, if the angle  $\theta$  is actually periodic, then it is not co-periodic, and  $2a$  itself is a repelling periodic point. (Compare Figure 6.)*

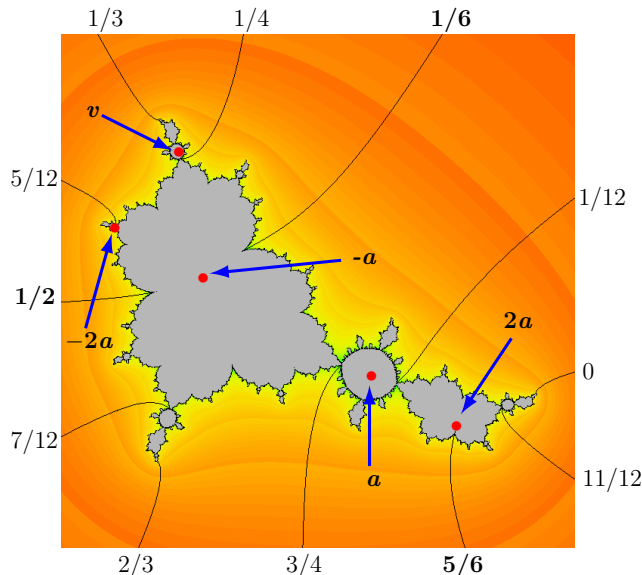


Figure 3: A parabolic example with ray period one: Julia set for the landing map of the  $5/6$  parameter ray in the inner escape region  $\mathcal{E}_{\text{in}}$  of  $\mathcal{S}_2$ . Here the dynamic rays of angle  $5/6 + 1/3 = 1/6$  and  $5/6 - 1/3 = 1/2$  land on the boundary of the fixed parabolic component, with the  $1/2$  ray landing at the parabolic fixed point. (See Figure 15 lower-left for the  $5/6$  ray in parameter space.) In this example we have period  $q = 1$ , so that the critical basin  $U(-a)$  is equal to the critical value basin  $U(v')$ .

(Compare [AK, §5].) The proof of Theorem 2.7 begins as follows.

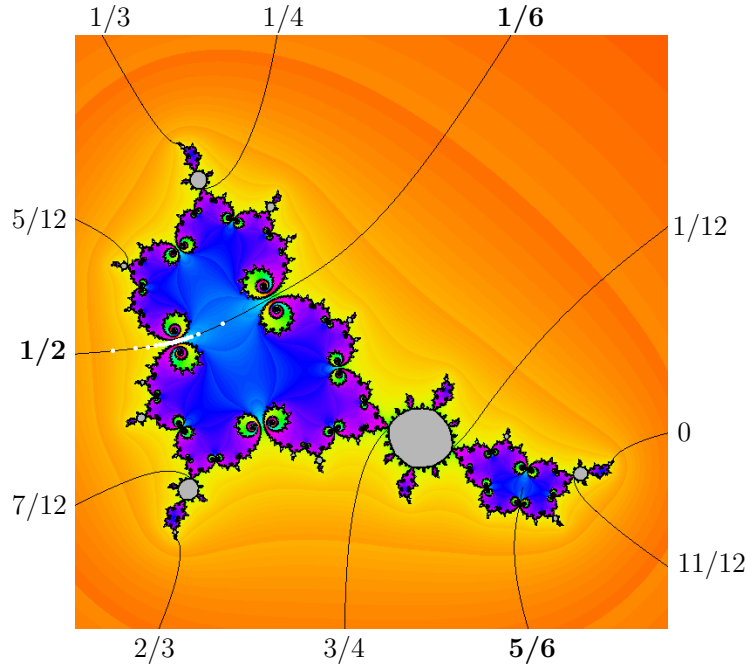


Figure 4: Modified version of Figure 3 showing the Julia set for a map belonging to the parameter ray of angle  $5/6$  in the inner escape region of Figure 15. The dynamic rays of angle  $\theta - 1/3 = 1/2$  and  $\theta + 1/3 \equiv 1/6$  now crash together at the free critical point  $-a$ ; while the  $5/6$  ray passes through  $2a$ . The first 22 forward images of  $-a$  are marked by white dots, lying on the  $(1/2)$ -ray. (Most of these dots are jammed close together since the orbit escapes very slowly through the narrow channel between two repelling fixed points.)

**Lemma 2.8 (Preliminary Landing Statement).** *Every parameter ray  $\mathfrak{R} \subset \mathcal{E}_h$  with rational parameter angle  $\theta$  lands at a well defined map  $F_{\mathfrak{R}}$  in the boundary  $\partial\mathcal{E}_h$  which is either parabolic or Misiurewicz. Furthermore, in the Misiurewicz case, the  $\theta$  dynamic ray lands at  $2a$ , and the two rays of angle  $\theta \pm 1/3$  land at  $-a$ .*

Note that these statements depend only on the angle of the parameter ray, and not on which particular escape region it is contained in.

The proof of this lemma will make use of the following.

**Lemma 2.9 (Landing stability for repelling points (Douady-Hubbard)).** *For  $f_0$  in the space of monic polynomial maps of some fixed degree  $n \geq 2$ , suppose that the periodic dynamic ray  $\mathcal{R}_{f_0}(\theta)$  lands on a repelling periodic point  $z_0$  of the Julia set. Then for all  $f$  in a neighborhood of  $f_0$  the corresponding ray  $\mathcal{R}_f(\theta)$  lands on a repelling point which depends holomorphically on  $f$ . Furthermore, the entire ray  $\mathcal{R}_f$  converges uniformly to  $\mathcal{R}_{f_0}$  (using the standard parametrization by the Green's function) as  $f$  tends to  $f_0$ .*

See for example [DH1, Prop. 8.5]. This contrasts with the behavior at a parabolic landing point. (Compare the Appendix.)

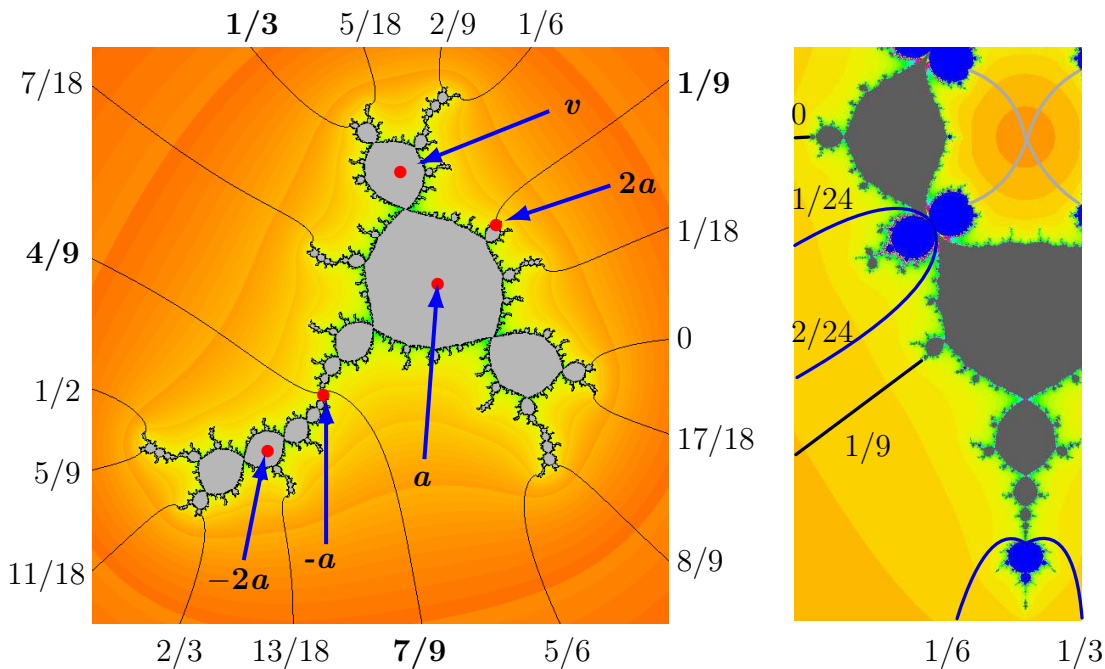


Figure 5: A Misiurewicz example. On the left, Julia set for the landing map of the  $1/9$  parameter ray in the outer (basilica) escape region  $\mathcal{E}_{\text{out}}$  of  $\mathcal{S}_2$ . Note that the dynamical  $1/9$  ray lands at the co-critical point, which is eventually periodic repelling since  $1/9 \mapsto 1/3 \mapsto 0 \pmod{\mathbb{Z}}$ . The two dynamic rays of angles  $1/9 \pm 1/3$  land on the free critical point  $-a$ . The  $1/9$  parameter ray is shown in the figure on the right. Note that  $1/9$  is not co-periodic. (Some co-periodic rays are also shown. Compare Figures 15 and 17 in Section 3.) Here the landing point of the  $1/9$  dynamic ray looks very much like the landing point of the  $1/9$  parameter ray. An analogous statement seems to be true in all Misiurewicz cases. Compare the discussion of **Tan Lei similarity** in Conjecture 6.1. For the coloring of parameter space pictures, see Remark 2.26; and for the choice of local coordinates in  $\mathcal{S}_p$  see [BKM, Sec.2].

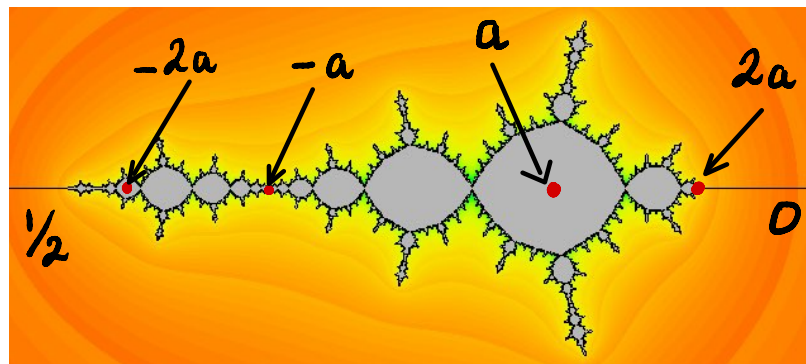


Figure 6: A simpler Misiurewicz example: Julia set for the landing point of the zero parameter ray in the outer escape region of  $\mathcal{S}_2$ . Here the free critical point  $-a$  maps directly to the repelling fixed point  $2a$ , the landing point of the  $\theta = 0$  ray. As in the previous figure, the landing point of the  $\theta$  ray in the dynamic plane looks much like the corresponding landing point in parameter space. (Again see Figure 15).

**Proof of Lemma 2.8.** The parameter ray  $\mathfrak{R}$  must have at least one accumulation point  $\widehat{F}$  in the boundary  $\partial\mathcal{E}_h$ . Since the parameter angle  $\theta$  is rational, and since  $\widehat{F}$  belongs to the connectedness locus, the associated dynamical ray  $\mathcal{R}_{\widehat{F}}(\theta)$  lands at some periodic or pre-periodic point  $z_0(\widehat{F})$  in the Julia set  $J(\widehat{F})$ . In fact, if we choose a multiple  $3^k\theta$  which is periodic under angle tripling, then the dynamic ray  $\widehat{F}^{\circ k}(\mathcal{R})$  will land at a periodic point  $z_k(\widehat{F}) = \widehat{F}^{\circ k}(z_0(\widehat{F}))$  which is either parabolic or repelling. (See for example [M3, §18.10].) If  $z_k(\widehat{F})$  is a parabolic point, then the map  $\widehat{F}$  is parabolic by definition.

On the other hand, suppose that this periodic point  $z_k(\widehat{F})$  is repelling, then we will prove that the landing point  $z_0(\widehat{F})$  is equal to the co-critical point  $2a = 2a_{\widehat{F}}$ , so that  $\widehat{F}$  is Misiurewicz. Let  $F$  vary over a small neighborhood of  $\widehat{F}$  in  $\mathcal{S}_p$ . By Lemma 2.9, the entire dynamical ray  $\mathcal{R}_F(\theta)$  will vary continuously with  $F$ . In particular, its landing point  $z_0(F)$  will vary continuously. If we choose  $F$  to lie on the parameter ray  $\mathfrak{R}_{\mathcal{E}_h}(\theta)$ , then the co-critical point  $2a_F$  will lie on this dynamical ray  $\mathcal{R}_F(\theta)$ . (Compare Figure 1.) Choose a sequence of maps  $F_j$  tending to  $\widehat{F}$  and all belonging to the parameter ray  $\mathfrak{R}_{\mathcal{E}_h}(\theta)$ , recall from Lemma 2.9 that the dynamic ray  $\mathcal{R}_{F_j}(\theta)$  converges uniformly to  $\mathcal{R}_{\widehat{F}}(\theta)$ , when these rays are parametrized by the respective Green's functions, the Green's function  $\mathbf{g}_{F_j}(2a_{F_j})$  will tend to  $\mathbf{g}_{\widehat{F}}(2a_{\widehat{F}}) = 0$ , hence the distance between  $2a_{F_j}$  and the landing point  $z_0(F_j)$  must tend to zero. Taking the limit as  $F_j$  tends to  $\widehat{F}$ , it follows that  $2a_{\widehat{F}}$  must be precisely equal to the landing point  $z_0(\widehat{F})$ , which is eventually periodic repelling. Since  $\widehat{F}(2a)$  is always equal to the critical value  $\widehat{F}(-a)$ , this proves that  $\widehat{F}$  is Misiurewicz. (Here we are only concerned with the orbit of  $-a$ , since the critical point  $a$  has finite periodic orbit by definition.)

Thus every accumulation point for the ray  $\mathfrak{R}$  in the boundary  $\partial\mathcal{E}_h$  must be either Misiurewicz or parabolic. Since the set of critically finite maps in  $\mathcal{S}_p$  is a countable union of zero-dimensional algebraic subvarieties, it is a countable set; and similarly the set of parabolic maps is countable. But the set of all accumulation points of a parameter ray in  $\partial\mathcal{E}_h$  is necessarily a connected set, hence it must consist of a single map  $F_{\mathfrak{R}}$ . This proves Lemma 2.8.  $\square$

### Proof of the Landing Theorem 2.7.

**Step 1.** Suppose that the parameter angle  $\theta$  is co-periodic. If the landing map  $F_{\mathfrak{R}}$  were Misiurewicz, then by Lemma 2.8 the dynamic ray of angle  $\theta$  for  $F_{\mathfrak{R}}$  would land on the co-critical point  $2a$ . Therefore the ray of angle  $3\theta$  which is periodic would land on the critical value  $F_{\mathfrak{R}}(2a) = F_{\mathfrak{R}}(-a)$ . Thus both critical orbits would be periodic; hence  $F_{\mathfrak{R}}$  would be in the interior of the connectedness locus. This is impossible since the landing point must be a boundary point of the connectedness locus. Thus  $F_{\mathfrak{R}}$  must be a parabolic map. It then follows from the work of Fatou and Julia that the orbit of at least one critical point (which can only be  $-a$ ) must converge to the parabolic orbit.

**Step 2.** We must prove the following statement:

**Lemma 2.10.** *If the landing map  $F_{\mathfrak{R}}$  is parabolic, with a parabolic basin of period  $q$ , then the parameter angle  $\theta$  for  $\mathfrak{R}$  must be co-periodic of co-period  $q$ . Furthermore, for any map*

$F$  on the ray  $\mathfrak{R}$ , the entire orbit of the free critical point under  $F^{\circ q}$  must be contained in a dynamic ray of period  $q$ , with angle either  $\theta + 1/3$  or  $\theta - 1/3$ .

We will need the following.

**Definition 2.11 (The Root Point of a Parabolic Basin).** Given a cycle of  $q$  parabolic basins, the parabolic map  $F^{\circ q}$  sends each basin to itself with degree two. Hence the boundary of each basin contains a unique fixed point of  $F^{\circ q}$ , called its **root point**. These root points form a parabolic orbit of some period  $k$  which divides  $q$ . In the case where  $k$  is less than  $q$ , note that each such root point will be shared between  $q/k$  different basin boundaries.

**Proof of Lemma 2.10.** Let  $U$  be the parabolic basin for  $F_{\mathfrak{R}}$  which contains the free critical point  $-a$ , and let  $q \geq 1$  be the period of this basin, so that  $F_{\mathfrak{R}}^{\circ q}$  maps  $U$  onto itself with degree two.

To simplify the discussion, we will first consider the special case  $q = 1$ , so that  $U = F_{\mathfrak{R}}(U)$ . Thus the orbit of  $-a$  under  $F_{\mathfrak{R}}$  will converge to the parabolic root point. (Compare Figure 7-left.) If we approximate this landing map by a nearby map  $F$  on the ray  $\mathfrak{R}$ , then the orbit of  $-a$  under  $F$  will pass through a narrow “escape channel” near the former parabolic point, and then diverge towards infinity. If the parameter angle is  $\theta$ , recall that the two dynamic rays of angle  $\theta \pm 1/3$  must crash together at the free critical point (Figure 7-right).

We want to prove that  $F$  must map one of these two crashing rays into itself. This will prove that  $\theta$  is co-periodic. Furthermore, since the  $F$ -invariant ray contains the free critical point, it will prove that this ray contains the entire free critical orbit.

Suppose to the contrary that neither crashing ray maps to itself under  $F$ . Since both of the angles  $\theta \pm 1/3$  map to  $3\theta$  under tripling, it follows that the ray of angle  $3\theta$  must land at  $F(-a)$ . Similarly for each  $k > 0$  the ray of angle  $3^k$  will land at  $F^{\circ k}(-a)$ . But every rational angle is eventually periodic under tripling, so this contradicts the hypothesis that  $-a$  eventually escapes to infinity. This proves the Lemma in the case  $q = 1$ .

If the parabolic basin has period  $q > 1$ , then we can apply an analogous argument to the iterate  $F^{\circ q}$  of degree  $3^q$ . Details are straightforward, and will be left to the reader. This completes the proof of Lemma 2.10 and Theorem 2.7.  $\square$

**Remark 2.12 (The quadratic analog).** A completely analogous argument proves the corresponding statement for quadratic maps:

If a parameter ray of angle  $\theta$  lands at a parabolic point of the Mandelbrot set, then  $\theta$  is periodic under doubling. Furthermore, the dynamic ray of angle  $\theta$  for any map  $f$  belonging to this parameter ray contains the entire orbit of the critical point under  $f^{\circ q}$ , where  $q$  is the period of  $\theta$ .

Of course these results are well known. (Compare [DH1, Chapter 8, Section 2.2 and Chapter 13] and Schleicher [Sch, Theorem 1.1]). However this method of proof seems much easier.

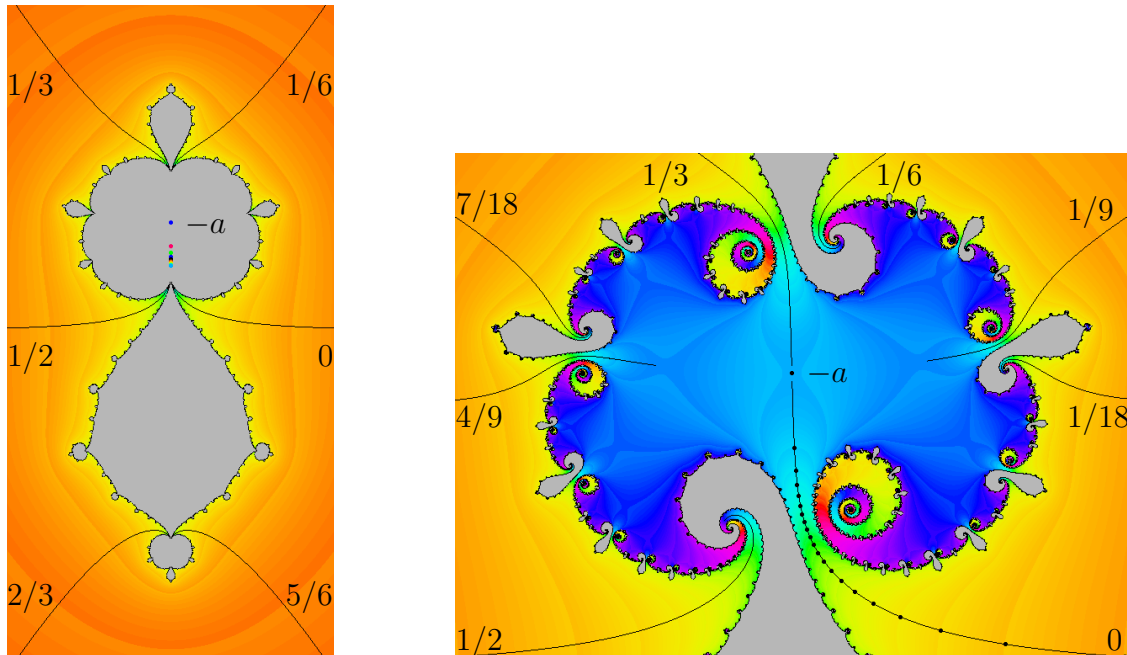


Figure 7: On the left: Julia set for the map  $z \mapsto z^3 + iz^2 + z$  in  $\mathcal{S}_1$ , showing the free critical orbit converging from above to the parabolic fixed point at  $z = 0$  within the basin  $U$ . On the right: detail of the Julia set for a map on the  $\theta = 2/3$  parameter ray, showing that the dynamic rays of angle  $\theta + 1/3 = 0$  and  $\theta - 1/3 = 1/3$  crash together at the free critical point (picture by Scott Sutherland).

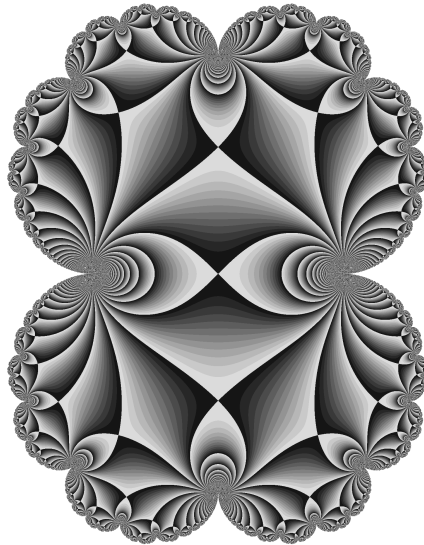


Figure 8: A picture of the standard cauliflower  $z \mapsto z^2 + z$  showing the real part  $\text{Re}(\Phi(z))$  of the Fatou coordinate, modulo  $\mathbb{Z}$ . Here the shading varies from white for zero+ modulo  $\mathbb{Z}$ , to black for one- modulo  $\mathbb{Z}$ . Thus the boundary curves between black and white indicate places where the real part of  $\Phi$  is an integer. The points where two such curves cross represent the critical point and its iterated pre-images.

**Remark 2.13 (Cyclic order).** If three or more parameter rays land at a common point (either parabolic or Misiurewicz), then we believe that the cyclic order of the rays about their landing point is always the same as the cyclic order of their parameter angles. (This is purely a local statement, and does not depend on whether the rays belong to the same escape region or to different escape regions.) For the Misiurewicz case compare Conjecture 6.1; while for the parabolic case compare the more detailed discussion in Section 4.

We next provide a more detailed description of the parabolic case, which will play an essential role in later sections. For the following, the symbol  $F$  will always denote a map which is parabolic, and hence belongs to the connectedness locus.

**Remark 2.14 (Dynamics in the parabolic basin).** Dynamics within a parabolic basin can be rather complicated, and is best understood in terms of Fatou coordinates. In the case of an  $F$ -invariant basin with a single simple critical point, the map is always topologically conjugate to the standard quadratic example which is illustrated in Figure 8. Here the interior of  $U$  is divided into simply connected open “cells”, bounded by curves which are black on one side and white on the other. Each such cell maps biholomorphically onto a different cell, and two cells have the same image if and only if they are diametrically opposite with respect to the central critical point. Each cell which has the parabolic fixed point as a boundary point maps to an immediate neighbor, either the right hand neighbor if it is along the  $x$ -axis, or the left hand neighbor otherwise.

**Remark 2.15 (Parabolic Multipliers).** One basic invariant of a parabolic map  $F$  in  $S_p$  is its *multiplier*  $\lambda$ .

**Definition.** If the parabolic orbit for  $F$  has period  $k$ , then  $\lambda$  is the first derivative of  $F^{\circ k}$  at any orbit point.

This is always a root of unity. More precisely, if the ray period is  $q$  then  $\lambda$  is a  $(q/k)$ -th root of unity. For further discussion see Conjecture MC2 in Remark 2.28.

**Theorem 2.16 (Parabolic Maps).** *Suppose that  $F$  has a parabolic orbit of ray period  $q$ . Let  $U(-a)$  be the Fatou component of  $F$  which contain the free critical point  $-a$ . Then, with notation as in Definition 2.4, the dynamic ray of angle  $\theta_q$  for  $F$  lands at the **root point** of  $U(-a)$ ; that is at the unique boundary point which is fixed by  $F^{\circ q}$ . (See Definition 2.11.) Similarly the non-periodic ray of angle  $\hat{\theta}$  lands at the unique boundary point of  $U(-a)$ , which is not equal to the root point, and yet maps to the root point under the 2-fold branched covering map  $F^{\circ q}$  from  $U(-a)$  to itself. Similarly, if we define the root point of the Fatou component  $U(2a)$  to be the unique point which maps to the root point of  $U(v')$  under  $F$ , then the non-periodic dynamic ray of angle  $\theta$  for  $F$  lands at the root point of  $U(2a)$ .*

**Proof.** The following diagram represents the various Fatou components which must be considered in the case  $q > 1$ .

$$U(2a) \xrightarrow{F} U(v') \begin{array}{c} \xrightarrow{F^{\circ q-1}} \\ \xleftarrow{F} \end{array} U(-a) \quad (6)$$

(Here we are only concerned with the orbit of the free critical point: the marked critical point is not involved in this discussion.) Thus the Fatou component  $U(2a)$  containing  $2a$  maps isomorphically onto the component  $U(v')$  under  $F$ , and then isomorphically onto the component  $U(-a)$  under  $F^{\circ q-1}$ . Then  $F$  sends it back to the component  $U(v')$  by a 2-fold branched covering map. For the special case  $q = 1$ , since  $U(v') = U(-a)$  there is a simpler diagram.

$$U(2a) \xrightarrow{F} U(-a) \curvearrowright_F$$

Since  $\theta$  has co-period  $q$ , we know that the angle  $\theta_1 = 3\theta$  is periodic of period  $q$ . It follows from Definition 2.11 that the dynamic ray of angle  $\theta_1$  lands at the root point of the Fatou component  $U(v')$  containing  $v' = F(-a)$ . It follows inductively that the dynamic ray of angle  $\theta_j$  lands at the root point of the component containing  $F^{\circ j}(-a)$ . Since the cycle of components has period  $q$  it follows that the ray of angle  $\theta_q$  lands at the root point of the component  $U(-a)$  itself.

The root point of  $U(v')$  has three pre-images under  $F$ . One is the root point of  $U(2a)$ , one is the root point of  $U(-a)$ , and the third is a diametrically opposite point of the boundary of  $U(-a)$ . Correspondingly the dynamic ray of angle  $\theta_1$  has three pre-images under  $F$ . The ray of angle  $\theta$  lands at the root point of  $U(2a)$ ; the ray of angle  $\theta_q$  lands at the root point of  $U(-a)$ ; while the ray of angle  $\hat{\theta}$  lands at the diametrically opposite point of the boundary of  $U(-a)$ .  $\square$

**Remark 2.17.** It might seem natural to expect that as a sequence of maps  $F_h$  on the parameter ray  $\mathfrak{R}$  converge to the landing map  $F_{\mathfrak{R}}$ , the corresponding dynamic rays of angle  $\theta \pm 1/3$  would converge to uniquely defined paths from infinity to  $-a$ ; but this may not be true. The limit outside of the filled Julia set  $K(F_{\mathfrak{R}})$  is uniquely defined. However, depending on the Lavaurs phase, there may be infinitely many possible limit maps inside of this filled Julia set, depending on which sequence of points of  $\mathfrak{R}$  we choose. (See [BMS].)

These results have an interesting consequence as follows.

**Corollary 2.18.** *Suppose that several co-periodic parameter rays with parameter angles  $\theta(j)$  land at a common parabolic map  $F \in \mathcal{S}_p$ . Then the dynamic rays of angle  $\theta(j)$  for  $F$  all land at the root point  $z_F$  of the co-critical component  $U(2a)$  in the filled Julia set. (Here these parameter rays need not all lie in the same escape region.)*

*Proof.* This follows immediately from Theorem 2.16.  $\square$

**Corollary 2.19.** *No two co-periodic parameter rays landing at a common point can have the same parameter angle. (This is true whether the rays lie in the same escape region or different escape regions.)*

*Proof.* This follows immediately from Corollary 2.18.  $\square$

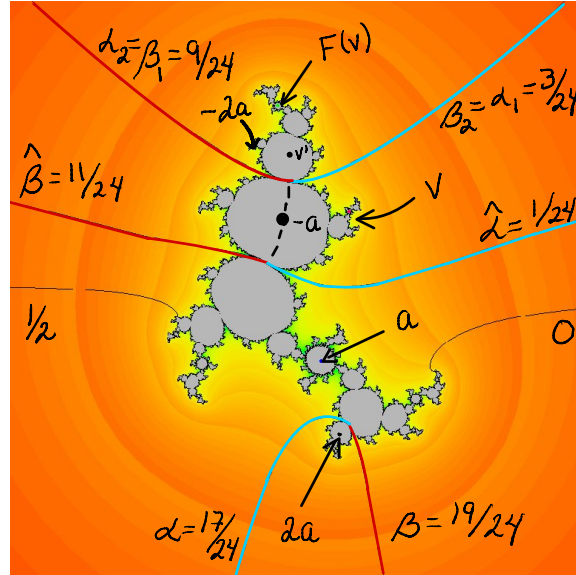


Figure 9: Julia set for a parabolic map in  $\mathcal{S}_3$  which is the landing point for two different parameter rays of co-period two with angles  $\alpha = 17/24$  and  $\beta = 19/24$ . In this example, there is a single parabolic fixed point, which is the root point of both the  $-a$  and the  $F(-a) = v'$  components. Furthermore, in this example the parameter angles  $\alpha$  and  $\beta$  belong to the same grand orbit, so that  $\alpha_1 = \beta_2$  and  $\beta_1 = \alpha_2$ . The corresponding point  $F$  in the parameter space  $\mathcal{S}_3$  is visible towards the upper left in Figure 33. There is an analogous picture for an arbitrary parabolic map in any  $\mathcal{S}_p$ , although the corresponding number of parameter rays will vary (conjecturally always between one and four). Compare Remark 2.23.

**Examples:** For each fixed co-periodic angle  $\theta$ , we will see in Section 5 that there are  $\mathbf{d}_p$  distinct parameter rays in  $\mathcal{S}_p$  with parameter angle  $\theta$ , where  $\mathbf{d}_p$  is the degree of  $\mathcal{S}_p$  (asymptotic to  $3^{p-1}$ ). Thus, for each such  $\theta$  there correspond  $\mathbf{d}_p$  distinct parabolic landing points. For examples in the case  $p = 2$  with  $\mathbf{d}_2 = 2$ , see Figures 15, and 17 or 18. For many examples with  $p = 3$  and  $\mathbf{d}_3 = 8$ , see Figures 31 through 35. In all of these cases, there is just one such ray in each escape region. However, for  $p \geq 4$  there are regions of multiplicity  $\mu > 1$ , each containing  $\mu$  such rays.

**A convenient notation.** We will often use the notation  $\mathbf{p}$  for a parabolic map, when we are thinking of it simply as a point in the parameter space  $\mathcal{S}_p$ . In such cases, we will use the notation  $F_{\mathbf{p}} : \mathbb{C} \rightarrow \mathbb{C}$  if we are thinking of it explicitly as a cubic map from the complex plane to itself.

As an example, in the lower right of Figure 17, the four parameter rays with angles  $\theta = 10/24, 11/24, 14/24$  and  $17/24$  belong to two different escape regions, but still lie in positive cyclic order around their common landing point  $\mathbf{p}$ . The dynamic rays with the same angles land at a common point  $z_0$  in the Julia set for  $F_{\mathbf{p}}$ . Here  $z_0$  is the root point of the hyperbolic component containing  $2a$ , as shown in Figure 21. The associated periodic angles  $3\theta = 1/4, 3/8, 3/4, 1/8$  are also in positive cyclic order, and land at the image  $F_{\mathbf{p}}(z_0)$ , which is the root point of the component containing  $-a$ . (Notice that in this particular case the Fatou components of  $-a$  and of  $v'$  share the same root point.)

In many cases the converse of Corollary 2.18 is true, so that a dynamic ray lands at the co-critical root point if and only if there is a parameter ray with the same angle landing at the given parabolic map. But there are also many counterexamples. For example Figure 22 shows four rays (in three different escape regions) landing at a parabolic map in  $\mathcal{S}_5$ ; and Figure 23 shows the four corresponding rays in the dynamic plane. But there are six additional rays in the dynamic plane, corresponding to six additional accesses to the root point. (Compare Remark 3.28.) Note that this parabolic map is on the common boundary between a rabbit region, and two different escape regions.

Conjecturally, such rabbit examples are the only counterexamples to the converse statement. And even in these counterexamples, for every dynamic ray landing at the co-critical root, there seems to be a parameter ray with the same angle which lands fairly close to the parabolic point. Furthermore, these other rays seem to play an important role in understanding the local dynamics (see [BM]).

Note also that the local angles between parameter rays at their landing point are quite different from the corresponding angles between dynamic rays (which are not even well defined unless the multiplier is real). This is completely analogous to what happens for the quadratic family. For example, since the parameter rays of angle  $1/7$  and  $2/7$  for the Mandelbrot set land at the “fat rabbit” map  $F_0$ , it follows that the  $1/7$  and  $2/7$  dynamic rays for  $F_0$  land at a common point in  $J(F_0)$ . But the  $4/7$  dynamic ray also lands at this same point. Similarly the correspondence does not preserve local angles in the quadratic case: The  $180^\circ$  angle between parameter rays at their landing point is not equal to the apparent  $120^\circ$  angles between dynamic rays at their landing point. (The latter angles are not actually well defined since the dynamic rays spiral in to their landing point.)

In §3 we will prove that every parabolic map in  $\mathcal{S}_p$  is the landing point of at least one co-periodic ray. (See Theorem 3.18 and Corollary 3.19.)

To conclude this section, we will describe several important concepts.

**Definition 2.20 (Kneading).** For every escape region  $\mathcal{E}_h \subset \mathcal{S}_p$  there is an associated infinite *kneading sequence*

$$(\kappa_1, \kappa_2, \kappa_3, \dots),$$

where  $\kappa_j = 0$  if  $F^{\circ j}(a)$  belongs to the lobe of the figure eight containing  $a$ , and where  $\kappa_j = 1$  if it belongs to the other lobe which contains  $-2a$ . (Compare Figure 1.) Here  $F$  can be any map in  $\mathcal{E}_h$ . Since the marked critical point  $a$  has period  $p$ , it follows that

$$\kappa_p = 0, \quad \text{and that} \quad \kappa_j = \kappa_{p+j} \quad \text{for all } j.$$

(Note that the minimal period of this sequence may be some divisor of  $p$ .)

In practice, it is usually more convenient to list only the first  $p$  entries  $(\kappa_1, \dots, \kappa_p)$  which we will call the *kneading invariant* of the escape region. (Here  $\kappa_p$  is always zero.) We will often abbreviate this notation, writing for example 110 in place of  $(1, 1, 0)$ . (Note that the various kneading invariants  $(1, 0)$  in  $\mathcal{S}_2$  or  $(1, 0, 1, 0)$  in  $\mathcal{S}_4$  or  $(1, 0, 1, 0, 1, 0)$  in  $\mathcal{S}_6$  all give rise to the same kneading sequence of period two; which can be denoted briefly by  $\overline{10}$ .)

**Remark 2.21 (The Mandelbrot Set and  $\mathcal{S}_p$ ).** The classical quadratic Mandelbrot set, which we denote by  $\mathbb{M}$ , plays two quite different roles in the study of  $\mathcal{S}_p$ .

- (1) Every  $\mathcal{S}_p$  contains infinitely many copies of  $\mathbb{M}$ , which play a very important role. These will be studied in Remark 2.28 below.
- (2) Branner and Hubbard [BH1] showed that every escape region  $\mathcal{E}$  in  $\mathcal{S}_p$  has a unique *associated critically periodic quadratic map* with the following property:

For every map  $F$  in  $\mathcal{E}$ , every connected component of the Julia set  $J(F)$  is either a point, or a copy of the Julia set for the associated quadratic map.

If the kneading sequence for an escape region in  $\mathcal{S}_p$  has minimal period  $k$ , then the period for the critical point of the associated quadratic map is  $p/k$ . (Compare Definition 2.6 as well as [M4, Theorem 5.15].) In particular, if the kneading invariant is  $(0, 0, \dots, 0)$  so that  $k = 1$ , then the quadratic map has critical period  $p$ .

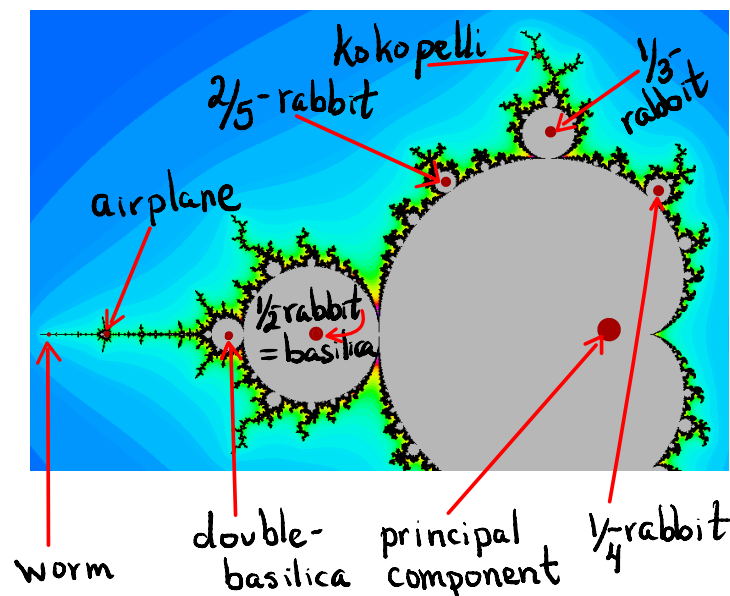


Figure 10: The classical Mandelbrot set  $\mathbb{M}$ , showing some of the critically periodic points that we will refer to. (Compare [BKM, Table 5.15]. Here the “worm” is the left-most period four component.) The immediate satellites of the main hyperbolic component are referred to as **rabbit** components. There is one rabbit component for each rational number  $0 < n/p < 1$ .

**Definition 2.22 (Zero-Kneading Regions).** We will say that an escape region in  $\mathcal{S}_p$  belongs to the *zero-kneading family* if its kneading invariant  $(0, 0, \dots, 0)$  consists of  $p$  zeros, or in other words if its kneading sequence is  $\bar{0}$ , of period one. In this case, Branner and Hubbard showed that the associated quadratic map determines the escape region uniquely. Zero-kneading regions are always invariant under 180 degree rotation ([BKM, Lemma 5.16]).

They are invariant under complex conjugation if and only if the associated quadratic map has real coefficients.

In particular, for each of the components emphasized in Figure 10, there is a corresponding escape region in some  $\mathcal{S}_p$ . The main hyperbolic component corresponds to the unique escape region in  $\mathcal{S}_1$ . There is the “basilica” region in  $\mathcal{S}_2$ . There are the “airplane” and two “rabbit” regions in  $\mathcal{S}_3$ . In  $\mathcal{S}_4$  there are the “Kokopelli” region (see Figure 44) and its complex conjugate, as well as the “ $(\pm 1/4)$ -rabbit” regions, the “double-basilica” region, and the “worm”. Compare [BKM, Ex. 5.14].

Every  $\mathcal{S}_p$  with  $p > 1$  contains two or more rabbit regions, corresponding to the period  $p$  immediate satellites of the Mandelbrot set. For more about zero-kneading regions see [BM] (the sequel to this paper).

For  $p \leq 4$  the following statement is true:

Two escape regions with a common boundary point always have different kneading sequences. In particular, no two zero kneading regions can share a boundary point.

It seems likely that this statement is true in every  $\mathcal{S}_p$ . As a step in this direction: [AK, Theorem 6.8] shows that if the common boundary point is also a boundary point of a hyperbolic component of Type B  $(m, n)$  then the  $m$ th component of the kneading sequence always flips as we cross from one escape region to the other, but no other component changes. (For the definition of Type B  $(m, n)$  see Remark 2.26.) In [AK], Arfeux-Kiwi provide a similar but much more complicated rule in the case of a Type A component.

**Non-Zero Kneading.** In all cases with non-zero kneading, since the kneading period  $k$  is greater than one, the period for the associated map is some proper divisor  $p/k < p$ . In particular, in many cases we will have  $p/k = 1$ , which means that all Julia sets in the escape region will contain countably many connected components which are topological circles. In particular, if  $p$  is a prime number then this will certainly happen in all cases with non-zero kneading.

**Remark 2.23 (From Julia Set to Kneading Invariant).** Any parameter ray  $\mathfrak{R}$  of co-period  $q$  lands at some parabolic map  $\mathfrak{p}$ . Given the parameter angle  $\theta$ , and the Julia set  $J(F_{\mathfrak{p}})$ , we will show that it is not difficult to compute the kneading invariant for the escape region which contains  $\mathfrak{R}$ . (Compare [AK, Definition 5.3]; which also includes an analogous discussion for parameter rays which are rational but not co-periodic.)

Recall from Theorem 2.16 that the dynamic ray of angle  $\theta$  must land at the root point of the Fatou component which contains  $2a$ . Hence for  $1 \leq j \leq q$  the ray of angle  $\theta_j = 3^j\theta$  lands at the root point of the component which contains  $F_{\mathfrak{p}}^{\circ j}(2a) = F_{\mathfrak{p}}^{\circ j}(-a)$ . In particular, the ray of angle  $\theta_q$  lands at the root point of the component  $U = U(-a)$  which contains the free critical point  $-a$ . Note that the map  $F_{\mathfrak{p}}$  from  $U$  to  $F_{\mathfrak{p}}(U)$  is a 2-fold branched covering map (with reference to Equation (6)).

The parameter angle  $\theta$  of co-period  $q$  gives rise to a *triad*

$$(\theta, \theta_q, \widehat{\theta})$$

consisting of three equally spaced dynamic angles, where  $\theta$  and  $\hat{\theta}$  are co-periodic, but  $\theta_q$  is periodic of period  $q$ . In the dynamic plane for the parabolic landing point, the  $\theta$  ray lands at the root point of  $U(2a)$ , the  $\theta_q$  ray lands at the root point of  $U(-a)$ , and the  $\hat{\theta}$  ray lands at the “opposite” boundary point of  $U(-a)$ , which maps to the root point under the 2-fold covering map  $F_p^{\circ q}$ . (Compare Figure 9.)

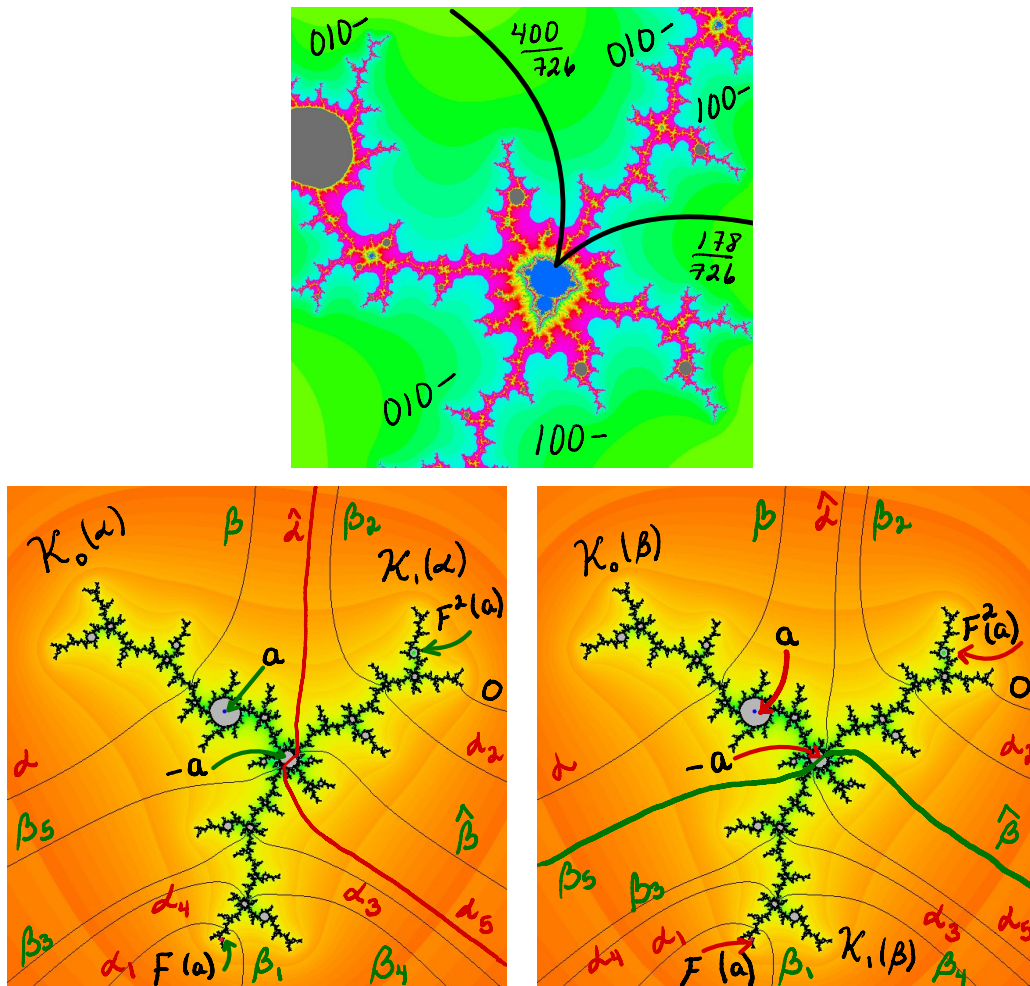


Figure 11: Above: A small Mandelbrot copy in  $\mathcal{S}_3$  lying along the boundary between the 010– and 100– regions. Below: The dynamic plane for the parabolic landing point, with the  $\alpha$ -wall on the left and the  $\beta$ -wall on the right, where  $\alpha$  has numerator 400 and  $\beta$  has numerator 178. The corresponding kneading invariants, 010 on the left and 100 on the right, can be computed using Lemma 2.25.

**Definition 2.24 (Walls and Kneading Walls).** By a *wall* across  $\mathbb{C}$  we will mean a closed subset homeomorphic to  $\mathbb{R}$ . Any wall separates  $\mathbb{C}$  into two complimentary simply-connected open sets.

Let  $\mathfrak{p}$  be a parabolic point of ray period  $q$  in  $\mathcal{S}_p$ , and let  $\theta$  be the angle of some parameter ray which lands on  $\mathfrak{p}$ . Then in the dynamic plane for the map  $F = F_p$ , the

dynamic ray of angle  $\theta$  will land at the root point of the  $U(2a_p)$  component. The union of the  $\theta_q$  and  $\widehat{\theta}$  dynamic rays, together with an arc within  $U(-a_p)$  joining their landing points, will be called the  $\theta$ -**kneading wall** across the dynamic plane. This wall bisects the plane, dividing it into an open set  $\mathcal{K}_0(\theta)$  containing the marked critical point  $a_p$ , and an open set  $\mathcal{K}_1(\theta)$  containing the marked co-critical point  $-2a_p$ . Every point of the marked periodic orbit must belong to one of these two open sets.

See Figures 9, 21, 23, for examples where the root point of  $U(-a_p)$  is a fixed point of  $F$ ; and see Figures 11 and 61-right for examples where it is not a fixed point.

**Lemma 2.25.** *The kneading invariant  $(\kappa_1, \dots, \kappa_q)$  for the escape region which contains this parameter ray of angle  $\theta$  can be computed as follows. We have  $\kappa_j = 0$  if and only if  $F_p^{\circ j}(a) \in \mathcal{K}_0$ , and  $\kappa_j = 1$  if and only if  $F_p^{\circ j}(a) \in \mathcal{K}_1$ .*

*Proof.* (Compare [AK, Definition 5.3].) The proof is easily supplied: As we approximate  $F_p$  closely by a map  $F$  which lies on the parameter ray  $\mathfrak{R}$ , the dynamic rays of angle  $\theta_q$  and  $\widehat{\theta}$  will deform continuously outside of the open set  $U$ , but will crash together inside  $U$ . Since the marked periodic orbit will also deform continuously, the conclusion follows.  $\square$

As an example, applying this lemma to Figure 9, it follows that the  $\alpha = 17/24$  parameter ray in an escape region of  $\mathcal{S}_3$  with kneading invariant 110, shares a landing point with the  $\beta = 19/24$  parameter ray in a region with invariant 010. See Figure 33, upper left, for the corresponding point in parameter space.

**Remark 2.26 (Hyperbolic Components).** The most basic distinction in our pictures of  $\mathcal{S}_p$  is between the **connectedness locus**, consisting of maps with connected Julia set, and the various escape regions. The connectedness locus contains four essentially different types of hyperbolic components. (Compare [M4, §1A].) If  $F$  is any map belonging to the hyperbolic component  $H$ , then  $H$  belongs to one of four types, as follows.

**Type A** if both critical points of  $F$  belong to the same Fatou component.

**Type B** if the critical points belong to different components of a common cycle of Fatou components. More explicitly, it has **Type B**( $m, n$ ) if

$$a \xrightarrow{F_0^{\circ m}} -a \xrightarrow{F_0^{\circ n}} a$$

where  $F_0$  is the center point of the hyperbolic component, and where  $m + n = p$  with  $m, n > 0$ .

**Type C** if some forward image  $F^{\circ n}(-a)$  belongs to the cycle of attracting Fatou components containing  $a$ , but the free critical point  $-a$  itself does not.

**Type D** if the critical points belong to disjoint cycles of attracting Fatou components. More explicitly we will call this **Type D**( $q$ ) if the free critical point  $-a$  belongs to a component of period  $q$ .

In our figures, the components of Type A, B and C are brown, while those of Type D are blue. The escape regions have lighter colors, tending towards green (or red) near the border. In all cases, the background is computer drawn, but any parameter rays are hand drawn approximations.

There are only finitely many components of Type A and B in each  $\mathcal{S}_p$ , while there are infinitely many of Type C and D. The components of Type A, B, and especially D, play an important role in the organization of each  $\mathcal{S}_p$ . (See for example Section 4.) Components of Type C usually appear as small attachments to the much larger A or B components, or as isolated disks. For examples see Figure 11 (top-left), or Figure 65 (left).

**Remark 2.27 (Root Points in Parameter Space).** By definition a *root point* of a hyperbolic component in  $\mathcal{S}_p$  is a parabolic boundary point with minimal ray period. Here components of Type D have one root point; those of Type A have two root points; and those of Type B have three root points. As one example, the archetypal Type A component is the central lemon shaped component in  $\mathcal{S}_1$ , with root points at the upper and lower tips. (Compare Figure 19.) As far as we know, those of Type C can never have a parabolic boundary point.

Assuming Conjecture MC1 below, it follows that components of Type A and B always have attached components of Type D. We believe that components of Type C never have such attachments. (For details in the Type A and B cases see [M1] and [AK, Theorem 6.6]. Similar arguments prove the corresponding statement for components of Type D.)

**Remark 2.28 (Copies of  $\mathbb{M}$  in  $\mathcal{S}_p$ : Three Basic Conjectures).** McMullen [Mc]<sup>1</sup> has shown that families of rational maps often contain many hybrid-conjugate copies of the quadratic Mandelbrot set  $\mathbb{M}$ . (Here “hybrid-conjugate” means that the copies are conformally isomorphic to  $\mathbb{M}$  throughout the interior; but only quasi-conformally isomorphic on the boundary.) In our case, we conjecture a somewhat more explicit statement.

**Conjecture MC1.** Every parabolic point in  $\mathcal{S}_p$  is contained in a unique maximal hybrid-conjugate copy of  $\mathbb{M}$ . Similarly every hyperbolic component of Type D in  $\mathcal{S}_p$  is contained in a unique maximal hybrid-conjugate copy of  $\mathbb{M}$ .

It follows for example that every parabolic point is the root point of a unique component of type D, and that parabolic points are everywhere dense on the boundary of each such component.

Now consider the *multiplier* of a parabolic point, as defined in Remark 2.15.

**Conjecture MC2.** Let  $F_p$  be a parabolic map in a copy  $M$  of  $\mathbb{M}$ . Then the multiplier of  $F_p$  is equal to the multiplier of the corresponding parabolic map in  $\mathbb{M}$ .

As an example, this implies that the multiplier of  $F_p$  is equal to  $+1$  if and only if  $p$  is the cusp point of its copy of  $\mathbb{M}$ .

---

<sup>1</sup>Special cases of [Mc, Theorem 1.1] were studied by Douady and Hubbard in [DH3, pgs. 332-336] and by Eckmann and Epstein in [EE].

By the *period* of a critically periodic map in  $\mathcal{S}_p$  we will mean the period of its free critical point. By the *period* of a Mandelbrot copy  $M$  we will mean the period of the center of its main hyperbolic component.

**Conjecture MC3.** If  $F$  is the critically periodic center point of a component in  $M$ , then the period of  $F$  is the product of the period of  $M$ , and the period of the corresponding critically periodic point in  $\mathbb{M}$ . (In particular if  $M$  has period  $q$ , then the period of the center point of any component of  $M$  will be some multiple of  $q$ .)

**Remark 2.29 (A Question).** If  $F$  is the center point of a hyperbolic component contained in such a copy  $M \subset \mathcal{S}_p$ , how is the Hubbard tree of  $F$  related to the Hubbard tree of the associated critically periodic quadratic map?

Giving a sufficiently precise answer to this question, it might be possible to give a constructive proof of Conjecture MC1. But before discussing the question, we need a precise definition which is weak enough so that it makes sense to compare quadratic and cubic Hubbard trees. (See Appendix B.)

**Remark 2.30 (Dual Critically Periodic Points in Parameter Space).** Suppose that both critical points of a cubic polynomial are periodic. We have a choice as to which one to mark if the map represents the center point of a hyperbolic component of Type B or D. (For center points of A components, the two critical points coincide, so there is no choice.) If one choice of marked point give rise to a point  $F \in \mathcal{S}_p$ , then the other choice gives rise to a *dual* point  $F^* \in \mathcal{S}_q$ , where  $q$  is the period of the other critical point. Note that  $F$  and  $F^*$  are identical as maps from  $\mathbb{C}$  to  $\mathbb{C}$ . In particular, the Julia set  $J(F)$  is identical to the Julia set  $J(F^*)$ . The only difference is the choice of which critical point to mark. In the case of an A component, we say that the center point is *self-dual*.

If  $(a, v)$  are the coordinates of a critically periodic point in  $\mathcal{S}_p$ , then the dual center point in  $\mathcal{S}_q$  has coordinates

$$(a', v') = (-a, F(-a)) = (-a, 4a^3 + v).$$

Here  $p = q$  in the case of a map of Type A, B or D ( $p$ ). However for a component of type D( $q$ ) in  $\mathcal{S}_p$  with  $p \neq q$ , the dual point will be of Type D( $p$ ) in the space  $\mathcal{S}_q$ .

For centers of Type B( $r, s$ ) (where  $r, s > 0$  and  $r + s = p$ ), the dual is of Type B( $s, r$ ). In the special case  $r = s = p/2$ , the component is *weakly self-dual* in the sense that the 180 degree rotation of the Julia set interchanges the two critical points  $a$  and  $-a$ . (Compare Figure 14. The involution  $(a, v) \leftrightarrow (a', v')$  has an actual fixed point only for the center of an A component.)

The center of a D component can never be self-dual. For this would imply that it has two different root points, which is impossible. (Compare Remark 2.27.)

The self-duality of an A component may seem uninteresting, but in fact it has significant consequences. According to Conjecture MC1, each of the two root points is also the root point of a component of type D. As we pass from one root point to the opposite one along

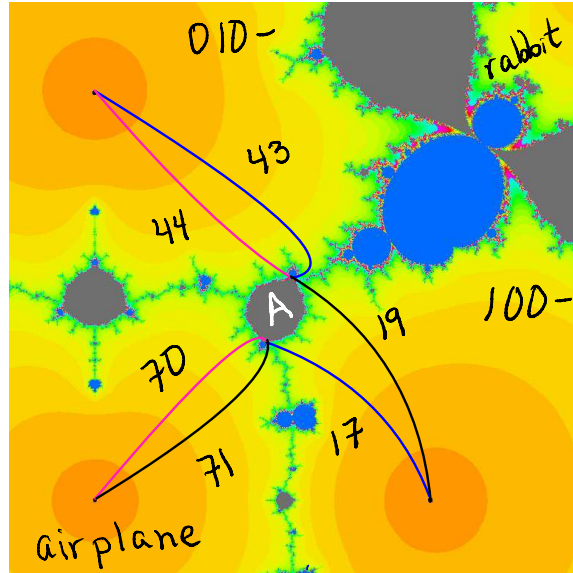


Figure 12: Detail of  $\mathcal{S}_3$ . (Compare Figures 30 through 37.) Four different escape regions are visible. Here the large Mandelbrot copy crashes into a Type A component at the root point of its airplane component, so that the tip of the copy gets bent upward. It is interesting to note that the small D component at the bottom of the A component is the dual of the “airplane” component at the top, so that the Julia sets of the center points are the same, but the roles of  $+a$  and  $-a$  are interchanged. Here twin rays have been given the same color. (Compare Remark 2.30.) All angles have denominator  $78 = 3d(3)$ . (See Remark 2.5.)

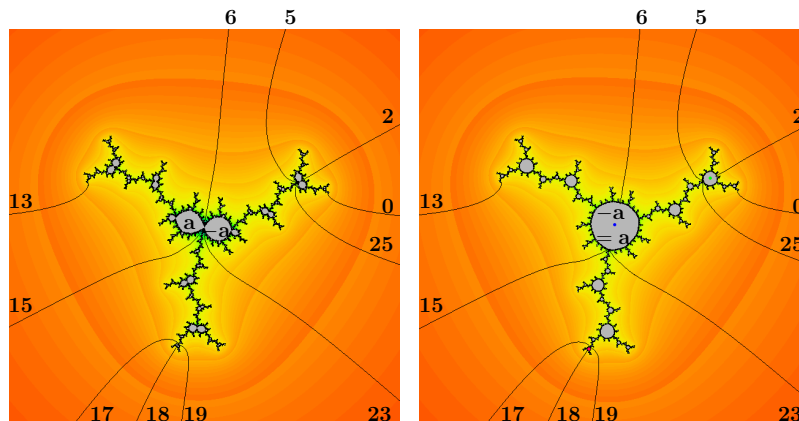


Figure 13: On the left, Julia set for the center of the Type D component which is attached to the top of the Type A component in the lower left of Figure 12. The lower Type D component has the same Julia set but with  $+a$  and  $-a$  interchanged. On the right, the Julia set for the center of this type A component, with  $+a = -a$ . All angles have denominator  $d(3) = 26$ . Note that the upper root point is the landing point of the  $(43, 44, 19)/78$  parameter rays, while the lower root point is the landing point for the  $(17, 70, 71)/78$  rays. Both of these triples correspond to the angles  $(17, 18, 19)/26$  for the critical value root point of the Julia set on the left, where  $(17, 18, 19) \mapsto (25, 2, 5) \mapsto (23, 6, 15)$ .

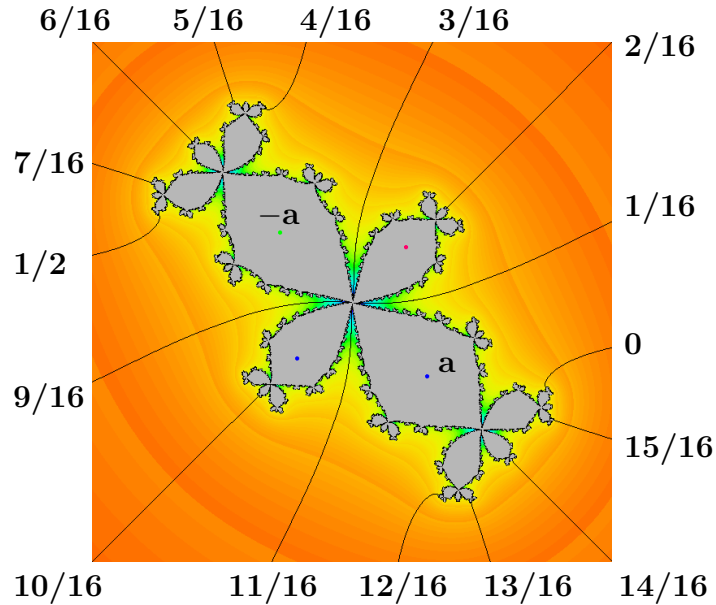


Figure 14: A weakly self-dual Julia set of Type B  $(2, 2)$  in  $\mathcal{S}_4$ . Here the two largest components are centered at  $+a$  and  $-a$ . The 180 degree rotation of this set interchanges the orbits of  $+a$  and  $-a$ . Note that  $1/16 \mapsto 3/16 \mapsto 9/16 \mapsto 11/16 \mapsto 1/16$ .

a path through the center, the critical points  $+a$  and  $-a$  cross through each other and are interchanged. As a consequence the D components at one root point are dual to the D components at the other one. (See for example Figures 12 and 13.)

For other examples of this duality see Remark 3.15, as well as the many examples in [BM].

Recall from Definition 2.4 that every co-periodic angle  $\theta$  has a unique *twin* co-periodic angle of the form  $\theta \pm 1/3$ . If two components  $H$  and  $H^*$  are dual to each, then the angles of parameter rays which land on a root point of  $H$  are twins of the angles of rays which land on a root point of  $H^*$ . In particular, if  $H$  is self-dual, then there are parameter rays with twin angles landing on the two root points of  $H$ .

This provides an easy way to distinguish between components of Type A and Type B in any parameter picture in which ray angles are provided: Choose any ray landing at a root point. There is a twin ray landing on the opposite root point of the same component if and only if it has Type A.

### 3 Tessellations and Orbit Portraits.

For each integer  $q \geq 1$  we will describe a partition of the smoothly compactified parameter curves  $\overline{\mathcal{S}}_p$  which controls the behavior of dynamic rays of period  $q$  for the associated Julia sets. (Compare Definition 3.7 and Theorem 3.18.)

**Definition 3.1.** Let  $q$  be any positive integer. The *period  $q$  tessellation* of the Riemann surface  $\overline{\mathcal{S}}_p$  is constructed as follows. The collection of all parameter rays of co-period  $q$  in all escape regions, together with their landing points, decomposes  $\mathcal{S}_p$  into a finite

number of connected open sets  $\mathcal{F}_k$ , which we will call the **faces** of the tessellation. (Note that there are only finitely many escape regions in  $\mathcal{S}_p$ , and only finitely many parameter rays of co-period  $q$  in each escape region. (Compare [M4, Corollary 5.12]; and see Section 5 for some specific numbers.) By definition, the **edges** of the tessellation consist of all parameter rays of co-period  $q$ ; while the **vertices** consist of:

- (1) **parabolic vertices**: the landing points of these rays; and
- (2) **ideal vertices** (or puncture points): the points of  $\overline{\mathcal{S}}_p \setminus \mathcal{S}_p$ .

Note that every edge joins a parabolic vertex to an ideal vertex. We will use the notation

$$\mathbf{Tes}_q(\overline{\mathcal{S}}_p) = (\mathbf{Tes}^{(0)}, \mathbf{Tes}^{(1)}, \mathbf{Tes}^{(2)})$$

for this tessellation, where  $\mathbf{Tes}^{(0)}$  is the set of vertices,  $\mathbf{Tes}^{(1)}$  is the set of edges, and  $\mathbf{Tes}^{(2)}$  is the set of faces.

**Remark 3.2.** Here we are stretching the usual concept of tessellation, which assumes that all faces are simply-connected. Our tessellations may well have faces which are not simply-connected. (Compare Figure 15.) In fact we see in [BM] that the tessellation  $\mathbf{Tes}_q(\overline{\mathcal{S}}_p)$  has non-simply-connected faces, and also has non-connected one-skeleton, whenever  $1 < p \neq q$ . On the other hand, it seems quite possible that, in all cases with  $p = q$ , the one-skeleton is connected, and every face is simply-connected. However we have no idea how to prove such a statement.

These tessellations are extremely complicated for all but the smallest  $p$  and  $q$ . (Compare Table 4 in Section 5.)

**Remark 3.3.** Each parameter ray in an escape region  $\mathcal{E}_j$  is a leaf in the smooth foliation of  $\mathcal{E}_j$  by its parameter rays. Since parameter rays can never intersect each other, we could equally well construct such a tessellation using any finite collection of co-periods  $q$ . Such **mixed period tessellations** provide more information by correlating behavior for several different periods. However we discuss only the simpler single period tessellations, which together provide all of the essential information, since a mixed period tessellation is completely determined by the corresponding single period tessellations.

Note that rays from two different escape regions  $\mathcal{E}_i$  and  $\mathcal{E}_j$  may well land at a common boundary<sup>2</sup> point in  $\partial\mathcal{E}_i \cap \partial\mathcal{E}_j$ . Similarly, a face  $\mathcal{F}_k \in \mathbf{Tes}_q^{(2)}(\overline{\mathcal{S}}_p)$  may well intersect several different escape regions, and will always intersect the connectedness locus. (Compare Figure 17. )

---

<sup>2</sup>Such a common boundary  $\partial\mathcal{E}_i \cap \partial\mathcal{E}_j$  (if non-empty) is always a compact subset of the connectedness locus. We suspect that this set is always totally disconnected. (See Figure 33 or 37 for examples.)

**Remark 3.4 (Parametrization of  $\mathcal{S}_p$ ).** To illustrate these tessellations, we must choose some parametrization of  $\mathcal{S}_p$ , of large open subsets of  $\mathcal{S}_p$ . For  $p \neq 3$  will use the local “*canonical coordinate*”  $\mathbf{t}$  around any point of the curve  $\mathcal{S}_p$ . (See [BKM, Section 2] or [BM, Appendix D].) On the other hand, in the special case of  $\mathcal{S}_3$ , it is more useful to use a *torus coordinate*, that is a suitably chosen affine coordinate on the universal covering surface of  $\overline{\mathcal{S}}_3$ , which is conformally isomorphic to  $\mathbb{C}$ . (See [BM, Appendix C].) In both cases, this parametrization is conformal, so that it preserves the shapes of small regions in  $\mathcal{S}_p$ .

**Example 3.5.** The space  $\mathcal{S}_1$  is isomorphic to  $\mathbb{C}$ , parametrized by the canonical coordinate  $\mathbf{t} = a$ , where  $a$  is the marked critical point. The space  $\mathcal{S}_2$  is isomorphic to  $\mathbb{C} \setminus \{0\}$ , parametrized by

$$\mathbf{t} = \frac{1}{3(v-a)},$$

where  $v$  is the marked critical value, with  $a \leftrightarrow v$ . See Figures 15 and 17, where the inner escape region  $\mathcal{E}_{\text{in}}$  parametrizes maps with kneading invariant  $(1, 0)$ , so that  $a$  and  $F(a) = v$  lie in different lobes of the figure eight curve of Figure 1. Every nontrivial component of the filled Julia set is a topological copy of the closed unit disk (Compare Definition 2.20.) The outer escape region  $\mathcal{E}_{\text{out}}$  parametrizes maps with kneading invariant  $(0, 0)$ , so that the orbit of  $a$  lies entirely in one lobe of the figure eight. In this case every nontrivial component of the filled Julia set is a copy of the basilica.<sup>3</sup>

For  $p > 2$  the canonical coordinate can only be defined as a local coordinate, since it ramifies at most ideal points. (See [BM, Appendix C] for further discussion.)

**Remark 3.6 (Symmetries).** Let  $\mathcal{G}$  be the commutative group consisting of the four transformations

$$z \longrightarrow \pm z \quad \text{and} \quad z \longrightarrow \pm \bar{z}$$

of the plane of complex numbers. Thus  $\mathcal{G}$  consists of three involutions, which we can describe as:

- *up-down reflection*  $z \longleftrightarrow \bar{z}$ ,
- *left-right reflection*  $z \longleftrightarrow -\bar{z}$ , and
- *180 degree rotation*  $z \longleftrightarrow -z$ ;

together with their product which is the identity transformation. Note that two of these four transformations are holomorphic and two are antiholomorphic.

This group  $\mathcal{G}$  acts naturally on each  $\mathcal{S}_p$ . If we think of  $\mathcal{S}_p$  as an affine variety with coordinates  $(a, v)$ , then the action of a group element  $g$  is given by  $g(a, v) = (g(a), g(v))$ .

---

<sup>3</sup>Compare Remark 2.21, as well as [BKM, Table 6.8 and Figure 9].

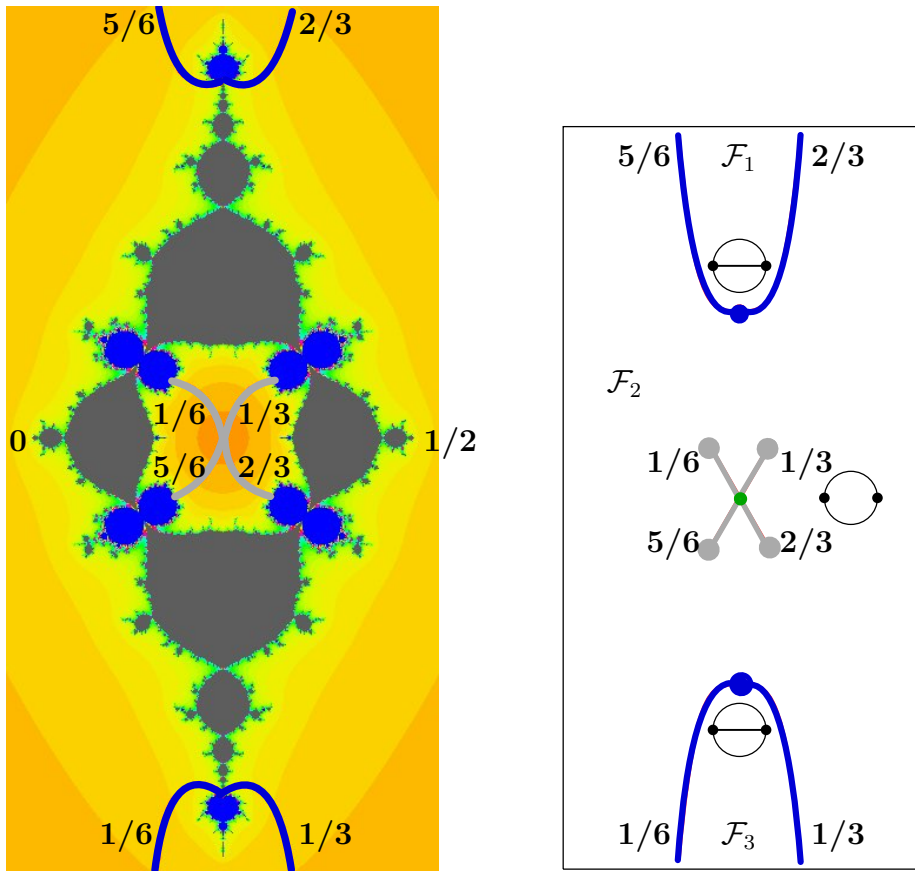


Figure 15: On the left, the curve  $\mathcal{S}_2$ , using the canonical coordinate  $t$ . The inner escape region with kneading invariant  $(1, 0)$  forms a neighborhood of the ideal vertex at the center of the figure, while the outer “basilica” escape region with kneading invariant  $(0, 0)$  is a neighborhood of the ideal vertex at infinity. Both regions have multiplicity  $\mu = 1$ . The four outer rays of co-period one divide the plane into three regions; but the four inner rays do not further separate the plane. (These rays are colored blue and gray respectively. Compare Definition 3.24.) On the right, a cartoon showing the resulting tessellation  $\text{Tes}_1(\overline{\mathcal{S}_2})$ . The orbit portrait associated with each face is indicated by a circle, with the points of angle zero and  $1/2$  joined whenever the corresponding rays have a common landing point. The six large dots represent parabolic vertices, while the green dot in the center represents one of the two ideal points. (The other ideal point is at infinity.) Note that the middle face intersects both of the escape regions.

On the other hand if we think of the elements of  $\mathcal{S}_p$  as polynomial maps  $F : \mathbb{C} \rightarrow \mathbb{C}$ , then it is given<sup>4</sup> by  $F \mapsto g \circ F \circ g$ .

For the associated Julia sets the appropriate formula is

$$J(g \circ F \circ g) = g(J(F)) .$$

(Compare Figure 16.) For either the angles of dynamic rays in a Julia set or the co-critical

<sup>4</sup>If  $F(z) = z^3 + \alpha z + \beta$ , then conjugating by  $z \mapsto \bar{z}$  sends  $F$  to  $z \mapsto z^3 + \bar{\alpha}z + \bar{\beta}$ ; while conjugation by  $z \mapsto -z$  sends it to  $z \mapsto z^3 + \alpha z - \beta$ .

angles of a parameter ray in  $\mathcal{S}_p$ , the corresponding action is given by

$$\begin{aligned} \theta &\mapsto -\theta && \text{for up-down reflection,} \\ \theta &\mapsto 1/2 - \theta && \text{for left-right reflection, and} \\ \theta &\mapsto 1/2 + \theta && \text{for 180 degree rotation;} \end{aligned}$$

where  $\theta \in \mathbb{R}/\mathbb{Z}$ .

**Note.** All of the escape regions we are familiar with have at least one non-trivial symmetry, so that there is at most one other region in  $\overline{\mathcal{S}}_p$  which is a holomorphic or antiholomorphic copy. However it seems quite possible that for higher values of  $p$  there exist escape regions with no symmetries other than the identity map, so that there could be four distinct regions which are copies of each other.

The parameter  $\mathbf{t}$  for  $\mathcal{S}_1$  or  $\mathcal{S}_2$ , or for the universal covering space of  $\overline{\mathcal{S}}_3$  will always be chosen so that the action of  $\mathcal{G}$  on this space corresponds to its action on the complex number  $\mathbf{t}$ . For  $p > 3$ , a similar statement is true for the local parametrizations. These automorphisms always preserve the tessellations.

**Definition 3.7 (Orbit Portraits).** Let  $F \in \mathcal{S}_p$  be a map such that every dynamic ray of period  $q$  lands at a (necessarily periodic) point of the Julia set. By definition the **period  $q$  orbit portrait**  $\mathcal{O}_q(F)$  is the following equivalence relation between angles of period  $q$  under tripling:

Two such angles  $\phi$  and  $\psi$  are equivalent, written  $\phi \simeq \psi$ , if and only if the corresponding dynamic rays have a common landing point in  $J(F)$ .

(Compare [M2].) This definition makes sense for every  $F$  in the connectedness locus  $\mathcal{C}(\mathcal{S}_p)$ . It also makes sense and is independent of  $F$  throughout each face  $\mathcal{F}_k$  of the tessellation  $\mathbf{Tes}_q(\overline{\mathcal{S}}_p)$ . However, in the special case where  $F$  belongs to a parameter ray of co-period  $q$ , the orbit portrait is not defined, since at least one period  $q$  dynamic ray must crash into a pre-periodic point and hence not land anywhere. In most cases, the orbit portrait will jump discontinuously as we cross such a ray. (Compare Corollaries 3.22 and Theorem 3.23.)

More generally we can consider **mixed period orbit portraits**. Let  $0 < q_1 < \dots < q_k$  be a finite list of periods. For a generic  $F \in \mathcal{S}_p$  we can consider the associated orbit portrait  $\mathcal{O}_{q_1, \dots, q_k}(F)$  in which we allow dynamic rays for all periods which are in the list. (Of course, dynamic rays of different period can never have a common landing point; hence their angles can never be equivalent.)

Such an equivalence relation between angles can be conveniently described by providing an unordered list of all of the equivalence classes which contain more than one element. As in Remark 2.5 we will write angles which have period  $q$  under multiplication by 3 as fractions of the form  $n/d$  with common denominator  $d = 3^q - 1$ . As an example, if  $q = 2$  so that  $d(2) = 8$  then the angles with period precisely  $q$  can be listed as  $1/8, 2/8, 3/8, 5/8, 6/8, 7/8$ . If the  $1/8$  and  $2/8$  rays land at one point and the  $3/8$  and  $6/8$  rays land at a different point, then we will write

$$\mathcal{O}_2(F) = \{1/8 \simeq 2/8, 3/8 \simeq 6/8\}.$$

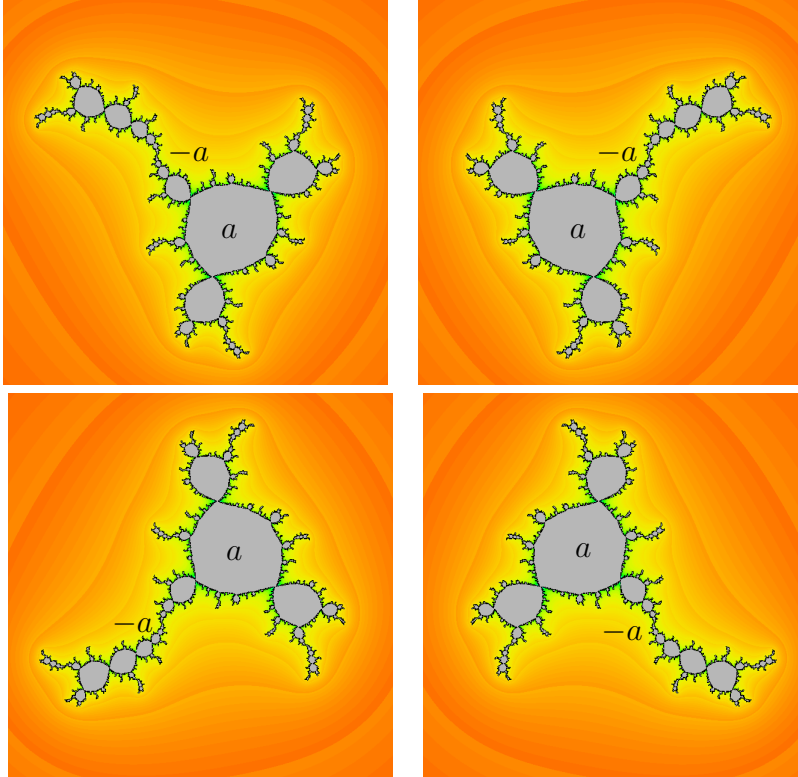


Figure 16: For most maps  $F \in \mathcal{S}_p$ , the four images  $g \circ F \circ g$  under conjugation by elements of  $\mathcal{G}$  are distinct, and the four corresponding Julia sets  $g(J(F))$  are also distinct. This figure shows a typical example, consisting of Julia sets for four Misiurewicz maps in  $\mathcal{S}_2$  which are on the boundary of the basilica escape region. (See Figure 5 in Section 2 for more detail of the lower left figure, and see Figure 15 or 17 for the full parameter space.) The group  $\mathcal{G}$  permutes these four maps, and correspondingly permutes their Julia sets. Thus this entire figure is invariant under the action of  $\mathcal{G}$ .

In practice we will often abbreviate the right hand side by writing  $\{1 \simeq 2, 3 \simeq 6\}/8$ . If all four of these rays land at a single point, we will write  $\{1 \simeq 2 \simeq 3 \simeq 6\}/8$ .

Such an orbit portrait can be described graphically by identifying each fraction  $n/d$  which has period  $q$  under tripling with the point  $e^{2\pi i n/d}$  on the unit circle, and then joining two such points by a path within the unit disk whenever the corresponding dynamic rays land at a common point in the Julia set. This can always be done so that two such paths intersect only when all of the associated dynamic rays land at a common point. As examples, the two orbit portraits described in the preceding paragraph corresponds to the two circle diagrams to the “south-east” in Figure 18.

Another way of expressing this condition is the following. By definition, two or more disjoint compact subsets  $A_j$  of the unit circle are *unlinked* if we can choose disjoint, compact connected sets  $A'_j$  in the unit disk so that  $A_j \subset A'_j$ . In fact, if the  $A_j$  are unlinked, then we can always choose  $A'_j$  to be the smallest convex set which contains  $A_j$ .

**Lemma 3.8.** *A necessary property of any orbit portrait (whether single period or mixed*

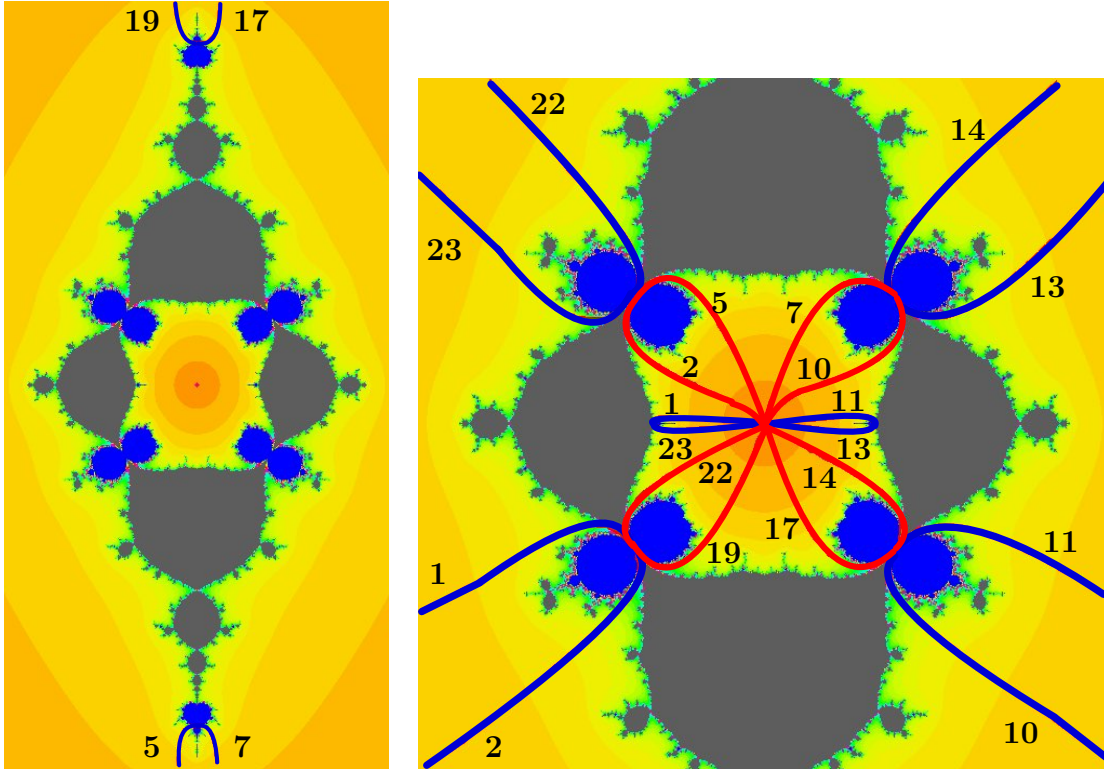


Figure 17: Showing the 24 parameter rays of co-period 2 for  $\mathcal{S}_2$  (twelve inside and twelve outside). Four of these rays are shown on the left, and the remaining twenty on the right. These rays divide the plane into sixteen period 2 faces. Compare Figure 18. For the distinction between red and blue rays, see Definition 3.24. All angles with denominator  $3d(2) = 24$ .

*period*) is that its various equivalence classes must be unlinked.

The proof is straightforward.  $\square$

Such a diagram in the unit disk can be thought of as the period  $q$  part of the Thurston lamination for  $F$ . See Figures 15 and 18 which show the orbit portraits associated with the various faces of the period one and two tessellations for the curve  $\mathcal{S}_2$ ; and Figure 19 for the various faces of the corresponding tessellations for the curve  $\mathcal{S}_1$ .

**Note.** Although we have described an orbit portrait as a geometric object, it can also be thought of as a finite dynamical system, consisting of the tripling map from a suitable set of angles of fixed co-period  $q$  to itself. Note that two orbit portraits which look very similar topologically, may have quite different dynamics. As an example, the orbit portrait  $\{1 \simeq 2 \simeq 3 \simeq 6\}/8$  looks topologically very much like  $\{1 \simeq 3 \simeq 9 \simeq 27\}/80$ . But the first consists of two orbits of period two while the second represents a single orbit of period four.

**Remark 3.9.** In Figures 15, 18 and 19 note that: Any two faces with an edge in common have different orbit portrait. (A single boundary point in common is not enough.) See the Edge Monotonicity Conjecture 3.27 which implies that the same statement is true in every tessellation  $\text{Tes}_q(\overline{\mathcal{S}}_p)$ .

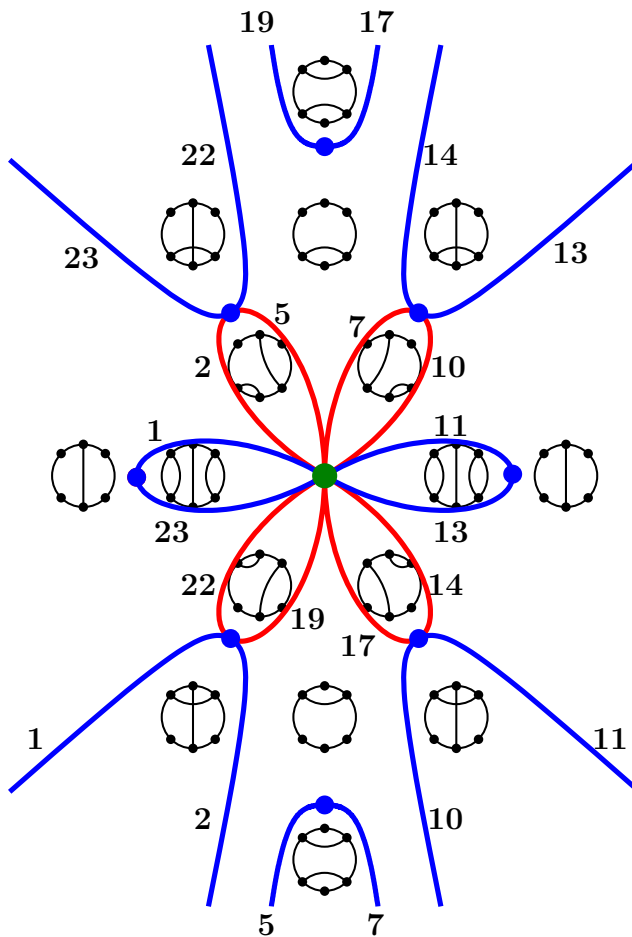


Figure 18: Cartoon showing the tessellation  $\text{Tes}_2(\overline{\mathcal{S}}_2)$ , together with the period 2 orbit portrait associated with each of the sixteen faces. Each of the co-periodic angles shown in this cartoon has denominator  $24 = 3d(2)$ . In this particular case, each face has a well defined critically periodic center point, and two faces have the same orbit portrait only if their center points have the same Julia set. (Compare Remark 3.15.)

**Definition 3.10 (Portrait Size).** By the *size*  $\varepsilon \geq 0$  of an orbit portrait we will mean the number of unordered pairs of distinct angles which are equivalent to each other. This is a convenient measure of the complexity of the portrait. Note that a collection of  $n$  mutually equivalent angles makes a contribution of  $n(n-1)/2$  to the size. Thus a portrait consisting of four rays meeting at a point has size six. As examples, the various portraits in Figure 18 have sizes 1, 2, 3, and 6.

**Definition 3.11 (Portrait Compatibility and Amalgamations).** By the *amalgamation* of two equivalence relations on the same set we will mean the smallest equivalence relation which contains both of them. For example the amalgamation of the orbit portraits  $\{1/8 \simeq 3/8\}$  and  $\{2/8 \simeq 6/8\}$  is a well behaved orbit portrait  $\{1/8 \simeq 2/8 \simeq 3/8 \simeq 6/8\}$ . (All three are visible in Figure 18.) However, the amalgamation of two orbit portraits although well defined as an equivalence relation, is not always a possible orbit portrait. In

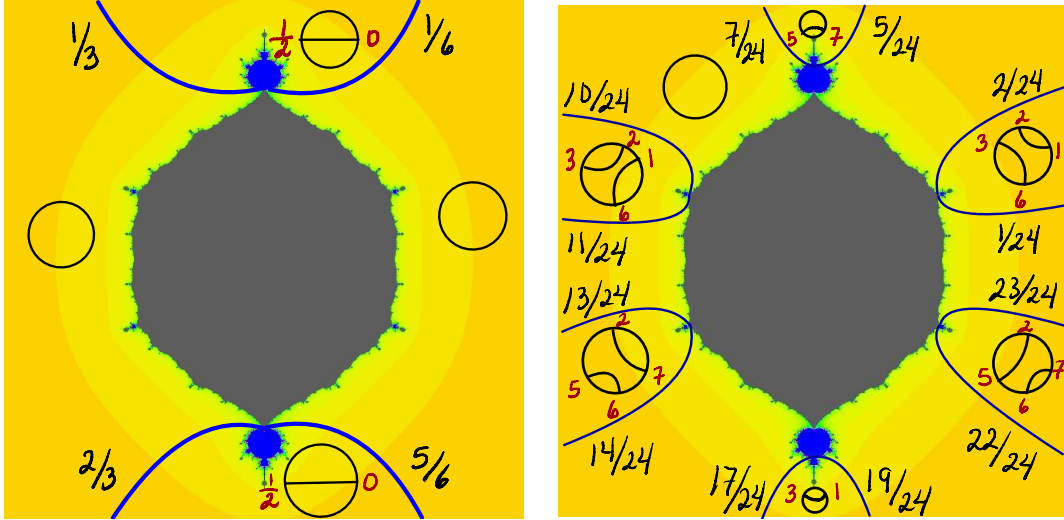


Figure 19: On the left, a picture of  $\text{Tes}_1(\overline{\mathcal{S}}_1)$ . Notice that the dynamic rays 0 and  $1/2$  land together for maps in the two primary wakes. On the right, a picture of  $\text{Tes}_2(\overline{\mathcal{S}}_1)$  (with common denominator  $d(2) = 8$  for orbit portraits). In both cases, the largest face containing the central region has trivial orbit portrait. The orbit portraits on the right are identical with those in the inner region of Figure 18, illustrating the duality between vertices of  $\text{Tes}_2(\overline{\mathcal{S}}_1)$  and  $\text{Tes}_1(\overline{\mathcal{S}}_2)$ .

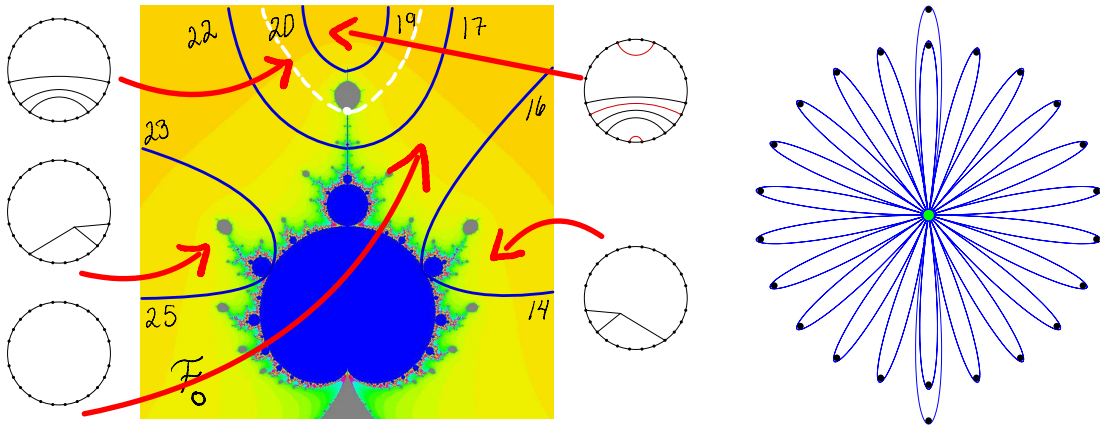


Figure 20: Left: The top part of the tessellation  $\text{Tes}_3(\overline{\mathcal{S}}_1)$  showing five faces, together with their period 3 orbit portraits. (The common denominator is  $3d(3) = 78$  for parameter rays, and  $d(3) = 26$  for dynamic rays.) The rest of the connectedness locus in  $\mathcal{S}_1$  can be seen above in Figure 19. The Type D components at the base of the two top faces are very small, and would be visible only under substantial magnification. For the dotted white rays, see Figure 29 and Remark 3.33.)

Right: An inverted picture of  $\text{Tes}_3(\overline{\mathcal{S}}_1)$  with the ideal point at the center, showing only the 48 parameter rays. Conjecturally the same pattern of co-period 3 rays landing together would occur in **any** zero-kneading region. Compare Figures 37 and 54 in Sections 3 and 4. There is an analogous conjecture for any co-period  $q$ . Compare the outer part of Figure 17 with Figure 19-right for the case  $q = 2$ . (See [BM] for a more detailed discussion.)

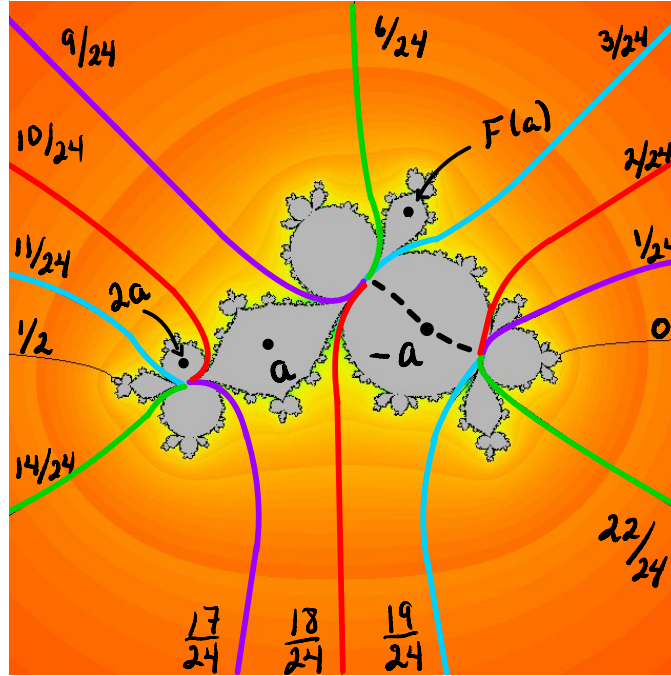


Figure 21: Julia set for a parabolic map  $F \in \mathcal{S}_2$ , with rays of angle  $10/24$ ,  $11/24$ ,  $14/24$  and  $17/24$  landing at the root point of the co-critical component  $U(2a)$ . These are the same as the angles of the parameter rays landing at the corresponding parabolic map. (See the bottom right quadrant of Figure 17.) Here the four ray colors correspond to the associated **triads**  $(\theta, \theta + 1/3, \theta + 2/3)$  of equally spaced angles. The associated periodic rays of angle  $3/4$ ,  $1/8$ ,  $1/4$ , and  $3/8$  land at the root point of the  $U(-a)$  component. (In this particular case, this is also the root point of the  $U(a)$  and  $U(F(a))$  components.) The remaining ray in each triad lands at the diagonally opposite boundary point of  $U(-a)$ . Here the walls corresponding to the pairs  $(1/24, 9/24)$  and  $(6/24, 22/24)$  separate  $a$  from  $F(a)$ , hence the corresponding parameter rays of angle  $17/24$  and  $14/24$  lie in the escape region with kneading invariant  $(1, 0)$ . On the other hand, the  $(2/24, 18/24)$  and  $(3/24, 19/24)$  do not separate, hence the  $10/24$  and  $11/24$  parameter rays lie in the  $(0, 0)$  region, as shown in Figure 17. There is an analogous figure for any parabolic point  $p \in \mathcal{S}_p$ , with a triad for each parameter ray landing at  $p$ . (Compare Remark 2.23.)

order to characterize which equivalence relations can be orbit portraits, we will need the following.

**Lemma 3.12.** *Suppose that three or more dynamic rays of period  $q$  land on a periodic point  $z$  of period  $q' < q$ . Then the cyclic order of the angles of these rays must be preserved under multiplication by  $3^{q'}$ . Hence these rays have a common well defined rotation number under the map  $F^{\circ q'}$ .*

*Proof.* This is clear since the map  $F^{\circ q'}$  maps a neighborhood of  $z$  diffeomorphically, preserving the cyclic order of the rays landing there.  $\square$

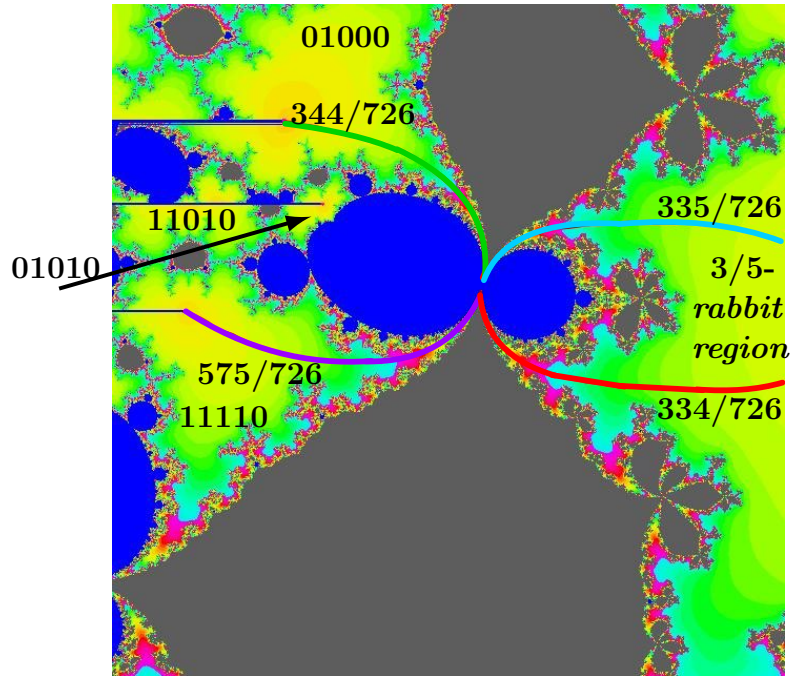


Figure 22: Part of the parameter curve  $\mathcal{S}_5$ , showing a parabolic point  $p$  which is on the boundary of three different escape regions, and showing the four rays of co-period 5 which land on it. These rays have been given four different colors, matching the corresponding colors in the Julia set picture (Figure 23). The two right hand rays are primary and lie in the  $3/5$  rabbit escape region; while the two on the left are secondary, and lie in two different escape regions. In fact there are four different escape regions on the left, labeled by their kneading invariants. (The three horizontal slits which terminate at ideal vertices are needed since the canonical coordinate is ramified at these points.) The four rays are labeled by their associated parameter angles. Note that each of the three escape regions which have  $p$  as boundary point contains at least one of these rays. There are actually hundreds of co-period 5 rays in each escape region (see Table 3 in Section 5), so the full picture of the tessellation within this square would be very complicated, even though each hyperbolic component is contained in a single face. For a more detailed picture of this region, see [BM].

**Example 3.13.** The orbit portrait  $\{1/8 \simeq 2/8 \simeq 3/8 \simeq 6/8\}$  described above is well behaved: The corresponding four rays must land at a common fixed point, and cyclic order is preserved by the tripling map  $\{1/8, 2/8, 3/8, 6/8\} \mapsto \{3/8, 6/8, 1/8, 2/8\}$ . However the larger equivalence relation  $\{1/8 \simeq 2/8 \simeq 3/8 \simeq 5/8 \simeq 6/8 \simeq 7/8\}$  cannot be an orbit portrait since the tripling map sends it to  $\{3/8, 6/8, 1/8, 7/8, 2/8, 5/8\}$ , completely confusing the cyclic order. More generally, for any  $q \geq 2$  it is not hard to check that the relation in which **all** period  $q$  orbits are equivalent can never be an orbit portrait.

By a *formal orbit portrait* we will mean any equivalence relation which satisfies the conditions of both Lemma 3.8 and Lemma 3.12. Conjecturally every formal orbit portrait is realized as an actual orbit portrait in  $\mathcal{S}_p$  for all sufficiently large  $p$ . (See Remark 3.14.)

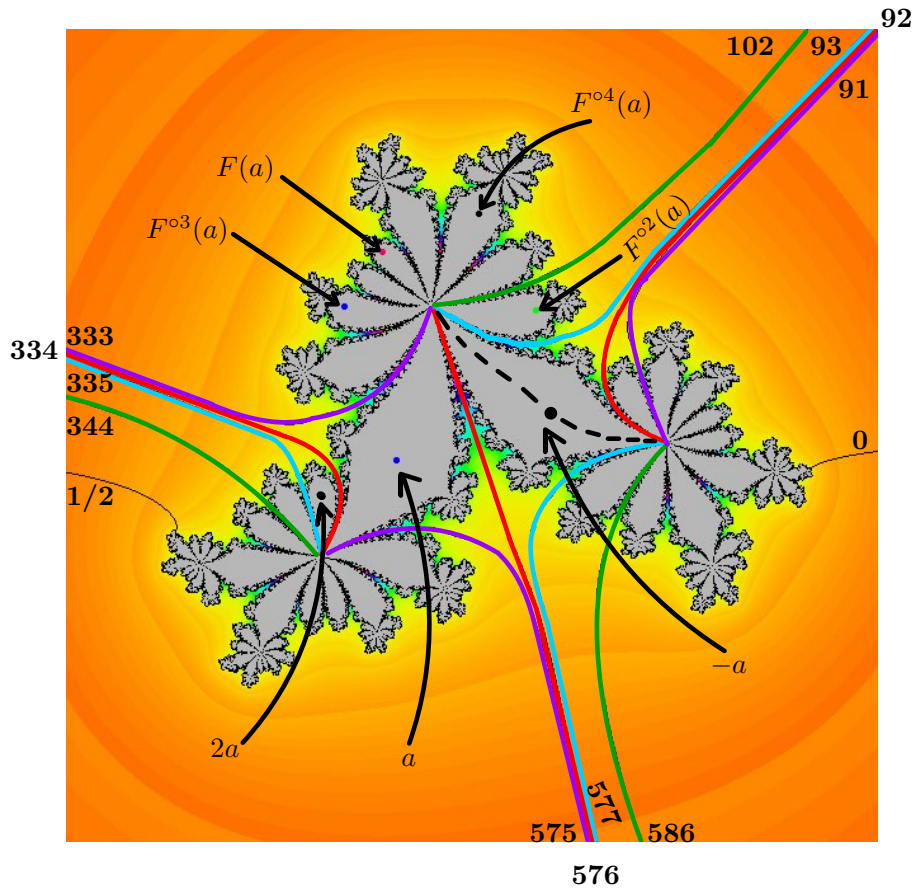


Figure 23: Julia set for the center of the right hand Type D component in Figure 22. (The corresponding picture for its parabolic root point  $p$  would be homeomorphic; but its components would be fatter and harder to separate.) Let  $\theta(1), \dots, \theta(4)$  be the angles for the four parameter rays landing at  $p$ . Then the corresponding dynamic rays of angle  $\theta(j)$  land, in the same cyclic order, at the root point of the  $U(2a)$  component to the lower left of the present figure. Similarly the corresponding periodic rays of angle  $\theta_5(j)$  land at the root point of the  $U(-a)$  component towards the top of the figure; while the associated co-periodic rays of angle  $\hat{\theta}_5(j)$  land at the opposite boundary point of  $U(-a)$ , to the lower right. The last eight rays, landing on the boundary of  $U(-a)$ , give rise to four different walls across this dynamic plane. The kneading invariants of the corresponding parameter rays can easily be computed, using Lemma 2.25 together with these walls. As one example, for the red wall, consisting of the 92 and 576 rays together with the dotted line, the entire orbit of  $a$  is contained in one complementary component; so the kneading invariant of the red  $334/726$  parameter ray is 00000, as shown in Figure 22. On the other hand the purple wall, consisting of the 91 and 333 rays connected by the dotted line, separates the marked point  $a$  from the rest of its orbit. Therefore the purple  $575/726$  parameter ray has kneading invariant 11110. There are actually ten different rays landing at the co-critical root point. For a discussion of how to tell which dynamic rays actually correspond to parameter rays, see [BM]. The primary parameter rays correspond to the co-periodic rays at both sides of the hyperbolic component that contains  $2a$  and that land at the root point of this component. The secondary parameter rays are the next closer ones to this component landing at the root point of the hyperbolic component of  $2a$ . Note that the dual map has an identical Julia set, but with the roles of  $+a$  and  $-a$  interchanged. (See Remark 2.30.)

Two or more orbit portraits of the same period  $q$  will be called *compatible* if they are contained in some common formal orbit portrait. This definition also makes sense for orbit portraits of different periods, providing that we allow mixed period orbit portraits. However note that two orbit portraits of different period are automatically compatible with each other. Evidently a collection of orbit portraits are compatible if and only if their amalgamation is a formal orbit portrait.

In many interesting cases, the orbit portrait of a face is the amalgamation of the orbit portraits of two neighboring faces. This seems to happen when the parabolic point  $\mathbf{p}$  of period  $p$  is in the boundary of two different escape regions in  $\mathcal{S}_q$ . Conjecturally,  $\mathbf{p}$  is the landing point of 3 or at most 4 parameter rays. (See Section 4.) For simple examples of this see Figure 18, and for more complicated examples see Figure 38.

**Caution.** If we choose two arbitrary period  $q$  orbit portraits, the amalgamation, although well defined as an equivalence relation, may not correspond to any possible orbit portrait. As an example, consider the three orbit portraits

$$\mathcal{O}_1 = \{1/8 \simeq 3/8\}, \quad \mathcal{O}_2 = \{2/8 \simeq 6/8\}, \quad \mathcal{O}_3 = \{5/8 \simeq 7/8\} .$$

The two-fold amalgamations  $\mathcal{O}_i \uplus \mathcal{O}_j$  all correspond to possible orbit portraits, which are visible in the outer part of Figure 18. However, as noted in Example 3.13, the three-fold amalgamation with  $\{1/8 \simeq 2/8 \simeq 3/8 \simeq 5/8 \simeq 6/8 \simeq 7/8\}$  does not correspond to any possible orbit portrait.

Note that the period  $q$  orbit portraits of a fixed map  $F$  for different periods  $q$  are always compatible with each other, so that their amalgamation is a well defined mixed period orbit portrait. As an example, the orbit portrait  $\{0 \simeq 1/2\}$  in Figure 15 is certainly compatible with the orbit portrait  $\{1/8 \simeq 3/8, 5/8 \simeq 7/8\}$  in Figure 18.

**Remark 3.14 (Problems).** This discussion raises at least two questions:

- Is every formal orbit realized by an actual orbit portrait in some  $\mathcal{S}_p$ , or are there additional constraints?
- If it is realized in a given  $\mathcal{S}_p$  can it always be realized in  $\mathcal{S}_{p+1}$  also?

Here are some examples. We see from Figures 18, 19-right and 34 that  $\{2 \simeq 7, 5 \simeq 6\}/8$  occurs as an actual orbit portrait in all three  $\mathcal{S}_1$ ,  $\mathcal{S}_2$  and  $\mathcal{S}_3$ . Similarly we see from Figures 24 and 36 that  $\{2 \simeq 5, 6 \simeq 15, 18 \simeq 19\}/26$  also occurs as an orbit portrait in all three  $\mathcal{S}_1$ ,  $\mathcal{S}_2$  and  $\mathcal{S}_3$ . However the orbit portrait

$$\{\{5 \simeq 14 \simeq 25\}/26, \{15 \simeq 16 \simeq 23\}/26, \{17 \simeq 19 \simeq 22\}/26\}$$

appears in  $\mathcal{S}_3$  but doesn't appear in  $\mathcal{S}_1$ ,  $\mathcal{S}_2$  or in  $\mathcal{S}_4$ .

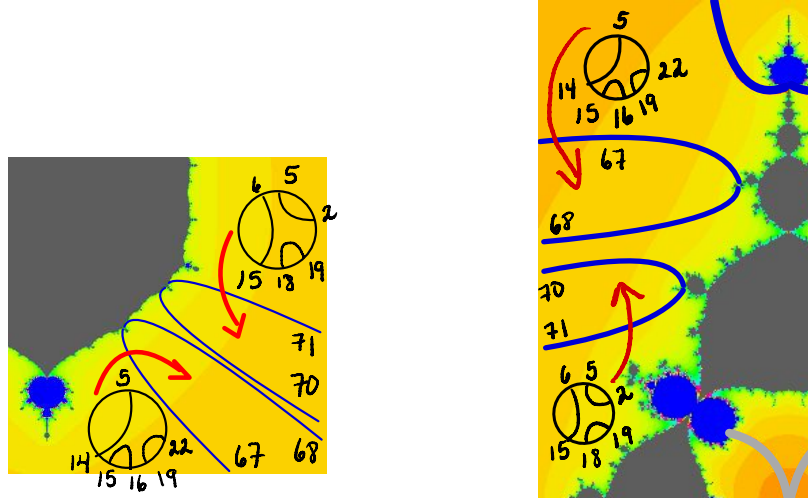


Figure 24: On the left, the bottom right of  $\mathcal{S}_1$  displaying the co-periodic angles  $70/78$  and  $71/78$  and its corresponding orbit portrait  $\{2 \simeq 5, 6 \simeq 15, 18 \simeq 19\}/26$ . On the right, the top left part of  $\mathcal{S}_2$  displaying the same orbit portrait and the same co-periodic angles. The same orbit portrait appears also in  $\mathcal{S}_3$ , see Figure 36. In this picture we also display the orbit portraits of the primary wakes in  $\mathcal{S}_1$  and  $\mathcal{S}_2$  corresponding to the co-periodic angles  $67/78$  and  $68/78$ . These orbit portraits are very different from the orbit portrait of the primary wake delimited by the same co-periodic angles in the airplane region in  $\mathcal{S}_3$ .

**Remark 3.15 (Examples of duality).** According to Remark 2.30, there is a natural one-to-one correspondence between hyperbolic components of Type D( $q$ ) in  $\mathcal{S}_p$  and hyperbolic components of Type D( $p$ ) in  $\mathcal{S}_q$ . The center points of two dual components actually represent the same polynomial map, and hence have the same Julia set. It follows of course that they have the same period  $h$  orbit portrait for any choice of  $h$ . As an example, there are six components of Type D(2) in  $\mathcal{S}_1$ , which are visible in Figure 19. Hence there are six corresponding components of Type D(1) in  $\mathcal{S}_2$ . These six components lie at the endpoints of the eight parameter rays in Figure 15; but it is easier to identify them by their period two orbit portraits, as shown in the central part of Figure 18. There are also eight components of Type D(2) in  $\mathcal{S}_2$  (see the outer parts of Figures 17 and 18). This yields four dual pairs with the same orbit portrait. Finally there are two large components of type B to the left and right of Figure 17 which are dual to each other, and hence have the same orbit portrait.

**Definition 3.16 (Edge Numbers).** We return to the study of tessellations. One very simple invariant of a face  $\mathcal{F}_k$  of a tessellation  $\mathbf{Tes}_q(\overline{\mathcal{S}}_p)$  is the number of its edges, counted with multiplicity. (By definition, an edge has multiplicity two if it is the only edge landing at a cusp point, so that we must traverse it twice as we follow the boundary of the associated face.) This edge number is always even, since ideal and parabolic vertices alternate as we traverse any component of the boundary of  $\mathcal{F}_k$ . Note that the sum of edge numbers over all faces is equal to twice the total number of edges. As an example, in Figure 15 the middle face  $\mathcal{F}_2$  has twelve edges counted with multiplicity, since each of the four edges in the middle is counted twice; while the top and bottom faces have two edges each.

As a very rough principle, faces with many edges will tend to have relatively small orbit portraits, since each additional parabolic boundary point will impose an additional upper bound on the associated orbit portrait. In fact the orbit portrait for any point of the face is contained in the orbit portrait for any parabolic boundary point. (Compare Corollary A.2 in Appendix A as well as the proof of the Edge Theorem 3.26.) In particular, faces with only two edges will tend to have larger orbit portraits.

**Definition 3.17 (Wakes).** The concept of wake is closely related to this discussion. Let  $H \subset \mathcal{S}_p$  be a hyperbolic component of Type D  $(q, p)$ . By definition,  $H$  has a *wake*  $W$  if  $H$  is contained in a simply-connected open subset  $W \subset \mathcal{S}_p$  which is bounded by two edges of  $\mathbf{Tes}_q(\overline{\mathcal{S}_p})$  which

- (1) lie in the same escape region  $\mathcal{E}$ , and
- (2) share a common parabolic landing point  $\mathfrak{p} \in \partial H$ .

A wake may consist of a single face of  $\mathbf{Tes}_q(\overline{\mathcal{S}_p})$ , in which case it is described as a *minimal wake*. Many examples of minimal wakes can be seen in Figures 15, 17 and 19.

But in many cases wakes may be *nested*, with one contained in another. For many examples of nested wakes, see Figure 30. Any wake which is not minimal must be made up out of two or more of the faces of the tessellation, together with all of the common boundary edges between two of these faces.

It will be convenient to say that a hyperbolic component  $H$  and an escape region  $\mathcal{E}$  are *adjacent* if they have infinitely many shared boundary points; or in other words if the intersection  $\overline{H} \cap \overline{\mathcal{E}}$  is infinite. Since every boundary point of a hyperbolic component must be a boundary point of at least one escape region, it follows that every hyperbolic component is adjacent to at least one escape region.

Here are two conjectural statements, which are true in every case that we have observed:

- (3) Any two parameter rays which are contained in the same escape region  $\mathcal{E}$ , and have a common parabolic landing point, bound a uniquely determined wake  $W = W(H)$  which intersects no escape region other than  $\mathcal{E}$ . In particular, the component  $H$  of Type D is uniquely determined.
- (4) Every Type D component which is adjacent to only one escape region  $\mathcal{E}$  must have a wake in  $\mathcal{E}$ .

On the other hand, it follows from (3) that a component  $H$  which is adjacent to two or more escape regions can never have a wake. See Figure 40 for examples of Type D components which are adjacent to two different escape regions.

Since no two parameter rays can intersect each other, it also follows from (3) that:

- (5) Any two wakes must be either disjoint or nested.

(This is true even if the wakes are associated with different values of  $q$ . As an example, the period two wake labeled by angle  $17/24$  and  $19/24$  at the top of Figure 17 is a subwake of the period one wake with angles  $2/3$  and  $5/6$  at the top of Figure 10.)

The complexity of the tessellation  $\mathbf{Tes}_q(\overline{\mathcal{S}}_p)$  increases rapidly as either  $p$  or  $q$  increase. For period  $q = 3$ , there are 48 angles of co-period three, all of the form  $j/26 \pm 1/3$  with denominator  $3d(3) = 78$ . (Compare Table 4 in Section 5.)

$\mathbf{Tes}_3(\overline{\mathcal{S}}_1)$  consists of a central lemon shaped hyperbolic component which is contained in a large face  $\mathcal{F}_0$  with trivial orbit portrait. It is surrounded by two pairs consisting of a wake and minimal subwake, together with 20 other minimal wakes. (Compare Figure 20-left for the top part of this tessellation, and Figure 20-right for a cartoon of this tessellation.)

$\mathbf{Tes}_3(\overline{\mathcal{S}}_2)$  consists of an annulus shaped face with trivial orbit portrait which separates the two escape regions, together with 24 faces in the inner  $(1, 0)$  escape region, and 24 in the outer basilica region. More precisely, the inner region contains six pairs consisting of wake and minimal subwake, plus twelve additional minimal wakes; while the outer region contain only two such pairs, plus twenty additional minimal wakes.

See Remark 3.34 for a detailed description of  $\mathbf{Tes}_1(\overline{\mathcal{S}}_3)$ ,  $\mathbf{Tes}_2(\overline{\mathcal{S}}_3)$  and  $\mathbf{Tes}_3(\overline{\mathcal{S}}_3)$ . In particular note that the statistics for the outer region of  $\mathbf{Tes}_3(\overline{\mathcal{S}}_2)$  are identical with those for the outer part of  $\mathbf{Tes}_3(\overline{\mathcal{S}}_1)$ , or for the airplane or rabbit regions of  $\mathbf{Tes}_3(\overline{\mathcal{S}}_3)$ . (Compare the Zero Kneading Conjecture in [BM], as well as Figures 20, 37, and 54.)

We will prove the following sharper version of Lemma 2.9. Let  $F$  vary over any one of the faces  $\mathcal{F}_k$  of  $\mathbf{Tes}_q(\overline{\mathcal{S}}_p)$ .

**Theorem 3.18 (Tessellation Landing Theorem).** *For each  $F \in \mathcal{F}_k$ , and each angle  $\theta_0 \in \mathbb{Q}/\mathbb{Z}$  of period  $q$  under tripling, the dynamic ray  $\mathcal{R}_F(\theta_0)$  lands at a repelling periodic point  $z(F) \in J(F) \subset \mathbb{C}$ . Furthermore, the correspondence  $F \mapsto z(F)$  defines a holomorphic function  $\mathcal{F}_k \rightarrow \mathbb{C}$ .*

*The orbit portrait for dynamic rays of period  $q$  is the same for all maps  $F \in \mathcal{F}_k$ .*

In particular, any two hyperbolic components contained in the same face must have the same period  $q$  orbit portrait, even if they are surrounded by different escape regions.

**Proof of Theorem 3.18.** Since  $\theta_0$  has period  $q$  under tripling, there are just three possibilities for a dynamic ray  $\mathcal{R}_F(\theta_0)$ . Either it lands on a repelling periodic point, or a parabolic point of ray period  $q$ , or it crashes into  $-a$  or some pre-image of  $-a$ . In the last case, some forward image of  $\mathcal{R}_F(\theta_0)$  would hit  $-a$  itself. But this would mean that  $F$  lies on a parameter ray of co-period  $q$ , or in other words to the edge of the period  $q$  foliation. Since  $F$  belongs to a face by hypothesis, this Case cannot occur.

There are only finitely many parabolic maps of ray period  $q$  in  $\mathcal{S}_p$ . This means there is at worst a finite subset  $X \subset \mathcal{F}_k$  of such points. Thus for all  $F \in \mathcal{F}_k \setminus X$  the  $\theta_0$  ray must land on a repelling fixed point of the iterate  $F^{\circ q}$ . The multiplier  $\lambda_F$  of this fixed point depends holomorphically on  $F$ . Thus we have a holomorphic map  $F \mapsto \lambda_F$  from  $\mathcal{F}_k \setminus X$  to  $\mathbb{C} \setminus \overline{\mathbb{D}}$  for each choice of  $\theta_0$ .

But it is not hard to check that the multipliers of fixed points of  $F^{\circ q}$  are bounded on any compact subset of  $\mathcal{S}_p$ . Therefore the ‘‘singularities’’ of the map  $F \mapsto \lambda_F$  at the points of  $X$  are removable. In other words, we can extend to a holomorphic function from  $\mathcal{F}_k$  to  $\mathbb{C} \setminus \overline{\mathbb{D}}$ . In fact, by the minimum modulus principle, it must actually take values in  $\mathbb{C} \setminus \overline{\mathbb{D}}$ .

But this leads to a contradiction. Given any  $F_0 \in X$ , choose a sequence of maps  $F_j \in \mathcal{F}_k \setminus X$  which converge to  $F_0$ . Passing to an infinite subsequence, we can assume

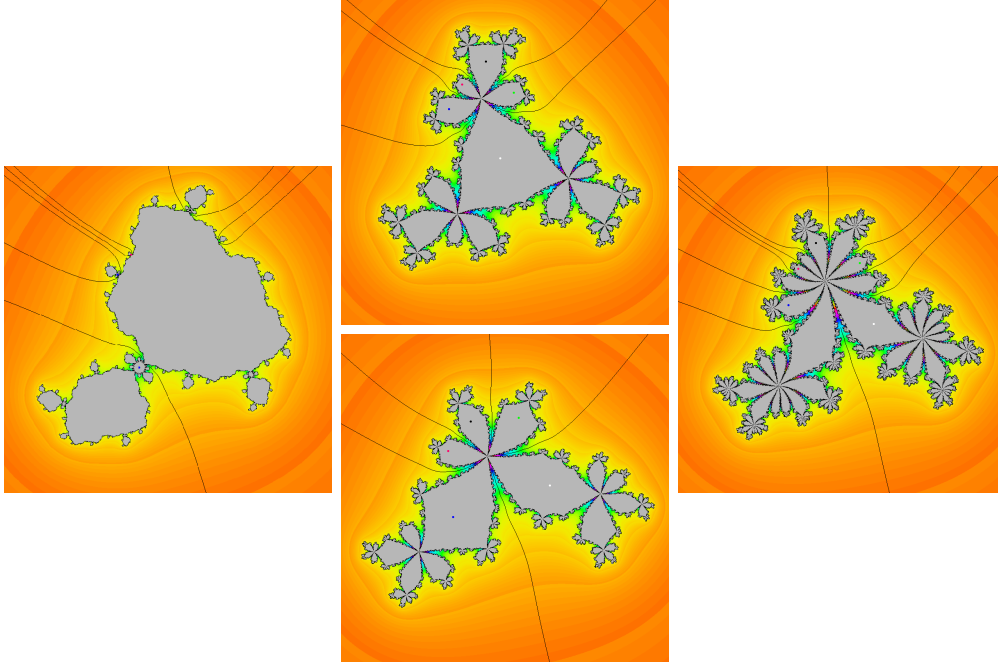


Figure 25: Julia sets for maps in the four hyperbolic components surrounding the parabolic map in Figure 22; and belong to four different faces of  $\mathbf{Tes}_5(\overline{\mathcal{S}}_5)$ . The left component of Type D and period one has trivial period 5 orbit portrait. The top and bottom figures, of Type A and B respectively, each have a cycle of 5 periodic rays landing at the middle fixed point; but these are different cycles. For the right hand figure, of Type D and period 5, both of these cycles of rays land at the same point. The Julia set of the parabolic map (Figure 23) is topologically equivalent to the right hand figure. (Here we can hope to understand the local tessellation; but it would hardly be possible to understand the full  $\mathbf{Tes}_5(\overline{\mathcal{S}}_5)$ , with its 38400 edges. Compare Section 5.)

that the landing points of the associated dynamical  $\theta_0$ -rays converge to a limit point  $z_0$ . Evidently the multiplier  $\lambda$  of  $F_0$  at  $z_0$  satisfies  $|\lambda| > 1$ . This contradicts the hypothesis that the landing point of the  $\theta_0$  ray is parabolic. This shows that the set  $X$  must be empty; and completes the proof of Theorem 3.18.  $\square$

**Corollary 3.19.** *Every parabolic map  $F_0 \in \mathcal{S}_p$  is the landing point of at least one co-periodic ray.*

*Proof.* Choose a parabolic periodic point  $z_0$  for  $F_0$ , and a dynamic ray  $\mathcal{R}_{F_0}(\theta)$  landing at  $z_0$ . (For the existence of such a ray, see the beginning of §2.) Let  $q$  be the period of this ray. Then  $F_0$  cannot belong to one of the sets  $\mathcal{F}_k$  in the co-period  $q$  tessellation of  $\mathcal{S}_p$ . In fact, by Theorem 3.18, any landing point of a period  $q$  dynamical ray in  $\mathcal{F}_k$  is repelling. It follows that  $F_0$  must be one of the vertices of  $\mathbf{Tes}_q(\overline{\mathcal{S}}_p)$ , the period  $q$  tessellation; and hence must be the landing point of some co-period  $q$  parameter ray.  $\square$

We have seen in Theorem 3.18 that the correspondence  $F \mapsto \mathcal{O}_q(F)$  is constant throughout each period  $q$  region  $\mathcal{F}_k$ .

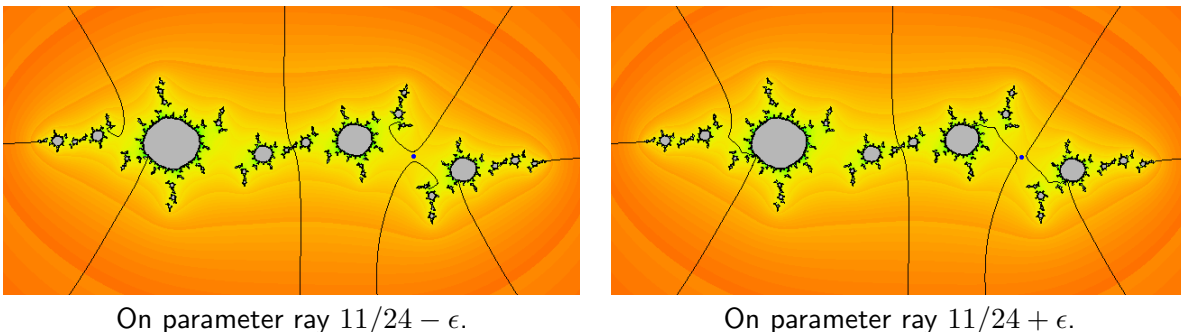


Figure 26: The parameter angle  $11/24 = 1/8 + 1/3$  is co-periodic. On the left, for a map on the parameter ray of angle  $11/24 - \epsilon$ , the  $1/8$  dynamic ray (which is periodic of period two) bounces up, away from the free critical point  $-a$ , and lands on the Julia set. Similarly its pre-image, the  $3/8$  ray is pushed up, while the other pre-image, the  $19/24$  ray is pushed down, so that both land on the Julia set. For a map precisely on the  $11/24$  parameter ray, the  $1/8$  and  $19/24$  rays would crash together. However, after we cross the  $11/24$  ray, the  $1/8$  and  $3/8$  rays both bounce to the right, so as to share a landing point with the  $7/8$  and  $5/8$  rays respectively. Thus the period two orbit portrait jumps in size from one to three. Note that only the  $1/8$  ray and its iterated preimages jump discontinuously as we cross the  $11/24$  parameter ray. All other dynamic rays vary continuously.

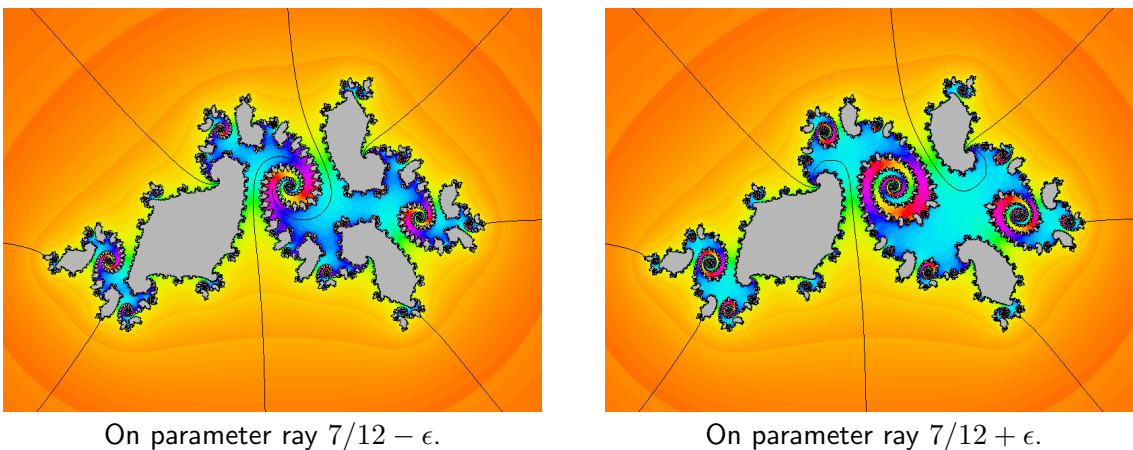


Figure 27: The landing points of both the  $1/4$  and  $3/4$  rays jump discontinuously as we cross the  $7/12$  ray.

**Lemma 3.20 (Crossing a Parameter Ray).** *If the map  $F$  lies precisely on a parameter ray with co-periodic angle  $\psi$ , then the two dynamic rays of angle  $\psi \pm 1/3$  crash together at the critical point  $-a$ . This pair of rays divides the dynamic plane into two simply-connected open sets  $U$  and  $V$ . Now consider a one-parameter family of maps which cross over this parameter ray. Just before the crossing, the two dynamic rays will bounce in opposite directions, so that one lands at a periodic point in  $U$  and the other lands in a periodic point in  $V$ . After the crossing, the roles are reversed, so that the dynamic ray which formerly landed in  $U$  will now land in  $V$  and vice versa.*

We will not provide any detailed argument; but examination of examples such as Figures 26 through 28 illustrate this behavior.  $\square$

It is important to emphasize that a period  $q$  dynamic ray for a map  $F$  in an escape region nearly always lands on a periodic point of ray period  $q$ . This fails to be true only in the cases where the map  $F$  lies precisely on a parameter ray of co-period  $q$ , or on the iterated pre-image of such a ray, so that the dynamic ray crashes into a critical or pre-critical point. Similarly periodic points nearly always vary continuously as functions of the map  $F$ . This fails to be true only when  $F$  is a parabolic map.

What can happen as we cross a parameter ray of co-period  $q$  is that the rotation number of the former landing point of the ray changes, so that the ray period increases, and this point no longer plays any role in orbit portraits of period  $\leq q$ .

**Definition 3.21.** The *grand orbit* of a co-periodic angle  $\psi$  under angle tripling will be denoted by  $((\psi))$ . This consists of all of the periodic points  $\psi_j$ , together with all of their iterated pre-images under angle tripling. (If the period  $q$  has been specified, then a convenient identifying label for the grand orbit is the minimum of the angles  $0 < \psi_j < 1$ , multiplied by the common denominator  $3^q - 1$ .)

**Corollary 3.22 (The cycle of jumping rays).** *As we cross any parameter ray with angle  $\psi$  of co-period  $q$ , the landing point of a dynamic ray will jump discontinuously if and only if its dynamic angle belongs to the grand orbit  $((\psi))$ . In particular, a periodic ray will jump if and only if its angle is one of the  $\psi_j$ . For all periodic or preperiodic angles which are not in this grand orbit, the landing point will vary continuously as a function of the point  $F$  in  $\mathcal{S}_p$ .*

The proof is straightforward.  $\square$

As an immediate consequence of Lemma 3.20, we obtain the following statement.

**Theorem 3.23.** *Let  $\mathfrak{R}$  be a parameter ray with angle  $\psi$  of co-period  $q$ . Suppose that for maps on one side of  $\mathfrak{R}$  there is a dynamic ray with angle belonging to the cycle  $\{\psi_j\}$  which shares a landing point with a dynamic ray of some other angle (necessarily also of period  $q$ ). Then after crossing the parameter ray these two dynamic rays will no longer share a landing point. Thus the period  $q$  orbit portrait will definitely change.*

*Proof.* There are three possible cases. If the other angle is not in the same periodic cycle, then its ray will not jump, and the conclusion follows immediately from Lemma 3.20.

Now suppose that the two rays belong to the same periodic cycle, and hence both jump. Then at the exact crossing point we will have two different pairs of dynamic rays crashing together, as illustrated in Figure 28 (upper right), dividing the plane into three regions. We claim that these two periodic dynamics rays must be oriented in opposite directions, as in Figures 27 and 28. Hence as we cross the parameter ray in one direction both periodic dynamic rays will jump into the middle region, where they will find a common landing point by hypothesis. But crossing in the other direction they will jump into the two outer regions, and can never land together.

If on the other hand these two rays were oriented in the same direction, then after crossing to either side of the parameter ray they would always jump into different regions, and could never share a landing point.  $\square$

**Note.** The concept of an edge  $E$  of the tessellation  $\text{Tes}_q(\overline{\mathcal{S}}_p)$  is of course completely equivalent to the concept of a parameter ray  $\mathfrak{R}$  of co-period  $q$  in  $\mathcal{S}_p$ . However, since we want to discuss tessellations, it will be convenient to switch to the edge terminology.

**Definition 3.24 (The three kinds of edge in  $\text{Tes}_q(\overline{\mathcal{S}}_p)$ ).** Using the discussion above, we can separate the edges  $E$  of the tessellation  $\text{Tes}_q(\overline{\mathcal{S}}_p)$  into three fundamentally different cases, as follows. Let  $\psi$  be the co-periodic angle of  $E$ .

**Case 0.**  $E$  is *inactive*: For neighboring maps on either side of  $E$ , no dynamic ray with angle in the cycle  $\{\psi_l\}$  shares a landing point with any other dynamic ray. In other words, throughout some neighborhood of  $E$  there is no non-trivial orbit relation involving any angle in this cycle.

It follows that the period  $q$  orbit portrait is the same on both sides of  $E$ .

**Case 1.**  $E$  is a *primary edge*: For maps on one side of  $E$  every ray with angle in  $\{\psi_j\}$  shares a landing point with at least one other dynamic ray (which itself may or may not have angle in this cycle); but for maps on the other side, no ray with angle in  $\{\psi_j\}$  shares a landing point with any other ray.

It follows that the change of orbit portraits between the two sides is strictly **monotone**: The orbit portrait on one side is a proper subset of the orbit portrait on the other side.

**Case 2.**  $E$  is a *secondary edge*: Every ray with angle in  $\{\psi_j\}$  on either side shares a landing point with at least one other ray. (Therefore the other ray or rays on one side must be disjoint from those on the other side.)

It follows that the change of orbit portrait is strictly **non-monotone**: Neither orbit portrait contains the other.

Many examples of each of the three cases will be provided in the pages which follow; but here are some preliminary examples.

**Inactive Edges.** These will usually be colored gray. As examples there are four such edges in Figure 15, and many others in Figures 31, 32 and 34.

**Primary Edges** will usually<sup>5</sup> be colored blue. These occur in every tessellation. See for example Figures 15, 17, 33, 35.

**Secondary Edges** will usually be colored red. These occur in every tessellation with  $q = p > 1$ , and for many with  $q \neq p$  and  $p, q > 1$ . See Figures 17, 33, 35.

---

<sup>5</sup>One exceptional case is Figure 22 where the ray colors are chosen to match the colors of the corresponding triad in the associated Julia set picture.

In particular, a wake will be called either primary or secondary according as its edges are primary or secondary. In  $\mathbf{Tes}_2(\overline{\mathcal{S}}_2)$  (Figures 17 and 18), the six wakes in the outer basilica region are primary, while the inner region with kneading  $(1, 0)$  contains two primary wakes and four secondary wakes. In  $\mathbf{Tes}_2(\overline{\mathcal{S}}_3)$ , Figure 33 shows 32 wakes, of which 28 are primary. (The four secondary wakes are all located in the  $100\pm$  regions, near the  $x$ -axis.) Figure 30 shows several examples of sub-wakes, which are necessarily primary.

**Remark 3.25.** Empirically it is very easy to distinguish between the three different kinds of edge without computing a single orbit portrait, just by looking at the local geometry near the parabolic endpoint. See Theorem 3.26 and Conjecture 3.27 below.

First note that, in practice every parabolic vertex  $\mathbf{p}$  in  $\mathbf{Tes}_q(\overline{\mathcal{S}}_p)$  is the *root point* of a unique hyperbolic component  $H = H_{\mathbf{p}}$  which has Type  $D(q, p)$ . (This means that each map  $F \in H$  has an attracting orbit of period  $q$  which is disjoint from the marked periodic orbit of period  $p$ .) Such a component  $H$  is conformally isomorphic to the open unit disk  $\mathbb{D}$  by mapping each  $F \in H$  to the multiplier of this period  $q$  orbit. (See for example [M1].) In our cases this conformal isomorphism always seems to extend to a homeomorphism from the closure  $\overline{H}$  onto the closed unit disk  $\overline{\mathbb{D}}$ . By definition, the *root point*  $\mathbf{p}$  of  $H$  is the unique parabolic boundary point for which this multiplier is  $+1$ .

By Corollary 3.19 every parabolic vertex of the tessellation is the endpoint of at least one edge.

**Theorem 3.26 (Edge Theorem).**

- (1) *If there is only one edge  $E$  of  $\mathbf{Tes}_q(\overline{\mathcal{S}}_p)$  with  $\mathbf{p}$  an endpoint, then  $E$  is an inactive edge.*
- (2) *If there are two or more edges landing at  $\mathbf{p}$ , which is the root point of  $H$ , then the two which are closest to  $H$  are primary edges.*

In fact Statement (1) is obvious since both sides of  $E$  belong to the same face. The proof of Statement (2) will be given later in this section. Here is an example to illustrate Statement (2): In Figure 22, taking  $H$  to be the small disk enclosed by the blue and red rays, we see that these two rays must be primary.

We will assume Conjecture MC1 in Remark 2.28, which asserts that:

Every parabolic point  $\mathbf{p}$  of ray period  $q$  is the root point of one and only one hyperbolic component  $H = H_{\mathbf{p}}$  of Type  $D$ .

We will also assume the following.

**Conjecture 3.27 (Edge Monotonicity Conjecture).** *There can be at most four edges with a given parabolic endpoint  $\mathbf{p}$ . If there are two or more such edges, then the two edges which are closest to  $H_{\mathbf{p}}$  are primary edges, so that the orbit portrait increases monotonically as we cross into the face containing  $H_{\mathbf{p}}$ . Any further edges are secondary. Furthermore a primary edge and a secondary edge with the same parabolic endpoint always lie in different escape regions.*

One easy consequence of this conjecture is the following:

The parabolic endpoint of every secondary ray must be a common boundary point between two or more escape regions.

For example, there can be no secondary edges in  $\mathcal{S}_1$  since there is only one escape region. Another easy consequence is the following:

If  $\mathbf{p}$  is a parabolic boundary point of the escape region  $\mathcal{E}$  then at most two parameter rays from  $\mathcal{E}$  can land at  $\mathbf{p}$ . (There is always at least one such ray. See Arfeux and Kiwi [AK] Theorem 5.8; and compare Remark 3.28 and Lemma 3.29.)

Another important consequence is that  $E$  is inactive only if it is a “dead end” edge which does not share its parabolic endpoint with any other edge. A completely equivalent statement is the following:

Any two faces which have an edge in common must have different orbit portraits.

Furthermore:

Any face with trivial orbit portrait must be bounded by primary edges.

(See Figures 15, 32 and 34.)

Arfeux and Kiwi [AK, Section 5] have proved that every parabolic boundary point of an escape region is the landing point of at least one parameter ray in that region. It seems likely that every parabolic point which is not the cusp point of a Mandelbrot copy is the landing point of at least two parameter rays. We can try to make this more precise as follows.

**Remark 3.28 (Accessibility).** Let  $\mathbf{p}$  be a boundary point of an escape region  $\mathcal{E} \subset \mathcal{S}_p$ . By definition,  $\mathbf{p}$  is *accessible* from  $\mathcal{E}$  if there exists a Jordan path in  $\mathcal{E} \cup \{\mathbf{p}\}$  with endpoint  $\mathbf{p}$ . More precisely, we can define an *access* to  $\mathbf{p}$  from  $\mathcal{E}$  as a homotopy class of such paths.

**Lemma 3.29.** *For every access to  $\mathbf{p}$  from  $\mathcal{E}$ , there exists one and only one parameter ray<sup>6</sup> in  $\mathcal{E}$ , necessarily co-periodic, which lands on  $\mathbf{p}$ .*

*Proof.* Choose such an access path  $\alpha : [0, 1] \rightarrow \mathcal{E} \cup \{\mathbf{p}\}$  with  $\alpha(0) = \mathbf{p}$ . For every  $t > 0$  there exists a unique angle  $\theta$  such that the  $\theta$  parameter ray passes through  $\alpha(t)$ . Choose a sequence  $\{t_j\}$  converging to zero. After passing to a countable subsequence, we may assume that the associated angles  $\theta_j$  converge to a limit  $\theta_0$ . Evidently this limit ray must land on  $\mathbf{p}$ . It follows that the angle  $\theta_0$  is co-periodic. If it were irrational, then there would be an irrational dynamic rays landing on the parabolic orbit, which is impossible. Therefore, by Theorem 2.7, it is co-periodic. It is unique since there cannot be two rays landing at the same point without some part of the connectedness locus between them.  $\square$

The proof of Theorem 3.26 will depend on two preliminary statements.

---

<sup>6</sup>Caution: The corresponding statement for dynamic rays is false if we allow Julia sets which are not connected. In Figure 62, we show a connected Julia set where there are infinitely many accesses to the central point, but only four rays landing there.

**Lemma 3.30.** *The period  $q$  orbit portrait for the root point  $\mathfrak{p}$  of a hyperbolic component  $H$  of Type  $D(q)$  is identical to the period  $q$  orbit portrait for any map  $F$  in the interior of  $H$ .*

In other words, two or more dynamic rays for the map  $\mathfrak{p}$  land together at a periodic point for this map if and only if the corresponding rays for any  $F \in H$  will land together at a periodic point of  $F$ . This can be proved by Haisinski surgery.<sup>7</sup>  $\square$

We will also need the Upper Semi-Continuity Corollary of Appendix A which states that:

The orbit portrait for any map in a neighborhood of  $\mathfrak{p}$  is a subset of the orbit portrait for  $\mathfrak{p}$ .

*Proof of Theorem 3.26.* We know that the orbit portrait must change as we move out of the face containing  $H$  by crossing one of the two bounding edges near  $\mathfrak{p}$ . Since the change is monotone by upper semi-continuity, both of these rays must be primary.  $\square$

Although the fact that an edge is secondary tells us exactly which dynamic rays jump, it does not provide much information about where they jump to. For a more explicit discussion of the precise changes in orbit portrait as we cross an edge of the tessellation, see Section 4.

Diagrams such as Figure 18 provide a great deal of information about changes in the orbit portrait as we cross an edge (= parameter ray). Note that there are twenty four edges shown in this figure. Sixteen of these are primary, so that the orbit portrait is replaced by a proper subset of itself as we cross the ray in the right direction. But for the remaining eight, all in the inner escape region, there is a more complicated behavior. (Again compare Section 4.)

How does the change actually take place? Two of these twenty four cases are illustrated in Figures 26 through 28. If we cross  $11/24$  parameter ray of the internal escape region of  $\mathcal{S}_2$ , the change seems relatively easy to understand. (Compare Figure 26.) Note that

$$\frac{11}{24} = \frac{1}{8} + \frac{1}{3},$$

where  $1/8$  has period two under tripling. As we cross this ray in the direction of increasing parameter angle, the landing point of the  $7/8$  dynamic ray varies continuously; but the landing point of the  $1/8$  rays jumps discontinuously to join it. Thus the orbit portrait jumps to a larger orbit portrait which contains the original one. More generally, all of the preimages of the  $1/8$  ray under iterated angle tripling behave in the same way. For example the landing point of the  $3/8$  ray jumps to the landing point of the  $5/8$  ray, which varies continuously. However, the landing points of all rays which are not iterated pre-images of  $1/8$  vary continuously. For example the  $1/4$  and  $3/4$  rays land together throughout this

---

<sup>7</sup>See [H1], [H2]. For example Kawahira in the sketch of [Ka1, Theorem 2.1] says that “To check the dynamical stability on the Julia sets, we check the stability of the ray equivalence, which is defined by shared landing points of external rays.”

transition. However the period two orbit portrait jumps to a larger orbit portrait which contains the original one.

The transition as we cross the parameter ray of co-critical angle

$$\theta = \frac{14}{24} = \frac{7}{12} = \frac{1}{4} + \frac{1}{3}$$

in the inner  $\overline{10}$  escape region<sup>8</sup> seems harder to understand. (See Figure 27.) Only the dynamic rays of angle  $1/4$  and  $3/4$  (and their preimages) jump discontinuously, and yet we obtain a new orbit portrait which neither contains nor is contained in the original one.

Figure 28 helps to provide a more detailed understanding of what is happening. Here we use a different coloring algorithm: Within the basin of infinity, the color depends on the value of the  $F$ -invariant angular variable

$$\log_3(\mathbf{g}_F(z)) \pmod{\mathbb{Z}}.$$

Here  $\mathbf{g}_F(z)$  stands for the Green's function for  $F$ , which is multiplied by  $d = 3$  if we replace  $z$  by  $F(z)$ . This coloring is useful since it makes it easier to see the critical and precritical points, which are located in the centers of red cross shaped configurations.

Each map in the central escape region has three repelling fixed points. There is the landing point of the zero ray to the right and the  $1/2$  ray to the left, and there is also a central fixed point. Generically this central fixed point is the landing point of finitely many dynamic rays, which map to each other with a well defined rational rotation number. (Compare the Rotation Number Section in [BM].)

There are infinitely many precritical points in each of the two spiral channels leading to the central repelling point. For parameter angles in the open interval  $5/12 < \theta < 7/12$  (top left in Figure 28), the  $1/4$  dynamic ray misses these precritical points, which act as local repellers. If  $\theta = 7/12$ , then the  $1/4$  dynamic ray crashes into the free critical point (top right). However if  $\theta > 7/12$ , then the  $1/4$  ray is pushed to the right and lands at the same point as the  $1/8$  ray. For each rational rotation number  $\rho = m/n$  in an interval  $(1/2, 1/2 + \epsilon)$  there is:

- (1) an angle  $\theta_\rho$  of rotation number  $\rho$  under tripling, and
- (2) an entire open interval of  $\theta$  values around  $\theta_\rho$  such that the  $n$  dynamic rays with angle of the form  $3^j\theta_\rho$  manage to wiggle through the spiral to land at the central fixed point.

(The figure illustrates the case  $m/n = 5/9$ .) At both endpoints of such an interval of constant rotation number, these  $n$  rays crash into  $n$  pre-critical points (visible as the centers of red X shaped configurations). For  $\theta$  values in the complementary Cantor set, if we exclude those which are endpoints of intervals of constancy, the rotation number is irrational, and infinitely many dynamic rays land on the central fixed point.

However, unless  $\theta$  is one of the countably many co-periodic angles, some dynamics rays will manage to wobble through the various narrow channels to land at the central fixed point,

---

<sup>8</sup>There is similar behavior at the inner  $2/24, 5/24, 7/24, 10/24, 17/24, 19/24,$  and  $22/24$  rays. All of the crossings in the outer (basilica) region are monotone.

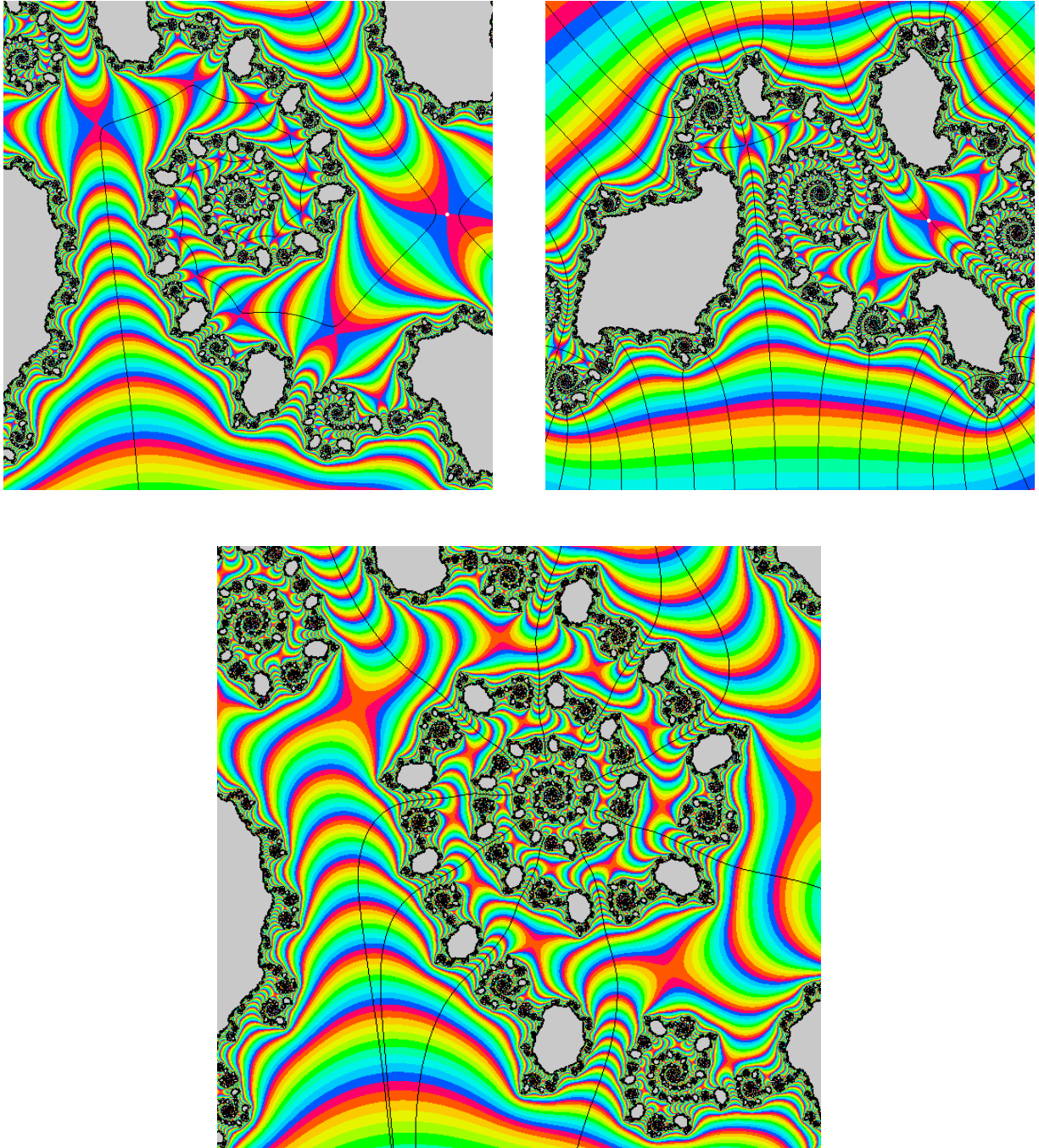


Figure 28: A more detailed view of the crossing in Figure 27, using a different coloring scheme. Top Left: For  $\theta < 7/12$  the dynamics rays of angle  $1/4$  and  $11/12$  come close to the free critical point  $-a$  and shoot off in opposite directions, so that the  $1/4$  ray (like the  $3/4$  ray) spirals into the central fixed point, which has rotation number  $\rho = 1/2$ . Right: if  $\theta = 7/12$ , the rays of angle  $1/4$  and  $11/12$  crash together at  $-a$ . Below: For  $\theta > 7/12$ , the  $1/4$  and  $3/4$  rays land on a period two orbit, while the central fixed point has a rotation number  $\rho > 1/2$  which varies continuously with  $\theta$ .

with rotation number  $1/2 < \rho < 1$ . The lower part of Figure 28 shows the special case where the rotation number is  $5/9$ , so that nine rays land.

**Note.** We have described what is happening in Figure 28 in some detail; but there is actually a similar problem in understanding Figure 27. The problem in both cases is that the period  $q$  orbit portraits are only aware of periodic orbits of ray period  $q$ . If the ray period changes, then, although orbit itself will usually vary continuously, anything involving that orbit will disappear from the orbit portrait. However, the ray period can change, only if the rotation number of the first return map to the periodic point changes. Since rotation numbers change continuously, it follows that any change must involve VERY large denominators, and hence VERY large ray periods.

In Figure 28 the change involves a fixed point. We will see in the Rotation Number Section of [BM] that the rotation numbers of fixed points are relatively easy to deal with, but in Figure 27 the change involves a period two orbit. In fact on the left side of this figure the  $1/8$  and  $3/8$  rays land on a period two orbit. On the right side, this period two orbit still exists; but its rotation number has changed. The first return map  $F^{\circ 2}$  now has degree nine; and the computational problems involved in understanding exactly what happens become much more difficult.

Thus to understand what is happening, we need to consider not only period two orbits, but orbits of arbitrary period. The central repelling fixed point remains “visible from infinity” as the co-critical angle increases. That is, there are always dynamic rays which land at this point (except at the countably many co-periodic angles, where the appropriate dynamic rays crash into precritical points). In fact, for an entire Cantor set of co-critical angles, there are infinitely many dynamic rays landing at the fixed point. The concept which unifies all of these cases is the *rotation number*  $\rho$  of this fixed point, which varies continuously as a function of  $\theta$ , with an interval of constancy for each rational rotation number. For further details, see [BM].

If we assume the Edge Monotonicity Conjecture 3.27, then it follows that every wake is either *primary*, bounded by two primary edges, or *secondary*, bounded by two secondary edges. Furthermore it follows that every primary wake contains a component  $H$  of Type D which has  $\mathfrak{p}$  as its root point. (Similarly a secondary wake always seems to contain a component of Type D with  $\mathfrak{p}$  as a boundary point; but never as its root point.)

**Remark 3.31.** Still assuming Conjecture 3.27, if  $W$  is a subwake of some other wake  $W'$ , then  $W$  is necessarily a primary wake, since the parabolic endpoint  $\mathfrak{p}$  for  $W$  has an open neighborhood  $W'$  which intersects only one escape region.

Evidently the orbit portrait is not constant throughout a wake unless it is a minimal wake: The orbit portrait always becomes strictly larger every time we pass to a sub-wake. Examples are easy to find. Thus Figures 17 and 18 clearly show twelve wakes, each consisting of a single face.

Although we are primarily concerned with wakes for a given period  $q$ , it is certainly possible to consider nested wakes which do not have the same value of  $q$ . Such wakes of different period still have the basic constraint that they must be either nested or disjoint. For example the period  $q = 1$  wake bounded by the  $2/3$  and  $5/6$  rays in Figure 15 contains the period  $q = 2$  wake bounded by the  $17/24$  and  $19/24$  rays in Figure 17 or 18.

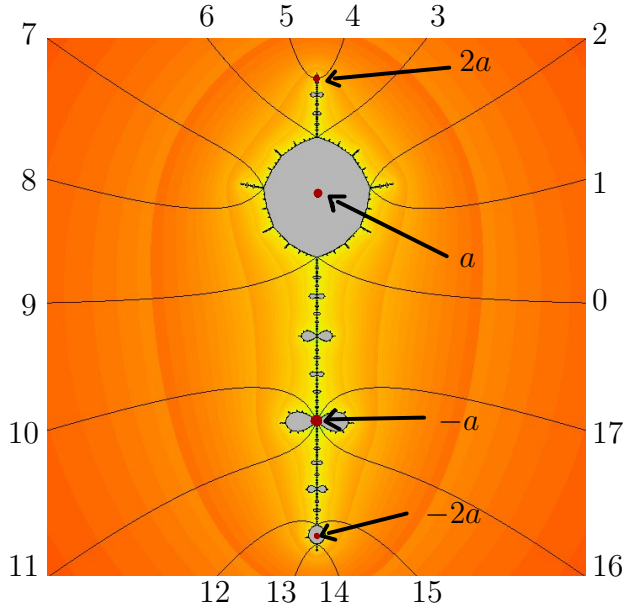


Figure 29: The Julia set for a Misiurewicz map  $F$  in  $\mathcal{S}_1$ . The  $4/18$  and  $5/18$  parameter rays in  $\mathcal{S}_1$  (indicated by dotted white curves in Figure 20) land at this map. Note that these angles are rational, but not co-periodic. These two rays bound a simply connected open subset of  $\overline{\mathcal{S}_1}$ ; but this set is not a wake. See Remark 3.33. Here for example

$$\{4, 10, 16\}/18 \mapsto 12/18 \mapsto 0 \curvearrowright \quad \text{and} \quad \{5, 11, 17\}/18 \mapsto 15/18 \mapsto 9/18 \curvearrowright .$$

**Remark 3.32 (Shared Faces).** Every tessellation contains two essentially different kinds of face. For  $p > 1$ , the distinction is between *shared faces*, which intersect two or more escape regions, and the remaining faces which intersect only one escape region. If we assume that any two edges in an escape region with a common landing point bound a wake (see Definition 3.17 (3)), then it is not hard to prove the following:

A face of  $\text{Tes}_q(\mathcal{S}_p)$  with  $p > 1$  is shared if and only if it is neither a wake nor a sub-face of a wake.

As a very rough rule, the shared faces tend to have smaller orbit portraits, but larger numbers of edges.

The case  $p = 1$  is different. There is only one escape region, and every tessellation  $\text{Tes}_q(\overline{\mathcal{S}_1})$  contains a unique “exceptional” face, which contains the map  $F(z) = z^3$ , and which has trivial orbit portrait. Every other face is either a wake or a sub-face of a wake, and has non-trivial orbit portrait. This dichotomy is perhaps more visible if we invert  $\overline{\mathcal{S}_1}$ , placing the ideal point at zero and the map  $F(z) = z^3$  at infinity, as in Figure 19-right.

We can also distinguish between *shared vertices* which are boundary points of at least two escape regions, and *unshared vertices*, which are boundary points of only one escape region.

**Remark 3.33 (Not a wake).** Note that a wake must be bounded by co-periodic parameter rays. A region bounded by two rays which are not co-periodic is not called a wake.

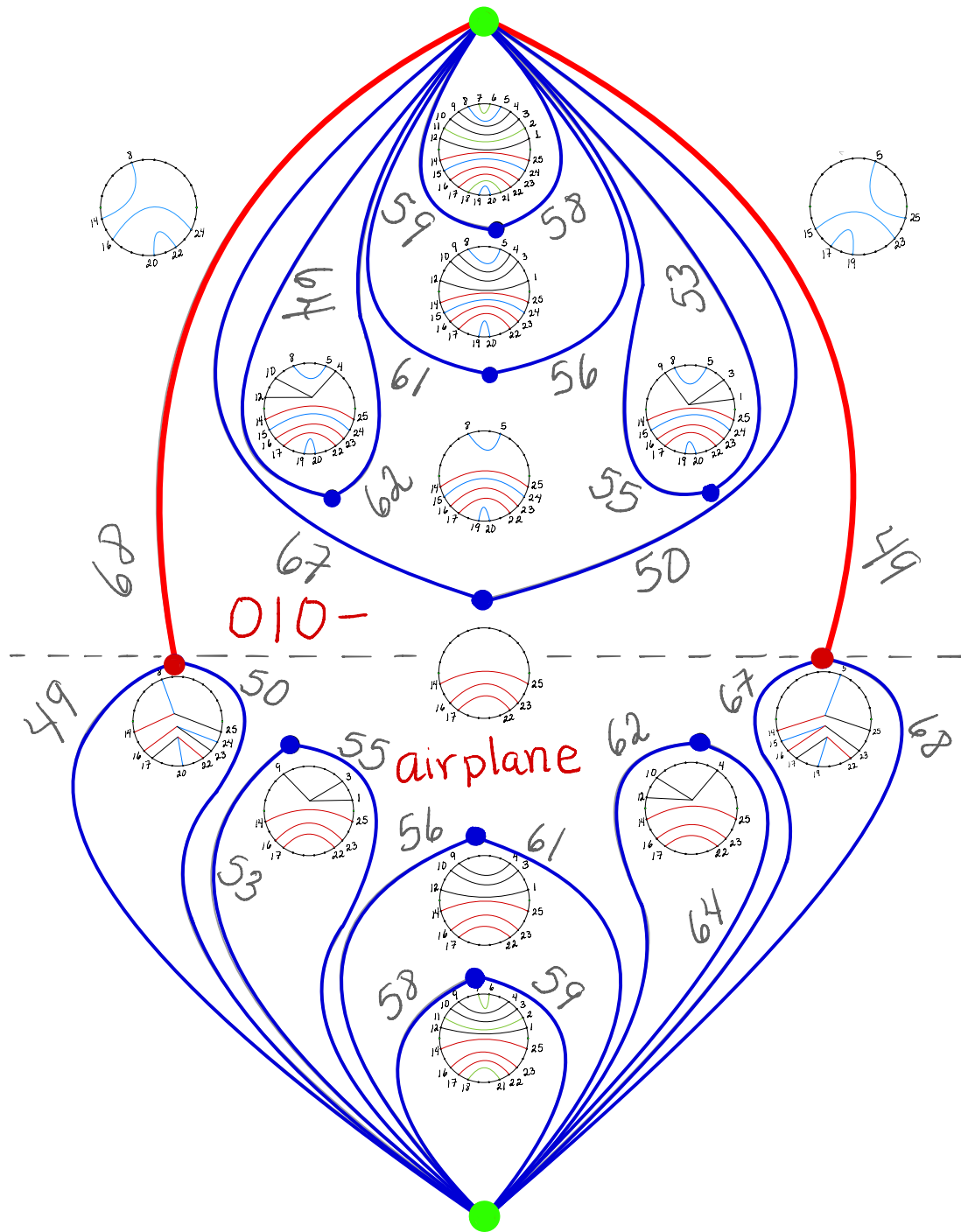


Figure 30: Period 3 orbit portraits in a part of  $\bar{S}_3$  between the 010— escape region above, and the airplane region below. (Here 010 is an abbreviation for the kneading invariant  $(0, 1, 0)$ . Compare Figures 31 through 38.) Note the five nested wakes above, and the two nested wakes among the six wakes below. Only the central orbit portrait represents a shared face. (Denominators 26 and 78.)

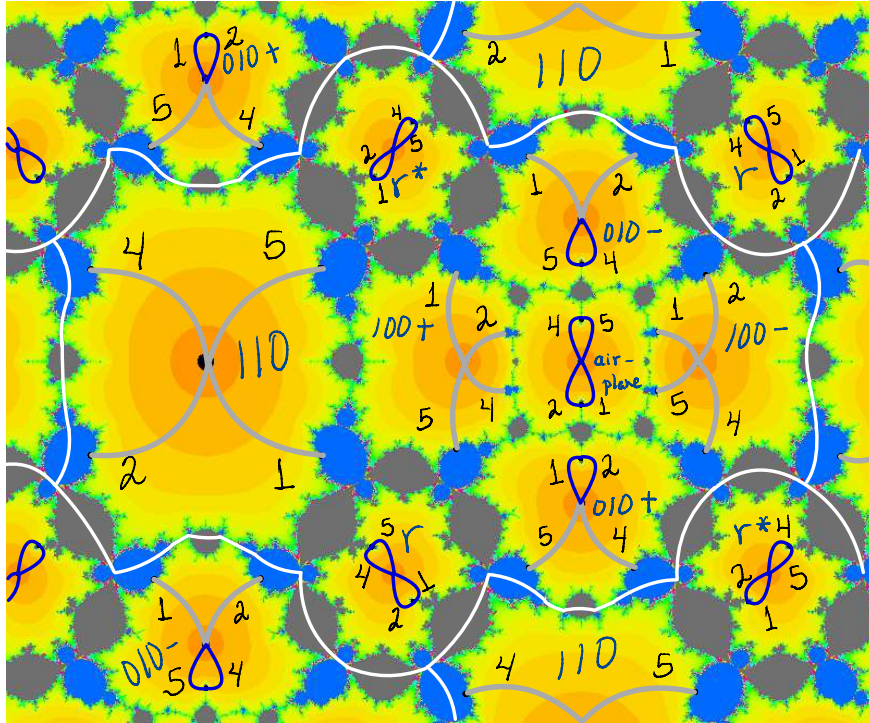


Figure 31: The tessellation  $\text{Tes}_1(\overline{S}_3)$ , lifted to the universal covering space of  $\overline{S}_3$ . (Compare [BM, Appendix].) A fundamental domain which contains one copy of each escape region is outlined in white, with 110, 100+, the airplane, and 100– in the central row, with the co-rabbit and 010– above, and with the rabbit and 010+ below. (Note that this white curve cuts across faces of the tessellation.) The orbit portrait is non-trivial for maps in each of the eight simply-connected wakes, but is trivial within the large non simply-connected shared face.

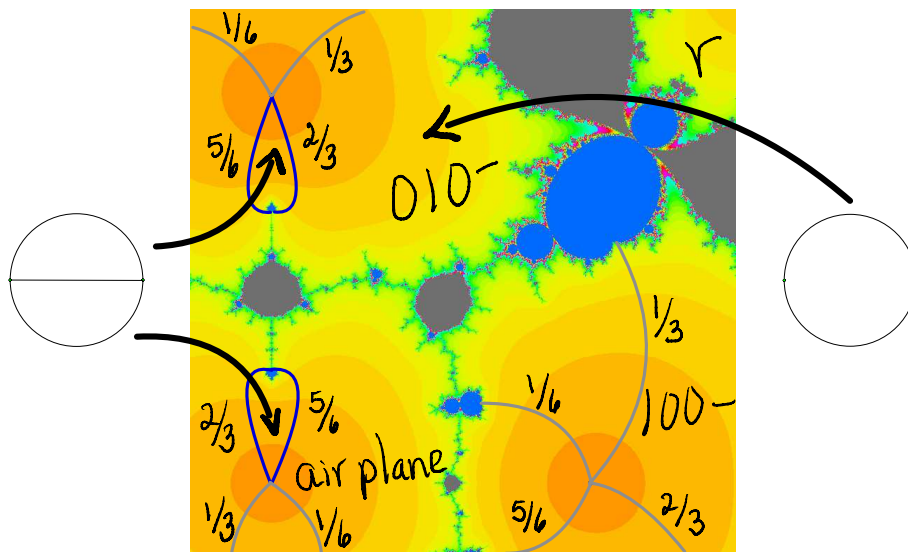


Figure 32: Magnified picture of a region in the upper right of Figure 31, showing the associated orbit portraits.

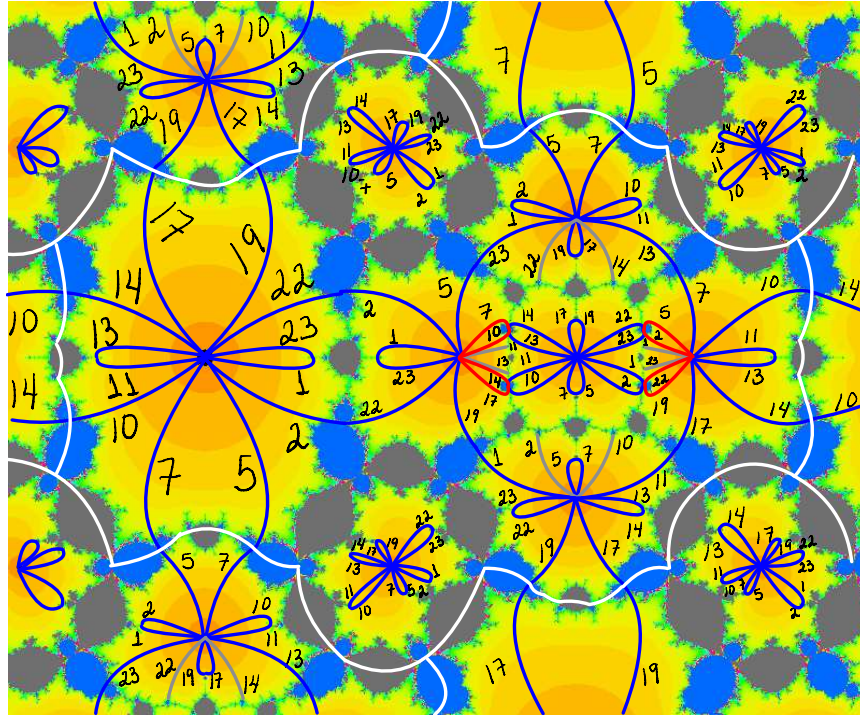


Figure 33: The tessellation  $\text{Tes}_2(\overline{S}_3)$  contains 32 wakes, together with 8 simply-connected shared faces, and two shared faces surrounding the two rabbit regions which are not simply-connected. As usual, primary edges are blue and secondary edges are red.

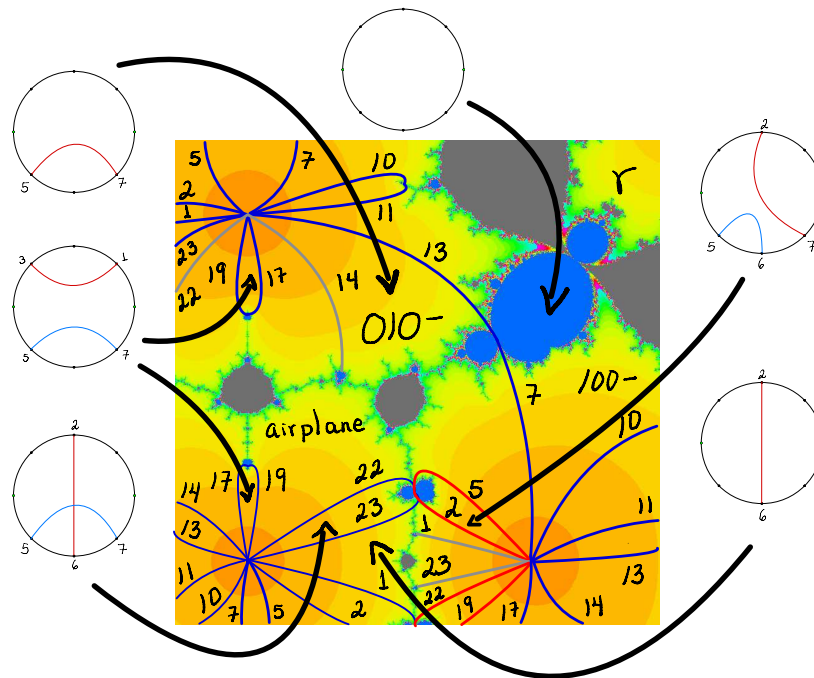


Figure 34: Again a magnified picture of a region to the upper right, showing the associated orbit portraits. Each of these non-trivial orbit portraits is found also in  $\text{Tes}_2(\overline{S}_2)$ , Figure 18.

As an example, the  $4/18$  and  $5/18$  rays in  $\mathcal{S}_1$  (the dotted white curves in Figure 20) land at a Misiurewicz map which is the bottom boundary point of an oval shaped hyperbolic component of Type C. Since these rays and their landing point are all contained in the interior of a single face of  $\mathbf{Tes}_3(\overline{\mathcal{S}}_1)$ , the period 3 orbit portrait does not change as we cross these rays. In fact a similar argument shows that the period  $q$  orbit portrait does not change for any  $q$ . The Julia set for this landing point is shown in Figure 29.

The rest of this section will discuss many detailed pictures of tessellations; while the theoretical discussion will resume in Section 4.

**Remark 3.34 (The torus  $\overline{\mathcal{S}}_3$ ).** Before describing tessellations of  $\overline{\mathcal{S}}_3$ , it may be useful to describe this space briefly. (See Figures 30 through 38, and see [BM, Appendix D] for details.) There are eight escape regions. Three of these belong to the zero kneading family of Remark 2.21, and correspond to the rabbit, co-rabbit, and airplane. There is also one escape region with kneading invariant  $110$ , and two each with kneading invariants  $100$  and  $010$ . The three involutions of Remark 3.6 interchange these eight escape regions as follows. The airplane and  $110$  regions map to themselves under all three involutions, and hence have a full group of symmetries. Each of the remaining six is invariant under only one of the three involutions. Thus the  $180^\circ$  rotation maps each rabbit region to itself but interchanges the remaining four in pairs, with

$$010 - \longleftrightarrow 010+ \quad \text{and} \quad 100 - \longleftrightarrow 100+ .$$

Similarly, complex conjugation maps each  $010\pm$  region to itself, but interchanges the two rabbits and the two  $100\pm$  regions; while left-right reflection interchanges the rabbits and the  $010\pm$  regions.

**The tessellation  $\mathbf{Tes}_1(\overline{\mathcal{S}}_3)$ .** In Figure 31 we show the period 1 tessellation of the full torus; while Figure 32 concentrates on an smaller region in the upper right of the airplane region. In most of Figure 32, the period one orbit portrait is trivial; but inside the three wakes to the left, the portrait is  $\{\{0, 1/2\}\}$ . The boundary rays of these wakes are primary rays (Definition 3.24); but the other rays shown are all non-separating.

This tessellation is similar to the period one tessellations of  $\overline{\mathcal{S}}_1$  and  $\overline{\mathcal{S}}_2$  in the following sense: For each of these cases, there is a one-to-one correspondence between escape regions and connected components of the 1-skeleton, with each such component contained in the closure of a corresponding escape region.<sup>9</sup> For any  $\mathbf{Tes}_1(\overline{\mathcal{S}}_p)$  where this is true, it follows easily that the face  $\mathcal{F}_0$  which separates the various components of the 1-skeleton satisfies

$$H_1(\mathcal{F}_0) \xrightarrow{\simeq} H_1(\mathcal{S}_p) \xrightarrow{\text{ont}^0} H_1(\overline{\mathcal{S}}_p) .$$

For example, if  $p = 3$ ,  $H_1(\mathcal{F}_0)$  is isomorphic to the group  $H_1$  of an 8-fold punctured torus, which has rank 9. (The first puncture does not change the rank; but each additional puncture adds one.)

---

<sup>9</sup>It seems possible that the analogous statement is true for every  $\mathbf{Tes}_1(\overline{\mathcal{S}}_p)$ . However, it would fail if there were a Mandelbrot copy with cusp point of period one which lies along the boundary between two escape regions (as in Figure 40 for the period five case). If this happens, then the two regions would be connected within  $\mathbf{Tes}_1(\overline{\mathcal{S}}_p)$ .

If the escape region has multiplicity one (as it always does when  $p \leq 3$ ), note that a component of the 1-skeleton of  $\mathbf{Tes}_1$  which is contained in its closure can only have the shape of an  $X$ , an  $\alpha$ , or of a figure eight.

**The tessellation  $\mathbf{Tes}_2(\overline{\mathcal{S}}_3)$ .** In Figure 33 we show the 2 tessellation of the full torus; while in Figure 34 we concentrate on a smaller region in the upper right of the airplane region. In this figure, the two thin wakes on the left with co-periodic angles  $17/24$  and  $19/24$  are primary, and lie inside the corresponding period one wakes  $4/6$  and  $5/6$  shown in Figure 32. The fatter wake in the airplane region with angles  $22/24$  and  $23/24$ , is also primary: Its orbit portrait is the amalgamation of the orbit portraits of the two neighboring faces (Definition 3.11). However, the nearby wake in the  $100-$  region is secondary. Note that the face with trivial orbit portrait is not simply connected, and completely surrounds the rabbit region.

Consider the large Mandelbrot copy in  $\mathcal{S}_3$  which lies between the  $010-$ ,  $100+$ , and rabbit regions, as shown in these figures. The cusp point of this copy is near the bottom right of the copy, and is the landing point of a non-separating ray in the period one tessellation. (See Figures 31 or 32.) The  $1/2$  limb of this copy is to the lower left, and its root point is the landing point of two rays in the period two tessellation which are primary; but do not bound any wake. (See Figures 33 or 34.)

This tessellation has two faces which are not simply-connected. In fact there is one such face surrounding each of the two rabbit regions, and each of these has the topology of an annulus.

Here the common denominator for the edge angles is  $3d(2) = 24$  (as is true for any  $\mathbf{Tes}_2(\overline{\mathcal{S}}_p)$ ).

**The tessellation  $\mathbf{Tes}_3(\overline{\mathcal{S}}_3)$**  (Figures 35, and 36 through 38). This is the most complex tessellation we have tried to understand in detail. Figure 35 shows a simplified picture of  $\mathbf{Tes}_3(\overline{\mathcal{S}}_3)$ , where an edge of the tessellation is shown only if its parabolic endpoint belongs to the boundaries of two (or three) different escape regions. This figure is enough to show that every face of  $\mathbf{Tes}_3(\overline{\mathcal{S}}_3)$  is simply-connected; but of course does not give a complete picture of the tessellation.

Figure 36 shows the orbit portraits in the area between the airplane and the rabbit region. The  $1/3$ -limb of the big Mandelbrot copy lying between the  $010-$  and  $100-$  regions lies in the rabbit region, and its root point is the landing point of four rays in the period three tessellation. The two rays in the rabbit region are primary and bound a primary wake, while the other two are secondary and do not bound any wake.

Figure 37 provides a complete picture for a large open subset of  $\mathbf{Tes}_3(\overline{\mathcal{S}}_3)$  centered around the “airplane” escape region. There are 36 faces of the tessellation which intersect the airplane region; but up to symmetry, as described in Remark 3.3, only eleven of these are distinct. In fact it suffices to study the eleven which lie in the upper right hand quadrant of the figure.

Figure 38 shows the orbit portrait for each of these eleven faces. Four of these are shared faces (two shared with the  $100-$  region, one with the  $010-$  region, and one shared with both). The remaining seven consist of six wakes and one sub-face of a wake. The shared

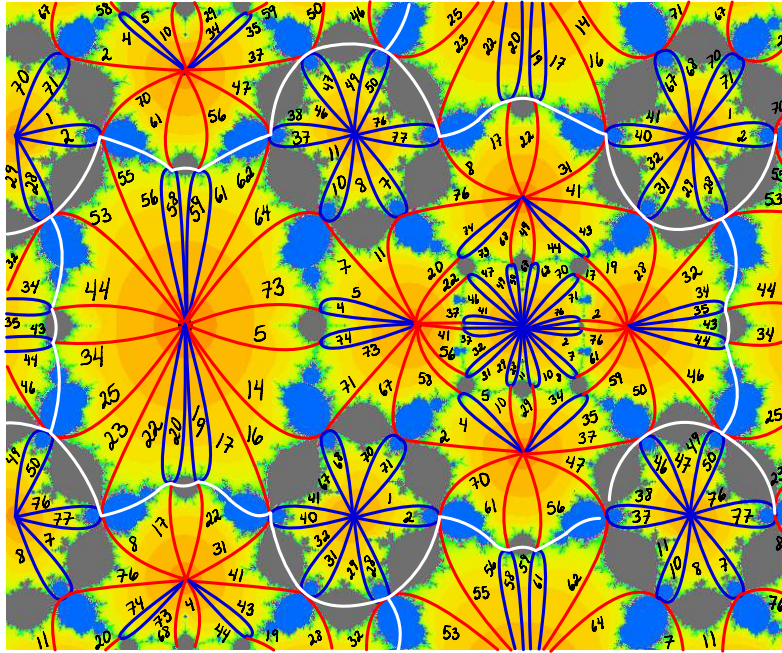


Figure 35: Simplified picture of  $\text{Tes}_3(\overline{\mathcal{S}}_3)$ . Only the rays which land on a common boundary point between two or more escape regions are shown. Here the common denominator for parameter angles is 78.

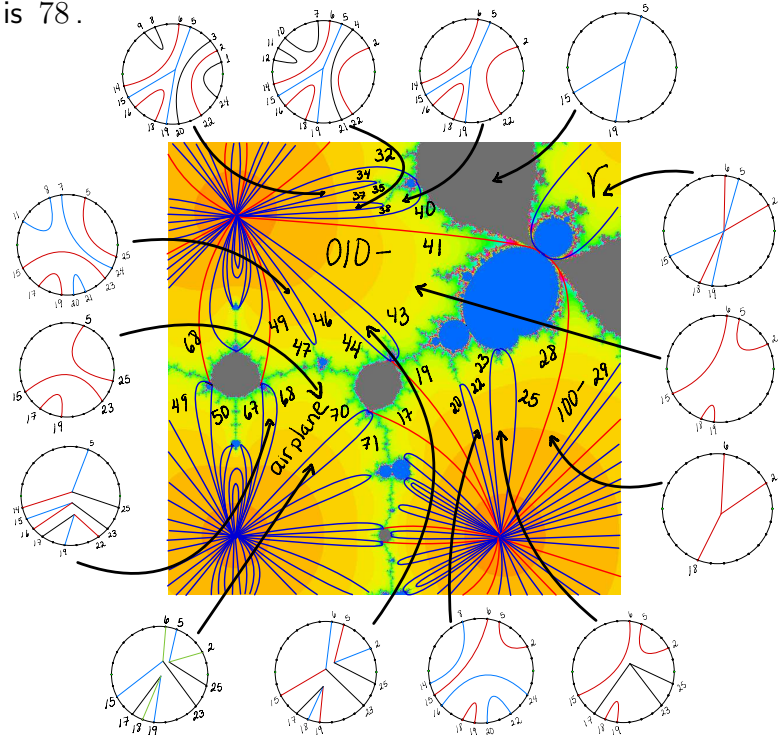


Figure 36: Period three tessellation and orbit portraits for an area to the upper right. The wake in the rabbit region, and the wake which lies between the 43 and 44 rays in 010– provide examples for which the orbit portrait is the amalgamation of the orbit portraits for the two neighboring shared faces. (See Proposition 4.8.)

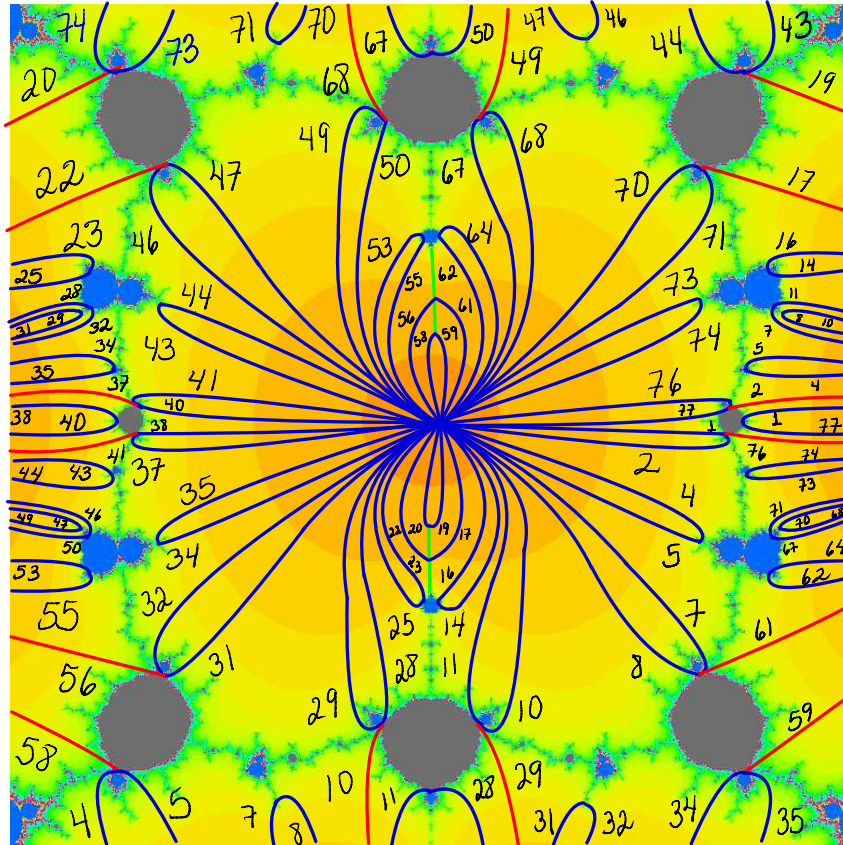


Figure 37: Detail of the airplane region of  $\text{Tes}_3(\bar{\mathcal{S}}_3)$  showing all of the co-period three rays.

faces all have orbit portraits of size three, although each shared face has an edge in common with each of its neighboring shared faces.<sup>10</sup> The remaining faces (wakes and sub-faces of wakes) have portraits of size either six or nine. The number of edges of these faces vary from two for the wakes and four for the sub-face of a wake to six, eight, or twelve for the shared faces. (For shared faces, we must also count edges outside of the of the airplane region, which are visible only in Figure 37.)

However further details definitely depend on the choice of escape region. For example, corresponding faces in different escape regions often have different orbit portraits. This is because the surroundings often impose different background relations. (Compare Section 4.)

## 4 Around a Parabolic Point

This section will help to describe  $\text{Tes}_q(\mathcal{S}_p)$  by giving a precise description of the changes in the period  $q$  orbit portrait as we circle around a parabolic vertex of the tessellation. Much of the discussion will assume that the Edge Monotonicity Conjecture 3.27 is satisfied.

<sup>10</sup>It is curious that the twelve shared faces around the airplane, together with their common edges, form an annulus surrounding the ideal point.

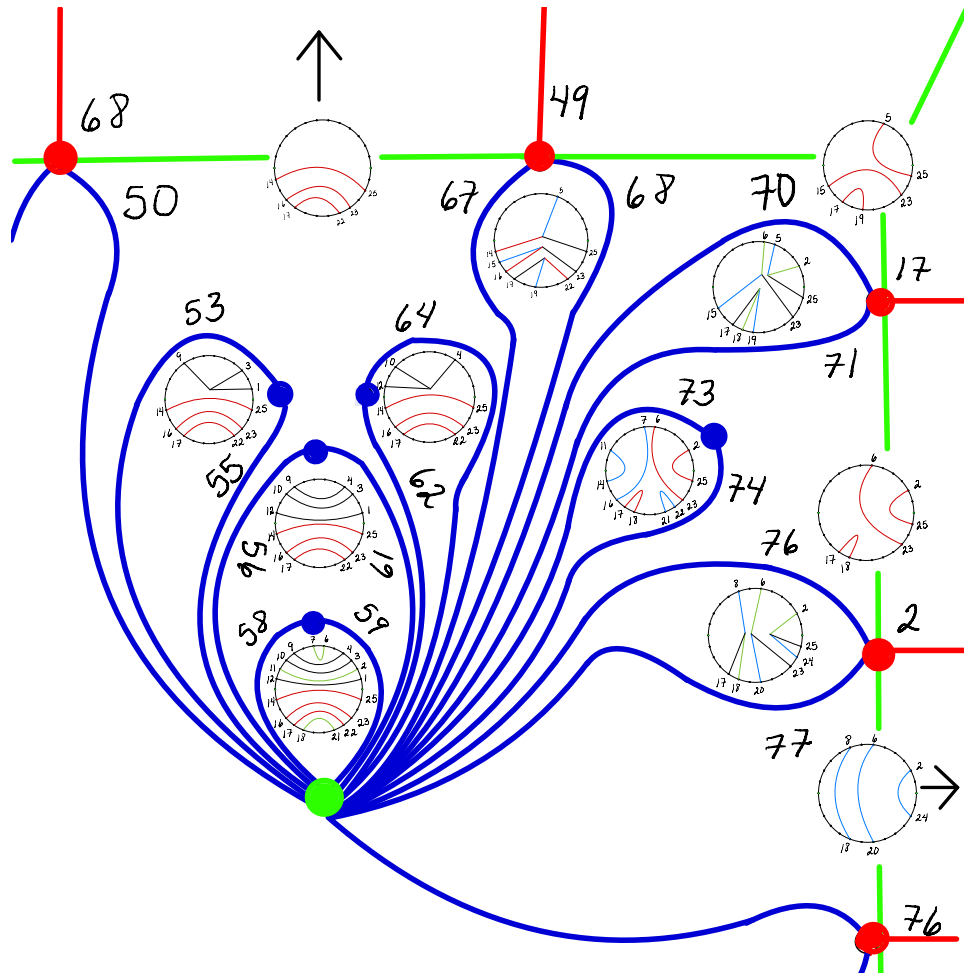


Figure 38: These orbit portraits correspond to faces in the top right quadrant of the airplane region of  $\text{Tes}_3(\overline{S}_3)$ , with the 010– region above and the 100– region to the right. Compare Figures 30, 37 and 36. Note that the three portraits on a vertical line through the ideal point are invariant under left-right reflection. Corresponding portraits for the upper left quadrant could be obtained by left-right reflection around this vertical line. Similarly the portrait on a horizontal line through the ideal point is invariant under up-down reflection (= complex conjugation); and portraits for the two lower quadrants could be obtained by up-down reflection in this horizontal line. Three of the wakes in each quadrant border on two different shared faces, and have orbit portrait equal to the amalgamation of the portraits for these two faces. (See Definition 3.11.)

First a definition. If an orbit relation  $\phi \simeq \psi$  is true for all maps in a neighborhood of  $\mathbf{p}$ , then it will be called a **background orbit relation** around  $\mathbf{p}$ . It is essential to specify the point  $\mathbf{p}$  since different parabolic points will often have different background relations. As examples, in Figure 38 the five points where exactly two rays meet all have background relations, while the five points where three rays meet do not.

Here we are concerned only with orbits relations of period  $q$ . For  $q' \neq q$  the point  $\mathbf{p}$  will be an interior point of some face of the  $q'$  tessellation, and the period  $q'$  orbit portrait will be constant throughout this face. If the point  $\mathbf{p}$  is contained in a wake  $W$ , then every

relation which holds for all points of  $W$  is certainly a background relation around  $\mathbf{p}$ .

This section will often ignore background relations and concentrate on the *distinguishing relations* which hold for some maps near  $\mathbf{p}$  but not for all.

**Notation:** It will be convenient to use Greek letters, such as  $\theta$ , for parameter angles of co-period  $q$ , and to use the notation  $\{\theta_j\}$  for the associated cycle of periodic dynamic angles, where  $j$  is an integer modulo  $q$ , and where  $\theta_j = 3^k\theta$  for any integer  $k \geq 1$  which represents  $j \bmod q$ . Thus if

$$\theta = \frac{n}{3(3^q - 1)} \quad \text{then} \quad \theta_1 = \frac{n}{3^q - 1} .$$

However we must be careful with this notation since the correspondence  $\theta \mapsto \theta_j$  is two-to-one. Here is a more precise statement.

**Lemma 4.1.** *For every periodic critical value angle  $\theta_1 = n/(3^q - 1)$  there are two possible choices for the associated co-periodic angle  $\theta = n'/3(3^q - 1)$ . The numerator  $n'$  must satisfy*

$$n' \equiv n \pmod{3^q - 1}, \quad \text{and} \quad n' \equiv \pm 1 \pmod{3} .$$

Thus the two possible choices of  $\theta$  correspond to the two possible choices of sign  $\pm 1$ . The proof is easily supplied: The first congruence must be satisfied so that  $3\theta = \theta_1$ , and the second must be satisfied so that  $\theta$  is co-periodic rather than periodic. (Recall that the two choices are referred to as **twin** co-periodic angles. Of course both choices belong to the same grand orbit.)  $\square$

A completely equivalent statement would be that

$$\theta = \theta_q \mp 1/3 = 3^{q-1}\theta_1 \mp 1/3, \tag{7}$$

where  $\mp$  is the opposite of the sign  $\pm$  above. (Compare Figure 1.) Here  $3^{q-1}\theta_1 = \theta_q$  is the angle of the dynamic ray landing at the free critical point, since  $F^{\circ q-1}$  maps the free critical value  $v'$  to the free critical point  $-a$ . If we multiply Equation (7) (which can be thought of as a congruence modulo one) by  $3(3^q - 1)$  then we obtain the congruence

$$n' \equiv 3^q n \mp (3^q - 1) \pmod{3(3^q - 1)} .$$

This last congruence must hold both modulo three and modulo  $3^q - 1$ , yielding the two congruences of the lemma.

**Face Notation.** If there are  $n$  parameter rays landing at the parabolic point  $\mathbf{p}$ , then the  $n$  corresponding faces around  $\mathbf{p}$  will be numbered in counter-clockwise order as  $\mathcal{F}_k = \mathcal{F}_k(\mathbf{p})$  where  $1 \leq k \leq n$ . Here the **number one face**  $\mathcal{F}_1$  will always be the one which contain the unique component  $H_{\mathbf{p}}$  of type D which has  $\mathbf{p}$  as its root point.

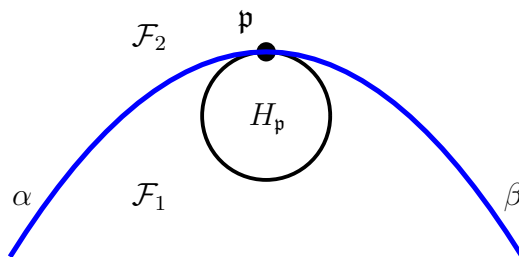


Figure 39: Cartoon for the Two Ray Case

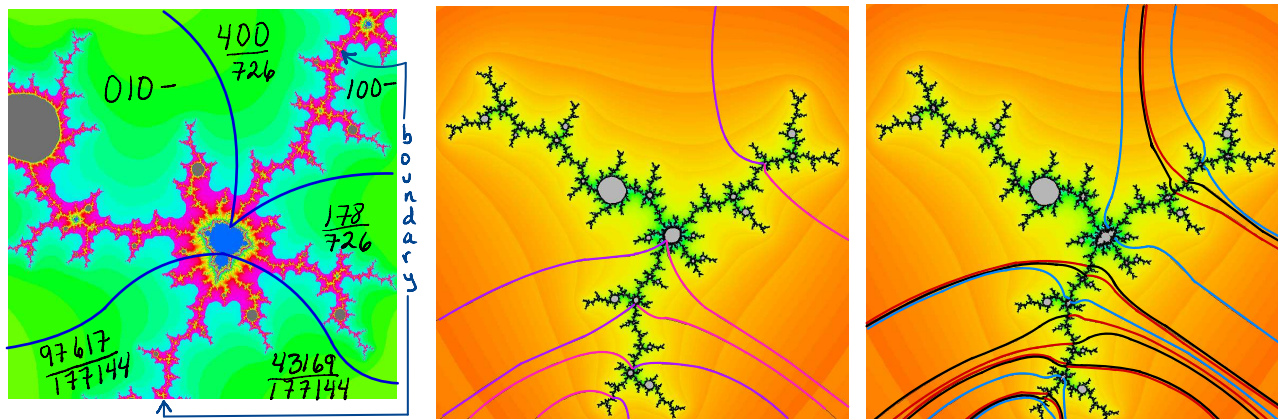


Figure 40: Illustrating the two ray case. **On the left:** magnified picture of a Mandelbrot copy of Type  $M(5,3)$  which lies **along** the boundary between the  $010-$  region on the left and  $100-$  region on the right, as in Figure 11. There are many pairs of primary rays, one from the left and one from the right, which land together at points of  $M$ . We have drawn the pair of co-period five landing at the cusp point, and the pair of co-period ten landing in the middle. (The others all have higher co-period.) **Middle:** Julia set picture showing the period five orbit portrait for a map below the cusp point. (The corresponding portrait for points above the co-period five rays is trivial.) **Right:** The period ten orbit portrait has size ten above the co-period ten parameter rays and size fifteen below. This figure illustrates the larger orbit portrait. The rays in the size ten part, which is unchanged in the crossing, are colored red and black. Thus the landing orbit has period ten, and also ray period ten. The dynamic rays in the part which appears only below the co-period ten are colored blue. They land on an orbit which has period five, but ray period ten. (The most conspicuous smaller Mandelbrot copies in the left hand figure are of Type  $M(8,3)$  on the left, and  $M(7,3)$  upper right. The black disks, including the large one on the left, are capture components. This figure is located in the short stretch of common boundary between the  $010-$  and  $100-$  regions in Figures 32 through 36.)

## The Two Ray Case

If only two parameter rays land at  $p$ , the discussion is fairly easy. We will label these two rays by their angles as in Figure 39. Since the  $\alpha$  and  $\beta$  parameter rays land together at  $p$ , it follows as in Theorem 3.26 that the  $\alpha_j$  and  $\beta_j$  dynamic rays land together for all  $F \in H_p$

and hence for all  $F$  in the face  $\mathcal{F}_1$ . Thus we have the orbit portrait relations

$$\alpha_j \simeq \beta_j \quad \text{for every } j \in \mathbb{Z}/q \quad (8)$$

throughout  $\mathcal{F}_1$ . On the other hand, since the  $\alpha$  and  $\beta$  edges are primary, the relations (8) disappear when we cross to the face  $\mathcal{F}_2$ . In all the cases we have observed, the relations (8) are the only distinguishing relations. (In principle there could be others. If there is a background relation  $\phi \simeq \psi$ , and if the landing point of  $\alpha_j$  jumped to the landing point of  $\phi$ , then two new distinguishing relations  $\alpha_j \simeq \phi$  and  $\beta_j \simeq \psi$  would be generated. But this does not happen in any case we have seen.)

**Caution.** This numbering of faces is only a local description with respect to  $\mathfrak{p}$ . As an example, in Figure 38 the face surrounded by rays 56, 58, 59 and 61 is the number one face as seen from the parabolic point above, but the number two face as seen from the parabolic point below.

Here  $\{\alpha_j\}$  and  $\{\beta_j\}$  may be the same periodic orbit. (Equivalently, the grand orbit  $((\alpha))$  may be equal to the grand orbit  $((\beta))$ .) For an example, see the parameter rays with angle  $\alpha = 53/78$  and  $\beta = 55/78$  in Figure 38. These correspond to dynamic angles  $\alpha_1 = 1/26$  and  $\beta_1 = 3/26 = \alpha_2$ , in the same periodic orbit. It follows that  $\alpha_1 \simeq \alpha_2 \simeq \alpha_3$ , so that there is an equivalence class with three elements.

On the other hand, the nearby parameter angles  $\alpha = 56/78$  and  $\beta = 61/78$  correspond to angles  $\alpha_1 = 4/26$  and  $\beta_1 = 9/26$ , which are not in the same periodic orbit. In this case, each equivalence class has at most two elements.

Although in many two ray cases the  $\alpha$  and  $\beta$  rays form the boundary of a wake, this is not always the case. See Figure 40 for a configuration where these two parameter rays lie in different escape regions.

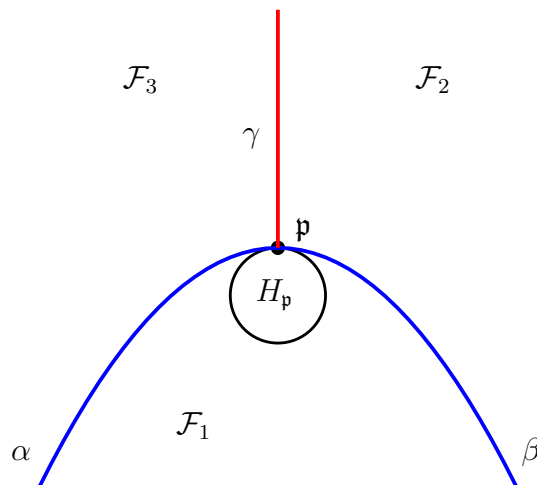


Figure 41: Cartoon of the three faces surrounding a parabolic point where three rays land.

## The Three Ray Case.

If there are three parameter rays of co-period  $q$  landing at a point  $\mathfrak{p} \in \mathcal{S}_p$ , labeled as in Figure 41, then the period  $q$  orbit relations in  $\mathcal{F}_1$  are clearly generated by

$$\alpha_j \simeq \beta_j \simeq \gamma_j \quad \text{for all } j \in \mathbb{Z}/q, \quad (9)$$

(together with any background relations which may exist). However, in all of the three ray cases we have seen:

- (a) There are no period  $q$  background relations at  $\mathfrak{p}$ ;
- (b) the grand orbits of  $\alpha$ ,  $\beta$  and  $\gamma$  are distinct:

$$((\alpha)) \neq ((\beta)) \neq ((\gamma)) \neq ((\alpha)); \text{ and} \quad (10)$$

- (c)  $\mathfrak{p}$  is the root point of a Mandelbrot copy of period  $q$  which is enclosed between the two primary rays with angle  $\alpha$  and  $\beta$ .

**Lemma 4.2.** *It follows from (a) and (b) that the period  $q$  orbit portrait for the face  $\mathcal{F}_1$  consists of  $q$  disjoint triples  $\alpha_i \simeq \beta_i \simeq \gamma_i$ . Similarly the orbit portrait for  $\mathcal{F}_2$  consists of  $q$  disjoint pairs  $\alpha_i \simeq \gamma_i$ , while the orbit portrait for  $\mathcal{F}_3$  consists of  $q$  disjoint pairs  $\beta_i \simeq \gamma_i$ .*

*Proof.* As base point in  $\mathcal{F}_1$  we can take the center point of the component  $H_{\mathfrak{p}}$ . Then the free critical point will be periodic of period  $q$ . The dynamic rays  $\alpha_i, \beta_i$ , and  $\gamma_i$  will land on  $F^{\circ i}(-a)$  for  $1 \leq i \leq q$ . Now as we cross the  $\beta$  ray into  $\mathcal{F}_2$ , the landing points of the  $\beta_i$  rays and only these rays must jump. But the Parabolic Stability Theorem of Appendix A implies that the new orbit relations will be a subset of the old. The only way this can happen is for all relations involving the  $\beta_i$  to disappear. The corresponding statement for  $\mathcal{F}_3$  follows similarly.  $\square$

In particular, as expected, it follows that the orbit portrait changes monotonically as we cross the two primary rays, and non-monotonically as we cross the secondary ray. Here is another important consequence.

**Corollary 4.3.** *It follows that the orbit portrait for  $\mathcal{F}_1$  is the amalgamation of the orbit portraits of the two side faces  $\mathcal{F}_2$  and  $\mathcal{F}_3$ .*

The proof is straightforward.  $\square$

**Examples.** Figure 37 provides sixteen examples of three ray points. Figure 38 shows five of these (three with a complete set of orbit portraits). The examples in this picture have the property that  $q = p = 3$ , with  $(\alpha, \beta, \gamma)$  equal respectively to

$$(67, 68, 49), \quad (70, 71, 17), \quad (76, 77, 2) \quad \text{over } 78.$$

Figure 36 contains six similar examples. Figure 43 shows the Julia set of a period three example in  $\mathcal{S}_3$ .

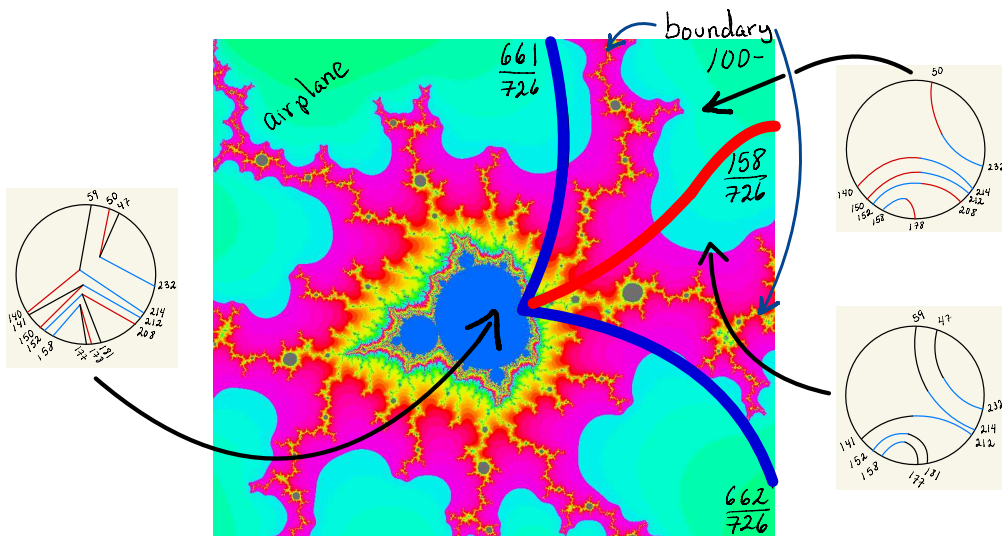


Figure 42: A three ray example. Magnified picture of a little Mandelbrot copy of period 5 which lies in a minimal primary wake in the airplane region of  $S_3$ , but with cusp point on the boundary of the 100– region. Thus the cusp is the landing point of two primary rays in the airplane region and one secondary ray in the 100– region. Note that the orbit portrait in the principal hyperbolic component is the amalgamation of the two orbit portraits on the right. This figure is located near the top of the stretch of common boundary between the airplane and 100– regions which is visible in Figures 32 through 37; very close to the ray of angle  $71/78$  which lands at the bottom root point of the type A component in the upper right of Figure 37.

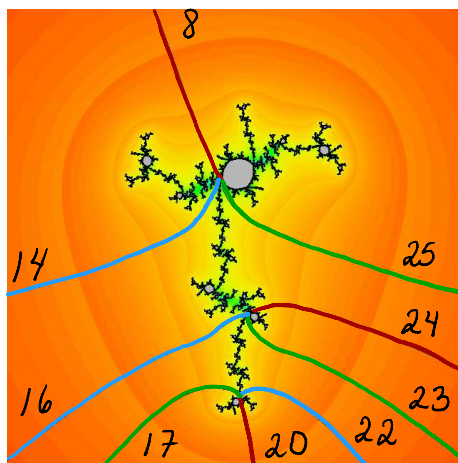


Figure 43: Julia set for the  $\mathcal{F}_0$  face of a three ray parabolic point which lies between the 110 and 010– regions of  $\text{Tes}_3(\overline{S}_3)$ , with  $\alpha = 20/78$ ,  $\beta = 22/78$  and  $\gamma = 17/78$ . This point is visible twice in Figure 35, both to the upper right and to the lower left. In this example,  $\alpha$  and  $\beta$  are contiguous as co-periodic angles, since the intermediate angle  $21/78$  is not co-periodic. Note that  $\alpha_1 = 20/26 \mapsto \alpha_2 = 8/26 \mapsto \alpha_3 = 24/26$ . Thus for example  $-a$  is at the landing point of the 24 ray while  $v' = F(-a)$  is at the landing point of the 20 ray.

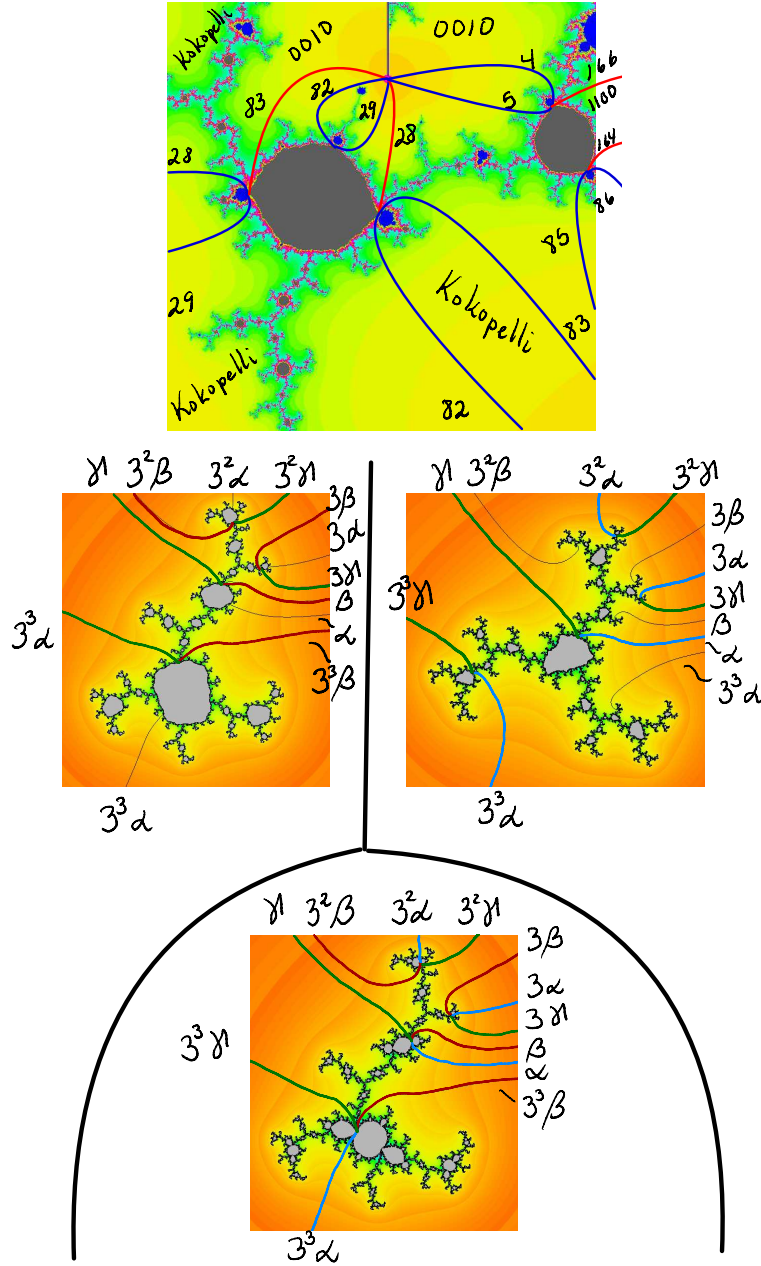


Figure 44: Above: a 3-ray point in  $\text{Tes}_4(\overline{\mathcal{S}}_4)$ . Below: Julia sets for the three faces around the parabolic vertex near the center of the top figure. Here  $(\underline{\alpha}, \underline{\beta}, \underline{\gamma}) = (82, 83, 28)/240$ , and  $(\alpha, \beta, \gamma) = (2, 3, 28)/80$ .

Figure 44 provides an example with  $p = q = 4$ , with  $(\alpha, \beta, \gamma)$  equal respectively to  $(82, 83, 28)$  over 240, and with orbit portrait of the principal hyperbolic component:

$$\{\{3, 28, 2\}, \{9, 4, 6\}, \{27, 12, 18\}, \{1, 36, 54\}\}/80 .$$

Figure 42 provides an example with  $p = 3$  and  $q = 5$  together with its orbit portraits.

**Remark 4.4.** The two primary rays always seem to belong to the same escape region; so

that the primary face which contains all of the associated Mandelbrot copy, is all or part of a wake. In many cases this wake is minimal. However in Figure 49-right there two wakes of angular width  $20/726$  attached to the bottom of the large B component; while in Figure 51-left there is one example of a wake of angular width  $19/726$  attached to the right of the large A component.

**Conjecture.** If  $p = q$  then we conjecture that  $p$  is also a root point of a component of Type A or B which lies in one of the two side faces.

Note that there can never be such an A or B component when  $p \neq q$ , since the root point of an A or B component always has period  $p$ . (Compare Figure 42.)

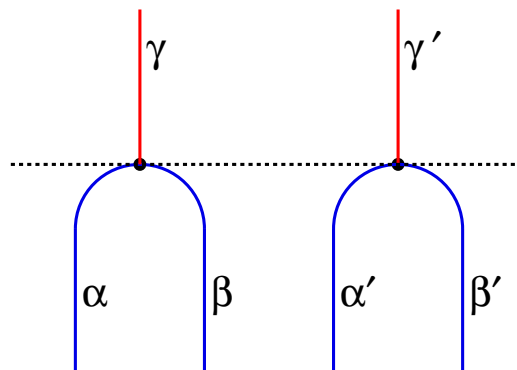


Figure 45: Cartoon illustrating an adjacent pair of 3-ray triples, satisfying condition (1).

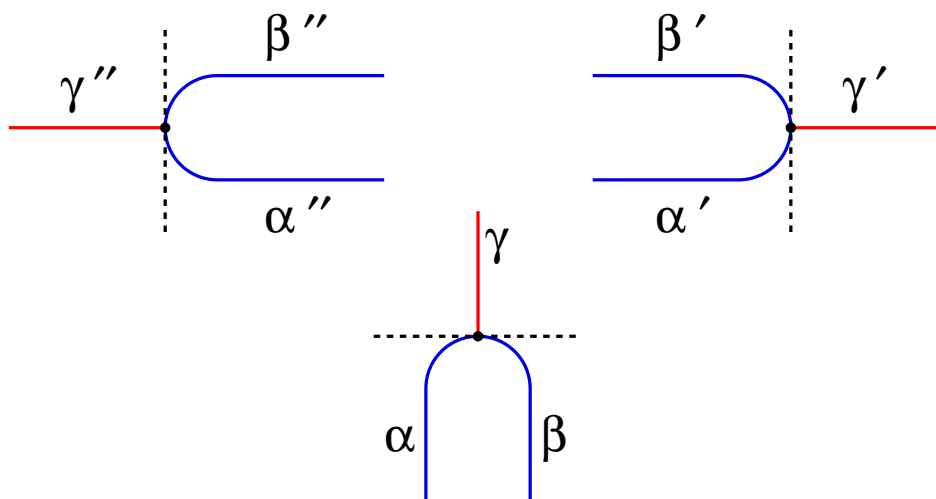


Figure 46: Cartoon illustrating two adjacent escape regions with 3-ray triples, satisfying condition (3).

**Neighboring 3-Ray Cases.** Now consider two adjacent 3 ray cases which are separated by a face which is shared between two escape regions, as illustrated schematically in Figures 45 and 46. If we know the three parameter angles  $\alpha$ ,  $\beta$ ,  $\gamma$ , then we can compute the orbit portraits of the three faces around the left hand triple. Similarly if we know  $\alpha'$ ,  $\beta'$ ,  $\gamma'$ , then we can compute the orbit portraits of the three faces around the right hand triple. This means that the orbit portrait for the central face, with its dynamics, can be computed in two different ways. From the left it is generated by the paired orbits

$$(\alpha_1, \gamma_1) \mapsto (\alpha_2, \gamma_2) \mapsto \cdots \mapsto (\alpha_p, \gamma_p) .$$

But from the right it is generated by the paired orbits

$$(\gamma'_1, \beta'_1) \mapsto (\gamma'_2, \beta'_2) \mapsto \cdots \mapsto (\gamma'_p, \beta'_p) .$$

Thus the unordered pair  $\{\alpha_1, \gamma_1\}$  must be equal to  $\{\gamma'_j, \beta'_j\}$  for some  $j$ .

**Notation.** It will be convenient to use the notation  $((\alpha))$  for the grand orbit of an angle  $\alpha$  of co-period  $q$ , recalling that each such grand orbit contains a unique period  $q$  orbit  $\langle \alpha_1, \alpha_2, \dots, \alpha_q \rangle$ , where  $\alpha \mapsto \alpha_1 \mapsto \cdots \mapsto \alpha_q$  under tripling.

**Remark 4.5.** We believe that all four grand orbits can never be identical. Assuming this, it follows that either:

$$\text{Condition (1): } ((\alpha)) = ((\gamma')) \neq ((\gamma)) = ((\beta')), \quad \text{or}$$

$$\text{Condition (2): } ((\gamma)) = ((\gamma')) \neq ((\alpha)) = ((\beta')), \quad \text{or}$$

$$\text{Condition (3): } ((\gamma)) = ((\gamma')) \neq \text{ and } ((\alpha)) = ((\alpha')) \text{ or } ((\beta)) = ((\beta')) .$$

In fact it seems that Condition (1) always applies in cases where the diagram is strictly like Figure 45, meaning when the two primary wakes are in the same escape region. However we will see that with versions of the diagram which are only slightly modified, the case of Condition (2) can also occur. (Figures 37 and 51-left illustrate conditions (1) and (2)). Condition (3) is satisfied in the case of Figure 46. (Figure 49 illustrates Condition (3).)

Note that Condition (1), exemplified in Figure 45, concerns only the four outer angles  $\gamma$ ,  $\alpha$ ,  $\gamma'$  and  $\beta'$ . Condition (3), exemplified in Figure 46, concerns the angles  $\gamma$ ,  $\gamma'$ ,  $\alpha$  and  $\alpha'$  on the right; and  $\gamma$ ,  $\gamma''$ ,  $\beta$  and  $\beta''$  on the left.

There are three possible cases which correspond precisely to the diagram in Figure 45: Either there is a unique component of Type A or B occupying the middle of the central face, or there is no component of Type A or B in this face. Condition (3) corresponds to the case in which there is no component of Type A or B in the face.

**The A-Centered Case.** In this case the central face is centered at an A component, with three rays landing at each root point. (Compare Figure 47.) Since each root point of a Type A component in  $\mathcal{S}_p$  has period  $p$ , we must have  $q = p$ . We conjecture that the three grand orbits  $((\alpha))$ ,  $((\beta))$ ,  $((\gamma))$  are always distinct, and that the cyclic order of  $\alpha$ ,  $\beta$ ,  $\gamma$  is always the same as the cyclic order of their twins.



As an example in  $\mathcal{S}_4$ , in the top right of Figure 44 with denominator  $3d(4) = 240$ , the twins of 4, 5, and 166 are  $\widehat{4} = 164$ ,  $\widehat{5} = 85$  and  $\widehat{166} = 86$ .

An example in  $\mathcal{S}_5$  is given by the large A component in Figure 51. In this case we have

$$\alpha = 64 \mapsto \langle 192, 92, 34, 102, 64 \rangle, \quad \beta = 65 \mapsto \langle 195, 101, 61, 183, 65 \rangle, \quad \gamma = 568 \mapsto \langle 10, 30, 90, 28, 84 \rangle,$$

with twin angles  $\widehat{\alpha} = 548$ ,  $\widehat{\beta} = 307$ , and  $\widehat{\gamma} = 326$ . The co-periodic denominator is  $3d(5) = 726$ , while the periodic denominator is  $d(5) = 242$ .

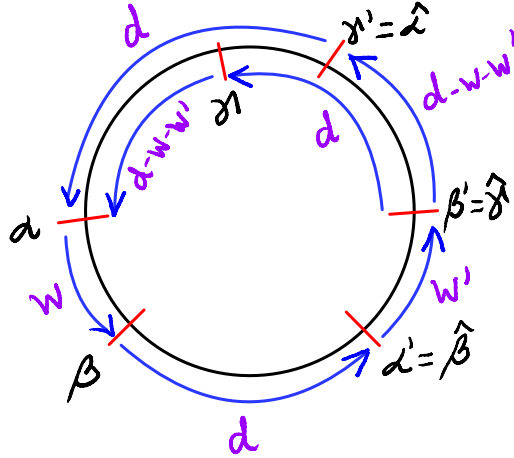


Figure 48: Cartoon illustrating angular distances around an A-centered face, following the notation of Figure 47.

**Remark 4.7.** Recall that parameter angles can be thought of as integers modulo  $3d$  where  $d = 3^q - 1$ . By the **angular distance**  $\Delta = \Delta(\theta, \eta)$ , measured in the positive direction, between two angles  $\theta$  and  $\eta$  of co-period  $q$  we will mean the unique integer  $0 \leq \Delta < 3d$  such that  $\Delta \equiv \eta - \theta$  modulo  $3d$ .

By the angular **width**  $w$  of the  $(\alpha, \beta)$ -wake we will mean the angular distance  $\Delta(\alpha, \beta)$ . In all of the examples we have seen, this width satisfies  $w \equiv 1$  modulo three, and  $w < d$ . This implies that  $\alpha \equiv 1$  and  $\beta \equiv 2$  modulo 3. Therefore

$$\widehat{\alpha} = \alpha - d \quad \text{but} \quad \widehat{\beta} = \beta + d,$$

so that  $\Delta(\widehat{\alpha}, \widehat{\beta}) = 2d + w$ . It follows easily that

$$\Delta(\beta', \gamma') = \Delta(\widehat{\gamma}, \widehat{\alpha}) = d - w - w'.$$

(Compare Figure 48.) A completely analogous argument shows that  $\Delta(\widehat{\gamma}, \gamma) = d$ , and hence that

$$\Delta(\gamma, \alpha) = d - w - w'.$$

In most of the cases we have seen,  $w = w' = 1$ ; but in the  $\mathcal{S}_5$  example described above we have  $w = 1$  and  $w' = 19$ .

**The Intermediate Case.** By this we mean the case where there is no component of Type A or B in the central face. In all such examples that we have seen, each of the two vertices is a root point of an A or B component. As an example, in the upper right of Figure 37 we have such a case lying between an A component in the airplane region of  $\mathcal{S}_3$  and a B component in the 100– region, with

$$\alpha = 70, \quad \beta = 71, \quad \gamma = 17, \quad \text{and} \quad \alpha' = 76, \quad \beta' = 77, \quad \gamma' = 2,$$

with denominator 78. For an example in  $\mathcal{S}_5$ , lying between two B components, see the left side of Figure 51-left. In this case.

$$\alpha = 28, \quad \beta = 29, \quad \gamma = 670 \quad \text{and} \quad \alpha' = 61, \quad \beta' = 62, \quad \gamma' = 574,$$

with denominator 726.

In the examples above, and conjecturally in all such examples, the four grand orbits  $((\alpha))$ ,  $((\beta))$ ,  $((\alpha'))$ ,  $((\beta'))$  are disjoint from each other, but  $((\alpha)) = ((\gamma'))$  and  $((\gamma)) = ((\beta'))$ . Thus we believe that Condition (1) is always satisfied in the Intermediate Case when the two primary wakes belong to the same escape region.

The symmetry relation  $\beta - \alpha = \beta' - \alpha'$  is satisfied in the examples above; but it is not always satisfied when the primary wakes belong to different escape regions, as exemplified in Figure 49-right. In this Figure, consider the triads determined by  $\alpha = 518/726$ ,  $\beta = 520/726$ ,  $\gamma = 515/726$ ; and  $\alpha' = 548/726$ ,  $\beta' = 568/726$ ,  $\gamma' = 521/726$ . Here  $\beta - \alpha = 2$ , and  $\beta' - \alpha' = 20$ . In the Intermediate Case, when the primary wakes belong to different escape regions, as exemplified in this Figure, Condition (3) holds.

**The B-Centered Case.** Examples with a component of type B in the middle of the central face are more complicated and interesting. These always seem to be organized in a very special way as in Figure 49-left (except that in some cases there are more than two surrounding escape regions). In the examples we have seen, the four grand orbits  $((\alpha))$ ,  $((\beta))$ ,  $((\alpha'))$  and  $((\beta'))$  are all different. Furthermore each of the four angles  $\alpha$ ,  $\beta$ ,  $\alpha'$  and  $\beta'$  is the parameter angle for two different rays which belong to different escape regions, as indicated in the figure. The angles  $\gamma$  and  $\gamma'$  of the two secondary rays always seem to satisfy  $\gamma = \beta'$  and  $\gamma' = \alpha$ .

It clearly follows that  $((\alpha)) = ((\gamma')) \neq ((\gamma)) = ((\beta'))$  in all such examples, so that Condition (1) is satisfied.

Another interesting property of the B case is that symmetry condition

$$\beta - \alpha = \beta' - \alpha' \quad \text{in} \quad \mathbb{R}/\mathbb{Z},$$

is satisfied in every case where the primary wakes belong to the same escape region. See the examples below.

**B-Centered Examples.** At the top of Figure 37 we have

$$(\alpha, \beta, \alpha', \beta') = (49, 50, 67, 68)/78,$$

with  $\mathcal{E}_1$  the airplane region in  $\mathcal{S}_3$  and  $\mathcal{E}_2$  the 010– region. In this case, both primary wakes belong to the airplane region. There is a similar example at the right center of Figure 37

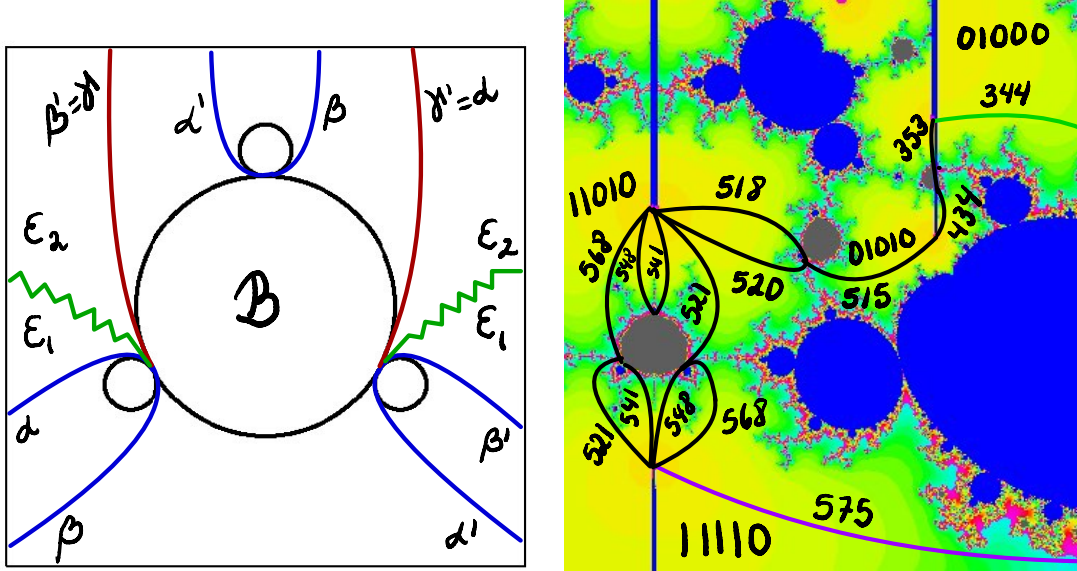


Figure 49: On the left, cartoon of a type B component between two escape regions  $\mathcal{E}_1$  and  $\mathcal{E}_2$ , showing 3 rays landing on each of its two bottom root points, plus an additional two rays landing on its top root point. Here  $\gamma = \beta'$  and  $\gamma' = \alpha$ . In all 3 ray examples that we have seen, the four grand orbits  $((\alpha))$ ,  $((\beta))$ ,  $((\alpha'))$ ,  $((\beta'))$  are all distinct. (This is true even in cases where there are more than two escape regions.) On the right, an example in  $\mathcal{S}_5$ . In this case the two wakes below the B component have angular width  $20/726$ , so they are far from minimal.

between the airplane and the 100– region. The corresponding orbit portraits are shown in Figure 38.

For a slightly different  $\mathcal{S}_3$  example, at the top of the 110 region on the left of Figure 35, the corresponding angles are  $(56, 58, 59, 61)/78$ . Thus both wakes have width two (although they are still minimal since the intermediate angles 57 and 60 are not co-periodic). As noted above, we believe that such a wake of even width can never occur in an A-centered case.

In Figure 44 (top),  $\mathcal{E}_1$  is the Kokopelli region of  $\mathcal{S}_4$  and  $\mathcal{E}_2$  is a 0010 region. The angles are  $(28, 29, 82, 83)/240$ , and both primary wakes belong to the Kokopelli region. Figure 49-right shows an example in  $\mathcal{S}_5$  where both of the wakes below the central type B component have width 20. These primary wakes belonging to the 11110 escape region are certainly not minimal.

For type B-centered examples as corners of different escape regions see Figure 51-left. This figure shows two examples in  $\mathcal{S}_5$  where the B component is surrounded by four different escape regions. The top left example with angles  $(670, 674, 28, 29)/726$  doesn't satisfy the symmetry relation, and the wake determined by 670 and 674 is certainly not minimal. Immediately below is the B component surrounded by  $(61, 62, 572, 574)/726$ . In this case again the symmetry relation is not satisfied, however the wake spanned by the angles 572 and 574 is still minimal, since the intermediate angle 573 is not co-periodic.

**Examples with A Off-Center.** We now consider cases which do not quite correspond to the requirements of Figure 45. As an example, Figure 50 can represent the face on the

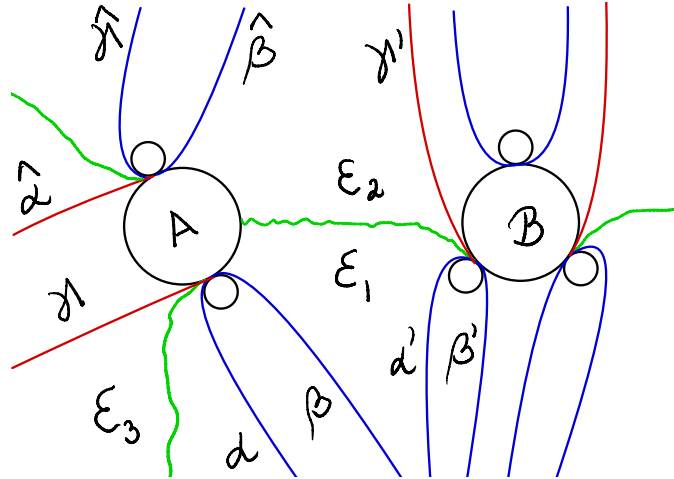


Figure 50: Cartoon showing an off-center A component, as well as the adjacent B component.

upper left of the airplane region of  $\mathcal{S}_3$ , as shown in Figure 37. In this case

$$\alpha = 46, \beta = 47, \gamma = 22, \quad \text{and} \quad \alpha' = 49, \beta' = 50, \gamma' = 68,$$

while  $\hat{\alpha} = 20, \hat{\beta} = 73, \hat{\gamma} = 74$ , all with denominator 78. Note that a mirror image case is shown on the upper right of the same figure.

On the other hand, Figure 50 can also represent the face of  $\mathcal{S}_5$  which is shown on the bottom of Figure 51-left. In this case we have

$$\alpha = 64, \beta = 65, \gamma = 568, \quad \text{and} \quad \alpha' = 91, \beta' = 92, \gamma' = 272,$$

while  $\hat{\alpha} = 548, \hat{\beta} = 307, \hat{\gamma} = 326$ , all with denominator 726.

In both cases we have  $((\alpha)) = ((\hat{\alpha})) = ((\beta'))$  and  $((\gamma)) = ((\hat{\gamma})) = ((\gamma'))$ , so that Condition (2) is satisfied. In fact we conjecture that it holds in all such cases.

**An Example with B off-center.** Figure 51-left illustrates an example in  $\mathcal{S}_5$  with

$$\alpha = 61, \beta = 62, \gamma = 574, \quad \text{and} \quad \alpha' = 64, \beta' = 65, \gamma' = 568, \quad (\text{with denominator } 726).$$

Here

$$61 \mapsto \langle 183, 65, 195, 101, 61 \rangle \quad \text{and} \quad 65 \mapsto \langle 195, 101, 61, 183, 65 \rangle$$

(with denominator 726 for parameter angles, or 242 for dynamic angles). It follows that  $((\alpha)) = ((\beta'))$ . Similarly

$$574 \mapsto \langle 28, 84, 10, 30, 90 \rangle \quad \text{while} \quad 568 \mapsto \langle 10, 30, 90, 28, 84 \rangle,$$

so that  $((\gamma)) = ((\gamma'))$ . Thus Condition (2) is satisfied.

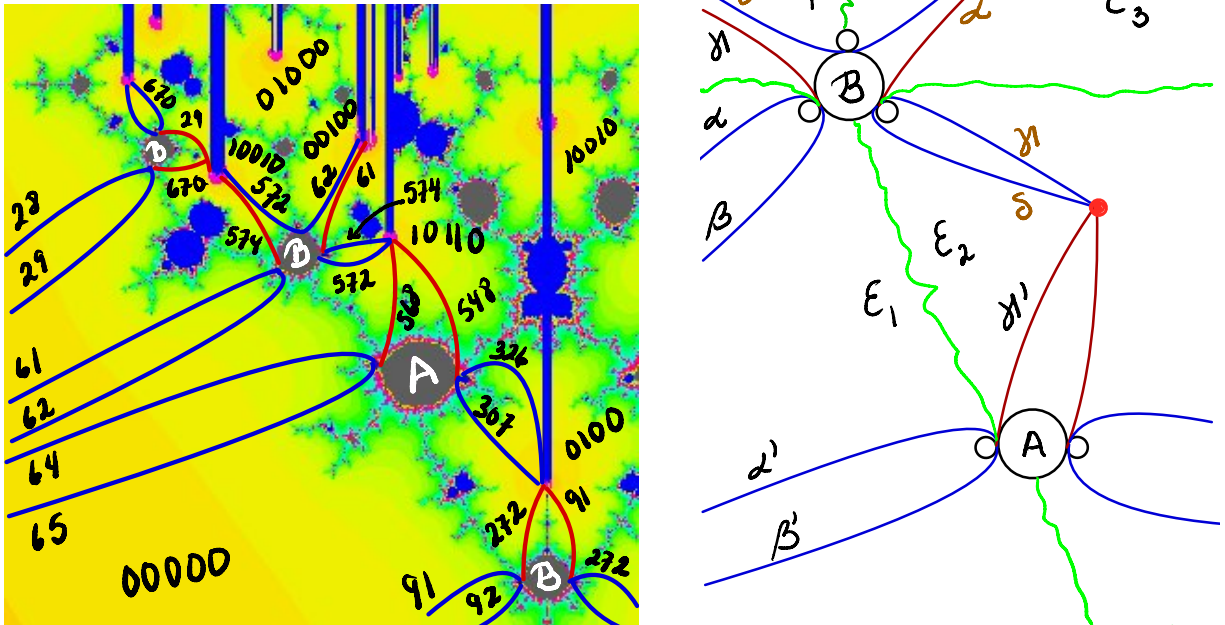


Figure 51: On the left, a region in  $S_5$ . Roughly in the middle there is a B component contained in a face which extends to the left, and which has one root point of a larger A component on its boundary. This is the only example we have seen of a B off-center face; but we suspect there are many more for larger values of  $p$ . On the right, a cartoon illustrating this face. The common denominator is  $3(3^5 - 1) = 726$ .

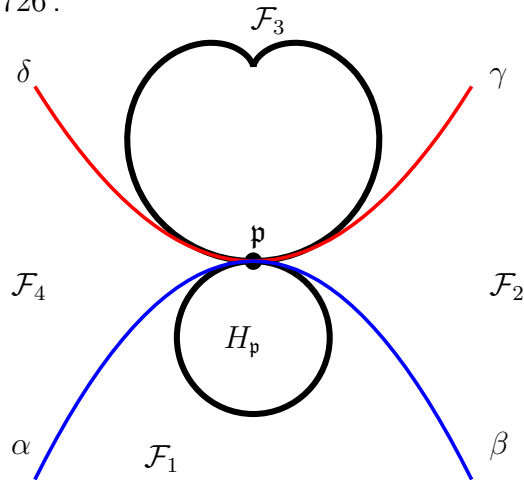


Figure 52: Cartoon of the four faces surrounding a parabolic vertex  $p$  in  $\text{Tes}_q(S_p)$  where four parameter rays land. As usual, face number one contains the component  $H_p$  which has  $p$  as root point. The opposite face is number 3 and the side faces are numbers 2 and 4. The four parameter angles, with denominator  $3(3^q - 1)$ , are denoted by  $\alpha$  through  $\delta$ .

### The Four Ray Case.

Now suppose that four edges of the tessellation  $\text{Tes}_q(\overline{S}_p)$  have  $p$  as a parabolic vertex, as illustrated in Figure 52. Arguing just as in the two and three ray cases, we see that the orbit

relations in the number one face are generated by

$$\alpha_j \simeq \beta_j \simeq \gamma_j \simeq \delta_j \quad \text{for all } j \in \mathbb{Z}/q \quad (11)$$

(together with any background relations). However in all four ray cases that we have seen:

(a') We have

$$((\alpha)) = ((\gamma)) \neq ((\beta)) = ((\delta)) . \quad (12)$$

In fact there is a somewhat more precise observation:

(b') There is a non-zero  $k \in \mathbb{Z}/q$  such that

$$\gamma_j = \alpha_{j+k} \quad \text{and} \quad \beta_j = \delta_{j+k} \quad \text{for all } j \in \mathbb{Z}/q . \quad (13)$$

In all four rays examples we have seen with  $p = q$ , there are no background relations; and  $\mathbf{p}$  is also a root point of two components of Type A or B in the two side faces. (See Figures 17 and 22.) Of course there can be no such A or B components when  $p \neq q$  (Figures 62 and 61).

Assuming (12) and (13), it follows easily that the distinguishing relations in the two side faces are generated by

$$\alpha_j \simeq \gamma_j = \alpha_{j+k} \simeq \gamma_{j+k} \quad \text{in } \mathcal{F}_2 \quad \text{and} \quad \beta_j \simeq \delta_j = \beta_{j-k} \simeq \delta_{j-k} \quad \text{in } \mathcal{F}_4 . \quad (14)$$

In fact, as we cross the  $\alpha$  edge of the tessellation, the  $\alpha_j$  and  $\gamma_j$  dynamics rays will jump so that only the  $\beta_j$  and  $\delta_j$  rays will continue to land together. Similarly, after we cross the  $\beta_j$  edge, only the  $\alpha_j$  and  $\gamma_j$  rays will land together. An important consequence is the following.

**Proposition 4.8.** *In both the three ray case and the four ray case, if we assume the appropriate grand orbit condition (10) or (12), then it follows that the orbit portrait for the number one face is the amalgamation (Definition 3.11) of the orbit portraits for the two side faces.*

Finally we must consider the opposite face  $\mathcal{F}_3$ . The Edge Monotonicity Conjecture 3.27 tells us which rays will jump as we cross the  $\gamma$  or  $\delta$  ray into  $\mathcal{F}_3$ ; however it does not tell us what they will jump to. A better strategy is to cross directly from  $\mathcal{F}_0$  to  $\mathcal{F}_3$  through the point  $\mathbf{p}$ . The conclusion as illustrated in Figure 53, is that the  $\alpha_1$  and  $\delta_1$  rays will be pushed away from the  $\beta_1$  and  $\gamma_1$  rays. This will leave only the distinguishing relations  $\alpha_1 \simeq \delta_1$  and  $\beta_1 \simeq \gamma_1$  between these particular angles, where the first two are definitely not equivalent to the second two. Since equivalence must be preserved under angle tripling, and since the equivalence relations must be a subset of those for the parabolic point, this proves the following.

**Proposition 4.9.** *The distinguishing relations for the opposite face  $\mathcal{F}_3$  are generated by*

$$\alpha_j \simeq \delta_j \quad \text{and} \quad \beta_j \simeq \gamma_j \quad \text{for all } j .$$

As we cross any secondary ray in either direction, note that all of the distinguishing relations get destroyed.

Thus we obtain quite explicit descriptions of how the period  $q$  orbit portrait changes as we circle around any parabolic vertex  $\mathbf{p}$  of the tessellation  $\mathbf{Tes}_q(\overline{\mathcal{S}}_p)$  in all of the two, three, and four ray cases, provided that the appropriate conditions (10) or (12) are satisfied. All that we need to know is the parameter angles for the rays landing at  $\mathbf{p}$ , or even the dynamic angles for the rays landing at the critical value  $F(-a_F)$ .

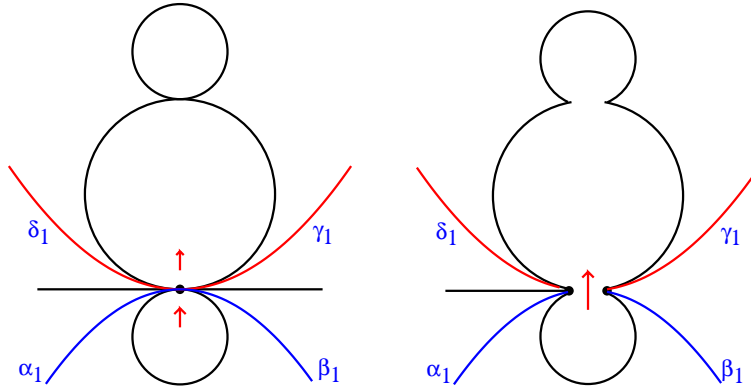


Figure 53: Cartoon illustrating the change of orbit portrait, as a parabolic point splits into a pair of repelling points. Compare Figures 62 and 61. However note that the primary wake is on top in Figure 61.

**Remark 4.10.** In all of the four ray cases we have seen, the  $\alpha$  and  $\beta$  rays belong to the same escape region, and bound a minimal wake. In fact the angles  $\alpha$  and  $\beta$  always seem to be immediately contiguous in the sense that  $\beta = \alpha + 1/3(3^q - 1)$ . (Thus if  $q$  is large the difference is VERY small.)

**Note.** If  $q$  is a prime number, then it is not hard to conclude, for maps in  $\mathcal{F}_0$ , that all of the the  $\alpha_j$  and  $\beta_j$  dynamic rays must land together at the central fixed point. This is also true in many cases where  $q$  is not prime. For example in each “rabbit” escape region of  $\mathcal{S}_p$ , as discussed in [BM, Rabbit Section] there are  $2p$  shared boundary points. Each one is the landing point of four parameter rays, and all are parabolic of ray period  $q = p$ . For the Julia sets corresponding to these boundary points, the  $2p$  primary dynamic rays all land on a central fixed point. For an example where the  $2q$  rays do not all land together, see Figure 61-right with  $q = 4$ ,  $p = 3$ .

**Remark 4.11 (Rabbit and Non-Rabbit Examples).** There is an essential difference between four ray points with  $p = q$  and those with  $p \neq q$ . The cases with  $p \neq q$  always seem to be isolated. (Compare Figures 61-left and 62-left.) There can never be an associated A or B component when  $p \neq q$  since every root point of an A or B component in  $\mathcal{S}_p$  has period  $p$ .

The case  $p = q$  is much more interesting. In every case that we have seen, the parabolic point  $\mathbf{p}$  is part of a compact connected *ring* consisting of the closures of  $2n$  components

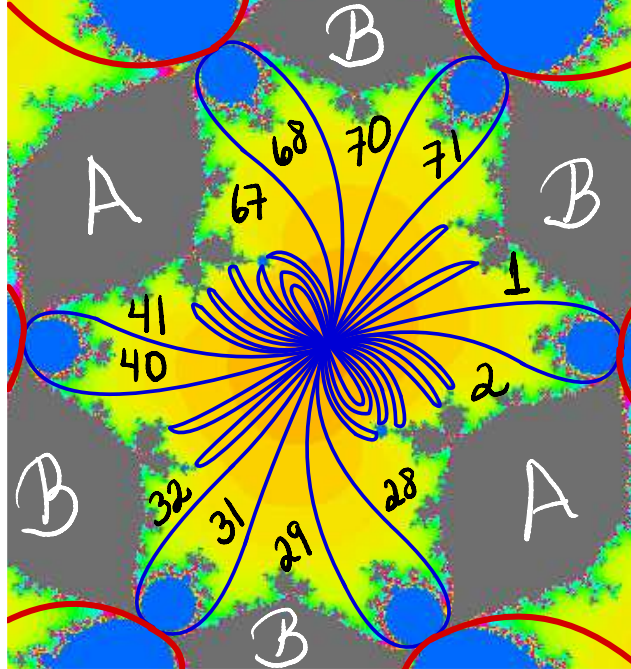


Figure 54: The  $1/3$ -rabbit region in  $\mathcal{S}_3$ . There are  $2(3^3 - 1) = 52$  rays of co-period three in this region. Twelve of these are connecting rays, labeled by their angles (multiplied by the common denominator of  $78$ ). These form  $6$  primary wakes, each with the smallest possible angular width  $1/78$ . Of the remaining  $36$  rays of co-period  $3$ , note that  $28$  are associated with Type A boundary components, while only  $8$  are associated with Type B components. Each subset of  $\mathcal{E}(1/3)$  bounded by the two connecting rays around an A component has angular width  $26/78 = 1/3$ ; while the analogous subsets adjacent to a B component all have much smaller angular width. The rotation  $\mathcal{I}$  adds  $39 = 78/2$  to each angle.

of type A or B, together with their  $2n$  common parabolic root points, where  $n \geq 2$ . Most of the examples we have seen are rings around the boundary of a rabbit region. Compare Figures 17, 22, 54 and 57. In these cases,  $n$  is always equal to  $p$ , and there are always two diametrically opposite components of Type A, together with  $2n - 2$  components of Type B. This case will be studied in more detail in [BM].

Figure 55 illustrates four rings in  $\mathcal{S}_4$  which are not associated with rabbit regions, but rather are associated with both the double basilica and 1010 regions. Two of these rings have  $n = 2$  with pattern ABAB, while the other two have  $n = 3$  with pattern BBBBBB. Two of these four rings are shown in more detail in Figure 56. The large **X** in the middle of each ring indicates that there is no meaningful way to fill in the center. We could proceed by analytic continuation along any path into the center (as long as we don't hit an ideal point). However different paths to the same point would lead to very different parts of  $\mathcal{S}_4$ .

For each of these four rings choose a smoothly embedded circle which passes through the  $2n$  parabolic points, connecting them through the  $2n$  A or B components.

**Lemma 4.12** (Splitting  $\bar{\mathcal{S}}_4$ ). *If we cut  $\bar{\mathcal{S}}_4$  open along all four of these embedded circles, then it will be split as the union of two connected Riemann-surfaces-with-boundary,  $S$  and*

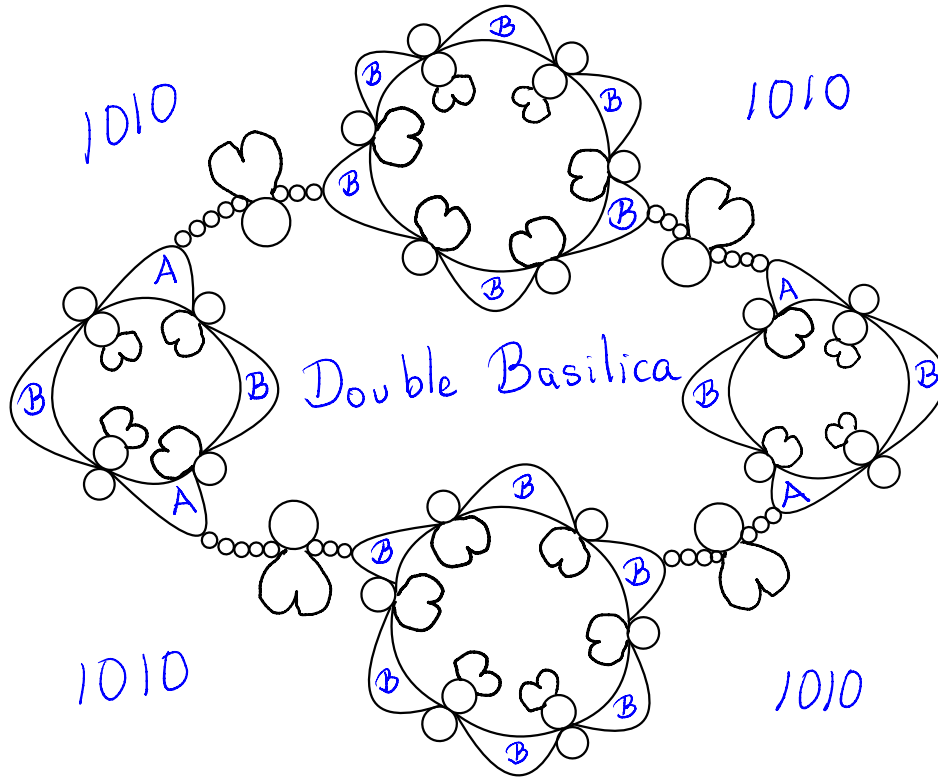


Figure 55: Cartoon illustrating the Double Basilica and 1010 regions of  $\bar{S}_4$  which are separated from the rest of  $\bar{S}_4$  by four rings. All of the rest of  $\bar{S}_4$  can be reached by passing through any one of these rings; but cannot be represented in any meaningful way in this figure.

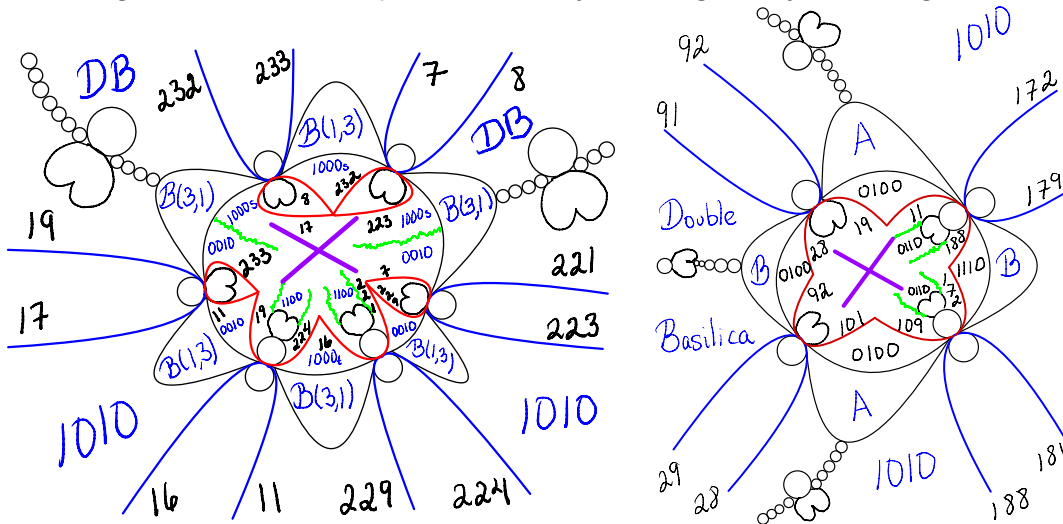


Figure 56: On the left: a more detailed picture of the bottom ring in Figure 55. As we circle once around the outside of this ring, note that the corresponding angles circle twice around  $\mathbb{R}/\mathbb{Z}$ . On the right: a more detailed picture of the right hand ring. The type B components in this ring are of type  $B(2, 2)$ , i.e., they are weakly self-dual.

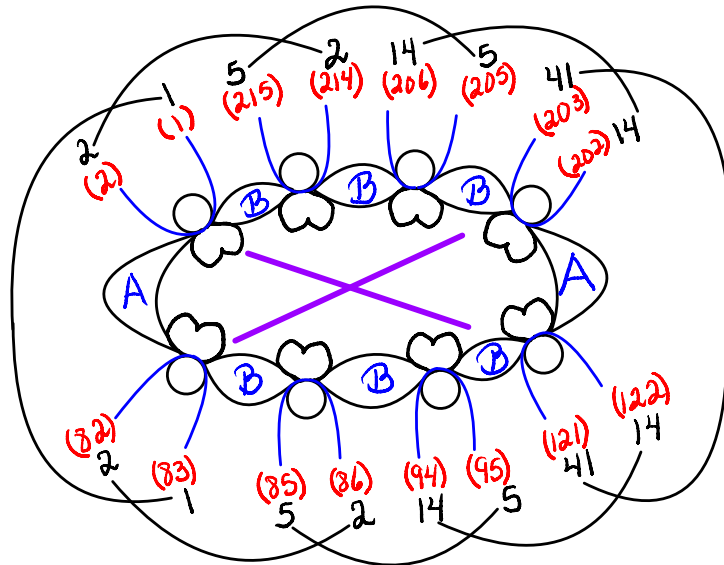


Figure 57: Cartoon illustrating the ring around the  $1/4$ -rabbit region. Here the rabbit region is outside of the ring, while the rest of  $\bar{S}_4$  is not shown. The actual parameter angles are shown in red, while labels for the associated grand orbits are shown in black. (Compare Definition 3.21.) Note that each A or B component is associated with a corresponding grand orbit; and that complex conjugate components share the same grand orbit.

$S'$ , which intersect only along the four common boundary circles. Here the surface  $S$ , as shown in Figure 55, has genus zero and contains the double basilica escape region and the 1010 escape region; while the other surface  $S'$  has genus twelve and contains all of the other 18 escape regions. The surface  $S$  contains all of the primary rays which land at one of the parabolic boundary points; while  $S'$  contains all such secondary rays.

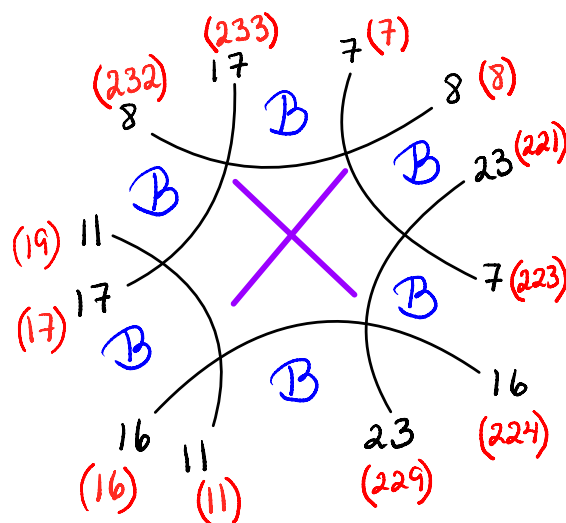


Figure 58: Angles and grand orbits for Figure 56-left, with notation as in Figure 57.

**Proof of Lemma 4.12.** The surface  $S$  is clearly connected, and of genus zero. To show that  $S'$  is connected, we first consider the quotient  $S'/\mathcal{I}$  where  $\mathcal{I}$  is the standard involution (= 180 degree rotation). Figure 11 of [BKM], together with the accompanying text, gives a complete description of the quotient  $\bar{S}_4/\mathcal{I}$ . In this figure, the notation **d** stands for the Double Basilica region, while **5** stands for the 1010 region, and **7** for the 1110 region. Examining this figure, it is not hard to check that if we remove the **d** and **5** regions, what is left is still connected. This proves that  $S'/\mathcal{I}$  is connected. Since the **7** region is  $\mathcal{I}$ -invariant, it follows easily that  $S'$  itself is connected.

Let  $g$  be the genus of  $S'$ . The computation of  $g$  is a fairly straightforward Euler characteristic computation. Let  $S' \cup \text{disks}$  be the closed Riemann surface of the same genus  $g$  which is obtained by pasting a closed disk into each of the four boundary circles. Then the Euler characteristic

$$\chi(S' \cup \text{disks}) = \chi(S') + 4$$

is equal to  $2 - 2g$ , or in other words  $\chi(S') = -2 - 2g$ . Since  $S$  has genus zero, a similar computation shows that  $\chi(S) = -2$ . Furthermore, since  $\chi(S \cap S') = 0$  it follows that

$$\chi(\bar{S}_4) = \chi(S) + \chi(S') = -2 + (-2 - 2g) = -4 - 2g .$$

since the Euler characteristic of  $\bar{S}_4$  is  $2 - (2 \times 15) = -28$ , we can solve for  $g = 12$ .  $\square$

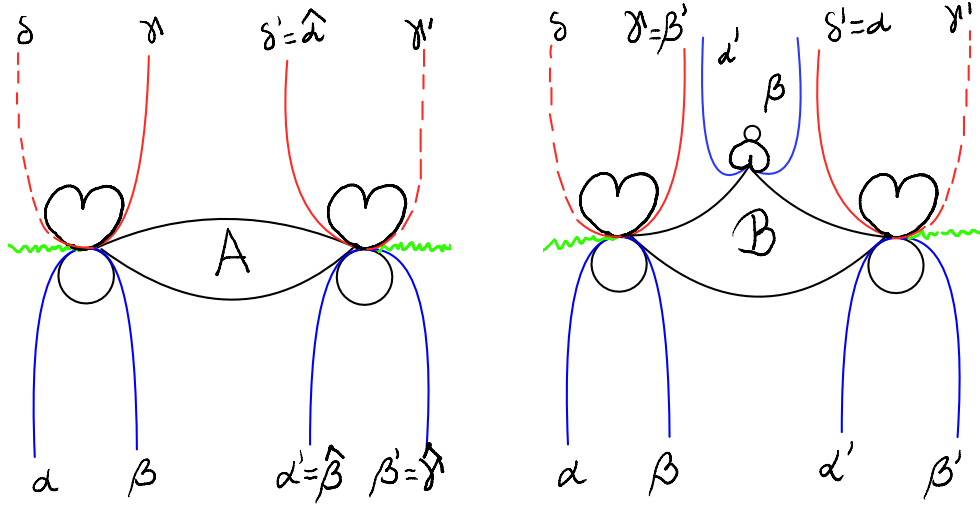


Figure 59: On the left: two four ray points separated by an A component. On the right: separated by a B component

**Remark 4.13 (Neighboring Four Ray Points).** As we circle around such a ring, we repeatedly encounter four ray points separated by an A or B component. First consider the case of an A component, as illustrated in Figure 59-left. If the  $\alpha$ ,  $\beta$ ,  $\gamma$ , and  $\delta$  rays land on the left root point, as illustrated, then the twin rays  $\hat{\alpha}$ ,  $\hat{\beta}$ ,  $\hat{\gamma}$ , and  $\hat{\delta}$  must land in the same

cyclic order around the right hand root point. (Compare Remark 2.30.) In fact they always seem to land as indicated, with

$$\alpha' = \widehat{\beta}, \quad \beta' = \widehat{\gamma}, \quad \text{and} \quad \delta' = \widehat{\alpha}.$$

Recall that  $\alpha$  and  $\gamma$  always belong to the same grand orbit, which also contains  $\widehat{\gamma} = \beta'$ . It follows that  $\alpha$  and  $\beta'$  belong to the same grand orbit:  $((\alpha)) = ((\beta'))$ . Similarly, since  $\beta$  and  $\delta$  belong to the same orbit, and  $\alpha' = \widehat{\beta}$ , consequently  $((\alpha')) = ((\beta))$ . Assuming as in Equation (12) that  $((\alpha)) \neq ((\beta))$  it follows that

$$((\alpha)) = ((\gamma)) = ((\beta')) = ((\delta')) \neq ((\alpha')) = ((\gamma')) = ((\beta)) = ((\delta)).$$

The key to understanding this situation is to look at the Julia set for the parabolic root points. Since the two root points of an A component are dual to each other, they have Julia sets which are identical, except for the choice of which component to label as  $a$  and which to label as  $-a$ .

Nearly all of the examples we know are for rabbit regions. As one specific example, let us concentrate on the  $1/3$ -rabbit region as shown in Figure 54, and on the A component in the upper left of this Figure. Figure 60 illustrates the Julia set for either of its two root points. (See Figure 21 for an analogous Julia set for the  $1/2$  rabbit, and Figure 23 for the  $1/5$  rabbit.)

Given any co-periodic angle  $\theta$  with denominator  $3(3^p - 1)$ , it is useful to consider the corresponding periodic angle  $3\theta$  with denominator  $3^p - 1$ . Note that two co-periodic angles  $\theta$  and  $\theta'$  satisfy  $3\theta = 3\theta'$  if and only if they are twins.

In our example, the root point of each  $\pm 2a$  component in the Julia set is the landing point of six dynamic rays. However, only four of the six dynamic angles correspond to parameter angles for rays landing at the specified root point of A. Below is a table describing the angles for the six dynamic rays landing at the left hand root point in Figure 54 (or 60), and specifying which four are the angles of parameter rays landing on a root of A.

	$\gamma$	$\delta$	$\alpha$	$\beta$	
angles :	16	19	22	31	40 41 /78
$\times 3 :$	16	19	22	5	14 15 /26

Here is the corresponding table for the right hand root points.

	$\alpha'$	$\beta'$	$\gamma'$	$\delta'$	
angles :	67	68	71	74	5 14 /78
$\times 3 :$	15	16	19	22	5 14 /26

Evidently the last row of the second table is just the last row of the first table permuted cyclically. It follows that the angles in the second table are just the twins of the angles in the first table, again permuted cyclically. In particular

$$\alpha' = \widehat{\beta}, \quad \beta' = \widehat{\gamma}, \quad \text{and} \quad \delta' = \widehat{\alpha}.$$

However the twin  $\widehat{\delta}$  is an angle which does not correspond to any parameter ray landing at a root point of this A component, and the same is true for  $\widehat{\gamma}'$ .

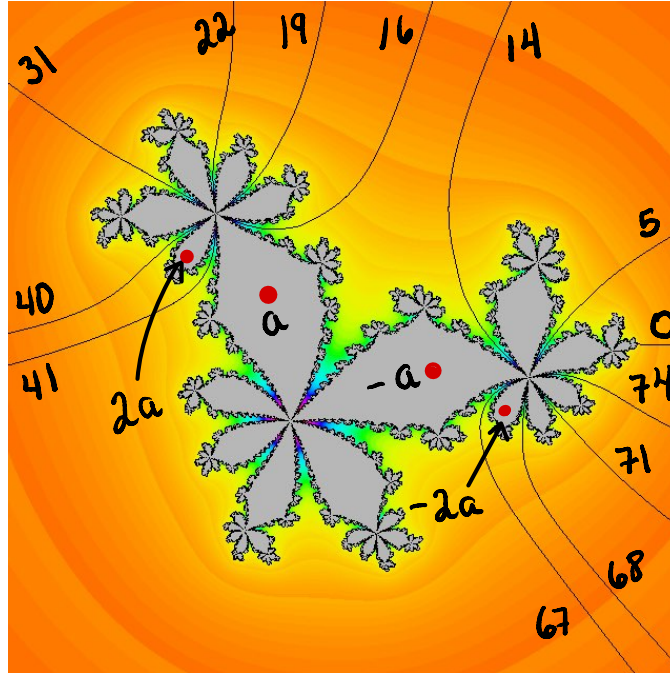


Figure 60: Julia set for the root point of an A component in a  $1/3$ -rabbit, with angles modulo 78, illustrating the tables above.

Similar remarks apply to any A component for an  $n/p$  rabbit ring with  $p \geq 3$ . However for  $p = 2$ , as in Figure 21, there are only four rays landing at the root points of the  $\pm 2a$  components. Therefore, in this case we get the extra relation  $\gamma' = \widehat{\delta}$ . Similarly we get this extra relation for the left and right rings in Figure 55, in a case with  $p = 4$ . This is probably the case since in both cases previously described the type B components are of type  $B(2, 2)$ , hence weakly self-dual.

The B case, as shown in Figure 59-right, is quite different. There are now ten angles to compare, rather than eight, and twin angles do not play any role, since type B components of types  $B(1,3)$  or  $B(3,1)$  are never weakly self-dual. Each of the four angles in the lower half of the figure is duplicated once in the upper half. The two outer angles above,  $\delta$  and  $\gamma'$  do not occur below. However  $\delta$  belongs to the same grand orbit as  $\beta$ , and  $\gamma'$  belongs to the same grand orbit as  $\alpha'$ . Thus we have three grand orbits

$$((\alpha)) = ((\gamma)) = ((\beta')) = ((\delta')), \quad ((\beta)) = ((\delta)), \quad \text{and} \quad ((\alpha')) = ((\gamma')),$$

which are conjecturally always distinct.

In the special case of a ring consisting only of components of type B, as in Figure 56-left, there is a simple explicit description. Let  $m$  be the number of B components in the ring. (Perhaps this number is always even, but we are not at all sure of this.) Let us label the components in cyclic order as  $B_1, B_2, \dots, B_m$ . Let  $O_j$  be the common grand orbit for the  $\alpha$  and  $\beta'$  angles of  $B_j$ . Here  $j$  should be understood as an integer modulo  $m$ . Then as we go around the ring, the four grand orbits associated with  $B_j$  are respectively

$$O_j, O_{j-1}, O_{j+1}, O_j.$$

Each  $O_j$  occurs twice, and there are a total of  $m$  grand orbits, conjecturally all distinct.

In all other cases that we have seen, there are two diametrically opposite A components and  $n - 2$  B components. We will number the components as

$$A_0, B_1, \dots, B_{n-1}, A_n, B_{n+1}, \dots, B_{2n-1} .$$

Then conjecturally the grand orbit  $O_j$  associated with  $A_j$  or  $B_j$  satisfies  $O_j = O_{2n-j}$  for all  $j$ , but no other equalities. Thus in this case there are  $n + 1$  distinct grand orbits. Compare Figures 17 and 56-right for the case  $n = 2$ , Figure 54 for  $n = 3$ , and 57 for  $n = 4$ .

However there is one difference between the rings surrounding rabbit regions and the similar rings in Figure 56. Each rabbit region in  $\overline{\mathcal{S}}_p$  is invariant under the  $180^\circ$  rotation  $\mathcal{I}$  of  $\overline{\mathcal{S}}_p$ . Hence each parameter angle  $\theta_j$  around such a rabbit ring satisfies

$$\theta_{j+p} = \theta_j \pm 3(3^p - 1)/2 .$$

On the other hand,  $\mathcal{I}$  interchanges the left and right rings of Figure 56. Therefore for each angle  $\theta_j$  in one of these rings, the ray of angle  $\theta_j \pm 3(3^p - 1)/2$  lands in the opposite ring. A similar remark applies to the upper and lower rings in Figure 56.

**Remark 4.14 (Three versus Four).** There is a strong resemblance between the four ray cases described above and the corresponding three ray cases of Figures 47 and 49. More explicitly, if we delete the  $\delta$  and  $\gamma'$  rays in Figure 59 and change the label  $\delta'$  to  $\gamma'$ , then we will get the equivalent of Figures 47 and 49. However there is one essential difference: There are always more distinct grand orbits in the three ray case.

**Remark 4.15 (Small Mandelbrot Copies).** The space  $\mathcal{S}_3$  contains many Mandelbrot copies which lie on the boundary between two different escape regions. More precisely there are three possibilities: Such a copy  $M$  lies:

**On one side** of the boundary if its cusp point is the only point which is a boundary point of two escape regions (Figure 42). It lies:

**Across** the boundary if the boundary cuts across at a parabolic point which bisects  $M$  (Figures 61 and 62) or:

**Along** the boundary if there are many components of  $M$  which have boundary points on both of the two escape region boundaries. (See Figure 40.)

In fact any part of the boundary which shows up as a thin wiggly line in our large scale pictures will contain many such copies. Compare Figures 40 and 42. Note that the size of a Mandelbrot copy of period  $q$  in  $\mathcal{S}_p$  tends to shrink exponentially as  $q$  increases with fixed  $p$ ; so most of these copies are extremely small.



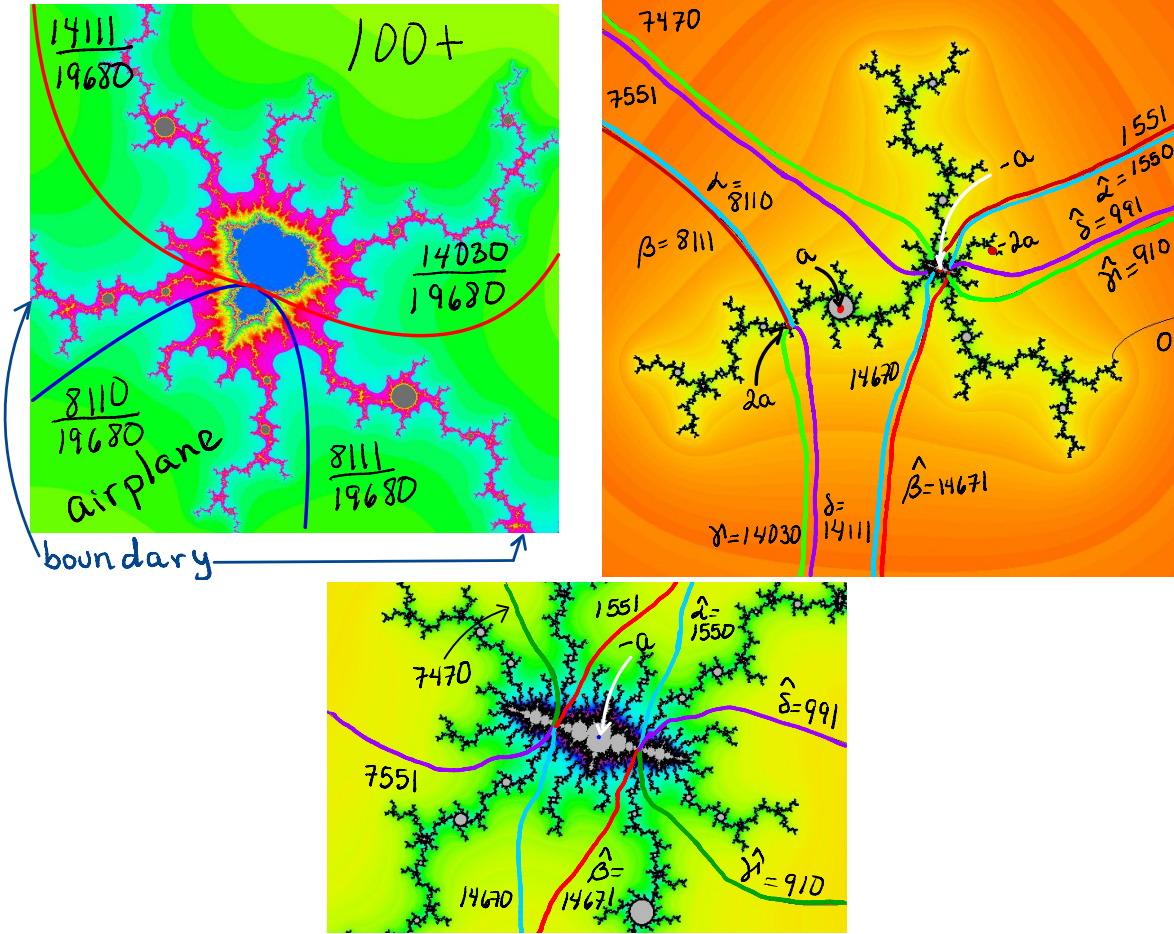


Figure 62: On the left: a small Mandelbrot copy of period 4 across the boundary between the airplane and 100+ regions of  $\mathcal{S}_3$ . On the right: Julia set for the center point of its 1/2 limb. Below: a magnified picture around the  $-2a$  component. The denominator is  $3(3^8 - 1) = 19680$ . The periodic dynamic rays land at the point of period two which lies between  $-a$  and  $F^{\circ 2}(-a)$ ; while associated co-periodic rays land at the pre-image of the fixed point which lies to the right of  $-a$ . The twin co-periodic rays land at the root point of the  $2a$  component.

**Conjecture 4.17 (Across the Boundary Conjecture).** *If a Mandelbrot copy in  $\mathcal{S}_p$  cuts across the boundary between two escape regions at a parabolic point of period  $q$ , then there are  $4$  parameter rays landing on  $\mathfrak{p}$ . In the Julia set for  $\mathfrak{p}$  there are  $4$  corresponding triads. Now suppose that  $p \neq q$ . The periodic dynamic rays  $\theta_q$  land at the point of period at least two which lies between the marked critical point  $a$  and the free critical point  $-a$ . The co-periodic rays  $\theta$  land at the root point of the hyperbolic component containing  $2a$ , and their corresponding twin rays  $\hat{\theta}$  land on a preimage of  $-a$ . Here the mid-point between the periodic point of period  $q \geq 1$ , where the periodic rays  $\theta_q$  land and the landing point of the twin rays  $\hat{\theta}$  is always the free critical point  $-a$ . When the parabolic point  $\mathfrak{p}$  is self dual, as in the case of a type A component, the twin rays land precisely at the root point of  $-2a$ .*

**Note.** In all of the parabolic Julia sets we have seen with four or more dynamic rays landing at a common point, there are four parameter rays landing at the corresponding point in parameter space. On the other hand there can certainly be three dynamic rays landing at a common parabolic point in examples where no three co-periodic parameter rays land together. See for example the landing point of the 62 and 64 rays in Figures 37. (We believe that this happens whenever the two parameter rays belong to the same grand orbit, and  $q$  is odd.)

## 5 Counting

This section will be concerned with the numbers of vertices, edges, and faces in the period  $q$  tessellation  $\mathbf{Tes}_q(\overline{\mathcal{S}}_p)$ . We will give explicit formulas for the number of edges, and (conjecturally at least) for the number of parabolic vertices. The number  $N_p$  of ideal vertices (= number of escape regions) is more difficult; but has been computed for  $p \leq 26$  by DeMarco and Schiff [DM-S]. The number of faces seems to be even more difficult to compute, so we know it only for small values of  $q$  and  $p$ . (See Table 4 at the end of this section.)

**Definition 5.1.** One important number is the degree  $\mathbf{d}_p$  of the affine curve  $\mathcal{S}_p$ , which is defined uniquely by the recursive formula

$$3^{n-1} = \sum_{p|n} \mathbf{d}_p.$$

The first few values are shown in Table 1. Note that  $\mathbf{d}_p \sim 3^{p-1}$  as  $p \rightarrow \infty$ .

$p :$	1	2	3	4	5	6	7	8	9	...
$\mathbf{d}_p :$	1	2	8	24	80	232	728	2160	6552	...

Table 1: The degree  $\mathbf{d}_p$  of  $\mathcal{S}_p$ .

This number  $\mathbf{d}_p$  is also equal to the number of hyperbolic components of Type A in  $\mathcal{S}_p$ . (See [M4, Lemma 5.4].) For each  $m, n > 0$  with  $m + n = p$ , the number of components of Type B( $m, n$ ) in  $\mathcal{S}_p$  is also equal to  $\mathbf{d}_p$  (See Theorem 5.4.). Furthermore, the number of escape regions in  $\mathcal{S}_p$  **counted with multiplicity** is also equal to  $\mathbf{d}_p$ . (Compare [M4, Remark 5.5 and Corollary 5.12].)

The actual number  $N_p$  of escape regions in  $\mathcal{S}_p$  is much more difficult to determine. For relatively small values of  $p$  it has been computed by DeMarco and Schiff [DM-S]. Here are a few values.

Note that the ratio  $\mathbf{d}_p/N_p \geq 1$  can be described as the **average multiplicity** of the various escape regions in  $\mathcal{S}_p$ . (Compare Figure 64 and Remark 5.12.)

For any tessellation of a compact surface into simply-connected faces, the classical Euler characteristic formula takes the form  $\mathbf{v} - \mathbf{e} + \mathbf{f} = \chi(\overline{\mathcal{S}})$ , where  $\mathbf{v}$  is the number of

$p :$	1	2	3	4	5	6	7	8	9	$\dots$
$N_p :$	1	2	8	20	56	144	404	1112	3120	$\dots$

Table 2: The number of escape regions in  $\mathcal{S}_p$ .

vertices,  $\mathbf{e}$  is the number of edges, and  $\mathbf{f}$  is the number of faces. However, in all of our tessellations  $\mathbf{Tes}_q(\overline{\mathcal{S}}_p)$  with  $1 < n \neq q$ , some of the faces are not simply-connected, so a correction term is needed. The appropriate corrected formula is

$$\mathbf{v} - \mathbf{e} + \mathbf{f} = \chi(\overline{\mathcal{S}}) + \text{rank}(H_1(\mathcal{F}^\cup)) = \chi(\overline{\mathcal{S}}) + \sum_k \text{rank}(H_1(\mathcal{F}_k)) , \quad (15)$$

using homology with rational coefficients,<sup>11</sup> where  $\mathcal{F}^\cup = \bigcup \mathcal{F}_k$  is the union of the open faces.

Here the Euler characteristic of the compactified moduli space is related to the number  $N_p$  of escape regions by the formula

$$\chi(\overline{\mathcal{S}}_p) = 2 - 2\mathbf{g} = N_p + (2 - p)\mathbf{d}_p . \quad (16)$$

Thus the genus

$$\mathbf{g} = 1 + ((p - 2)\mathbf{d}_p - N_p)/2 > (p - 3)\mathbf{d}_p/2$$

grows very rapidly with  $p$ . (See [BKM, Theorem 7.2].) Here the term  $(2 - p)\mathbf{d}_p$  can be described as the Euler characteristic of the open manifold  $\mathcal{S}_p$ , or of the connectedness locus which is a nested intersection of deformation retracts of  $\mathcal{S}_p$ .

**Angles.** The number of periodic angles of period  $q$  can easily be computed as

$$\# \text{ period } q = \begin{cases} 2 & \text{if } q = 1 , \\ 3\mathbf{d}_q & \text{if } q > 1 . \end{cases} \quad (17)$$

To obtain the number of co-periodic angles  $\theta \pm 1/3$  we must multiply these numbers by two. Here is a list of the first few values

$q :$	1	2	3	4	5	6	7	8	$\dots$
periodic angles:	2	6	24	72	240	696	2184	6480	$\dots$
co-periodic:	4	12	48	144	480	1392	4368	12960	$\dots$

Table 3: The number of angles of period or co-period  $q$ .

**Edges.** The number  $\mathbf{e}$  of edges in our tessellation is equal to the product of the number of angles of co-period  $q$ , and the number of escape regions counted with multiplicity. Thus it is given by

$$\mathbf{e} = \mathbf{e}_q(\mathcal{S}_p) = \begin{cases} 4\mathbf{d}_p & \text{for } q = 1 , \text{ but} \\ 6\mathbf{d}_q\mathbf{d}_p & \text{for } q > 1 . \end{cases} \quad (18)$$

<sup>11</sup>There is no torsion in the cases we consider, so it doesn't matter what coefficient field we use.

**Vertices.** We must distinguish between ideal vertices and parabolic vertices. The number of ideal vertices is clearly equal to the number  $N_p$  of escape regions, as listed above.

To compute the number of parabolic vertices, we proceed as follows. By definition a hyperbolic component in  $\mathcal{S}_p$  is of Type D  $(q, p)$  if the free critical orbit for its center map is periodic of period  $q$ , and is disjoint from the marked critical orbit. (Here the use of a double index is convenient, since there is a natural one-to-one correspondence between components of type D  $(q)$  in  $\mathcal{S}_p$  and their dual components of Type D  $(p)$  in  $\mathcal{S}_q$  with  $p \neq q$ .)

**Lemma 5.2.** *If we assume the Conjecture MC1 of Remark 2.28, then it follows that there is a one-to-one correspondence between components of Type D  $(q)$  in  $\mathcal{S}_p$  and parabolic vertices in  $\mathbf{Tes}_q(\overline{\mathcal{S}}_p)$ .*

*Proof.* This conjecture implies that no two components of Type D can have the same root point, and the conclusion follows immediately.  $\square$

**Lemma 5.3.** *For every  $p$  there are precisely  $3\mathbf{d}_p^2$  hyperbolic components of Type either A, B, or D  $(p, p)$  in the curve  $\mathcal{S}_p$ . Similarly, for  $q \neq p$ , there are precisely  $3\mathbf{d}_q\mathbf{d}_p$  components of Type D  $(q, p)$  in  $\mathcal{S}_p$ .*

The proof in [M4, Lemma 5.8] involves the dual curve  $\mathcal{S}'_q$  consisting of all pairs  $(a, v) \in \mathbb{C}^2$  such that the critical point  $-a$  has period exactly  $q$  under the usual map  $F(z) = z^3 - 3a^2z + (2a^3 + v)$ . This dual curve has degree  $3\mathbf{d}_q$  in  $\mathbb{C}^2$ . It is important to note that the two curves  $\mathcal{S}_p$  and  $\mathcal{S}'_q$  intersect transversally. This transversality can be proved using Thurston's basic construction of rational maps from topological data. (See [DH2].) A purely algebraic proof of transversality has been provided by Silverman [Si]. The number of intersections between these two curves is then counted using Bezout's Theorem. When  $p \neq q$ , the intersection points are precisely the centers of components of Type D  $(q, p)$ ; but for  $q = p$  the centers of A and B components are also included in this count.  $\square$

As an immediate consequence, assuming Conjecture MC1, we have the following formula for the number of parabolic vertices in  $\mathbf{Tes}_q(\overline{\mathcal{S}}_p)$ .

$$\mathbf{v}_{\text{par}} = 3\mathbf{d}_q\mathbf{d}_p \quad \text{whenever } q \neq p. \quad (19)$$

On the other hand, for  $q = p$  we need to count the number of components of Type A and B in order to compute  $\mathbf{v}_{\text{par}}$ . The number of components of Type A in  $\mathcal{S}_p$  is precisely equal to  $\mathbf{d}_p$ . See [M4, Lemma 5.4] and its proof. For Type B we proceed as follows.

### Counting Type B Components.

By definition a hyperbolic component in  $\mathcal{S}_p$  is of Type B  $(m, n)$  if its center point  $F$  satisfies  $F^{\circ m}(a) = -a$  and  $F^{\circ n}(-a) = a$ , where  $m + n = p$ .

**Theorem 5.4.** *For each  $m, n > 0$  with  $m + n = p$  the number of components of Type B  $(m, n)$  in  $\mathcal{S}_p$  is equal to the degree  $\mathbf{d}_p$  of the curve  $\mathcal{S}_p$ .*

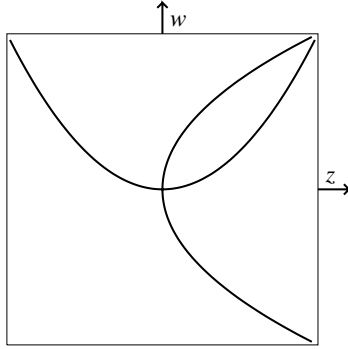


Figure 63: Two transverse curves.

The proof proceeds as follows.

Let  $\mathcal{S} \cong \mathbb{C}^2$  be the full space of maps  $F = z^3 - 3a^2z + 2a^3 + v$ . For any  $m, n \geq 0$  with  $m + n > 0$ , let  $\mathcal{B}(m, n) \subset \mathcal{S}$  be the finite subset consisting of all  $F$  which satisfy the equations

$$F^{\circ m}(a) = -a \quad \text{and} \quad F^{\circ n}(-a) = a .$$

Note that  $\mathcal{B}(m, n) \subset \mathcal{B}(km, kn)$  for any  $k > 0$ . If  $m + n = p$ , the subset  $\mathcal{B}(m, n) \cap \mathcal{S}_p$  will be denoted by  $\mathcal{B}_0(m, n)$ . Evidently  $\mathcal{B}_0(m, n)$  is precisely the set of all center points of hyperbolic components of Type B  $(m, n)$  in  $\mathcal{S}_{m+n}$ .

**Caution:** The sets  $\mathcal{B}(0, p)$  and  $\mathcal{B}(p, 0)$  are identical, and should not be distinguished from each other. This set  $\mathcal{B}(0, p) = \mathcal{B}(p, 0)$  can be described as the set of all unicritical maps  $F(z) = z^3 + v$  for which  $F^{\circ p}(0) = 0$ . In particular,  $\mathcal{B}(1, 0) = \mathcal{B}(0, 1)$  consists of a single map  $F(z) = z^3$  in  $\mathcal{S}_1$ , and is contained in every  $\mathcal{B}(m, n)$ .

**Lemma 5.5.** *The curves  $F^{\circ m}(a) = -a$  and  $F^{\circ n}(-a) = a$  intersect transversally within  $\mathcal{S}$ , and have precisely  $3^{p-1}$  intersection points.*

*Proof.* We must first prove transversality. Each intersection point is the center of a hyperbolic component in  $\mathcal{S} \cong \mathbb{C}^2$ . The paper [M4] provides a canonical biholomorphic model for such hyperbolic components. In this particular case, the model is a polynomial map from the disjoint union of two copies of  $\mathbb{C}$  to itself. If  $z$  is the coordinate for the first copy and  $w$  for the second, then the map sends  $z$  to  $w = z^2$  and  $w$  to  $z = w^2$ . If we restrict to the case where  $z$  and  $w$  are real, then the graphs of these two maps are shown in Figure 63. Evidently these graphs intersect transversally, so the corresponding complex graphs also intersect transversally.

The conclusion then follows easily from Bezout's Theorem. (Note that the equation  $F^{\circ m}(a) = -a$  has degree  $3^{m-1}$  when  $m > 0$ , since it can be written as  $F^{\circ m-1}(v) = -a$ . Bezout's Theorem must actually be applied in the complex projective plane which is obtained from  $\mathcal{S}$  by adding a line at infinity; but it is not hard to check that there are no intersection points on this line at infinity.)  $\square$

**Lemma 5.6.** *Suppose that  $m' \leq m$  and  $n' \leq n$ . Then  $\mathcal{B}(m', n') \subset \mathcal{B}(m, n)$  if and only if*

$$m \equiv m' \quad \text{and} \quad n \equiv n' \quad \text{modulo} \quad p' = m' + n'. \quad (20)$$

*In particular, whenever  $\mathcal{B}(m', n') \subset \mathcal{B}(m, n)$  it follows that  $p = m + n \equiv 0 \pmod{p'}$ .*

The proof is straightforward. Any map  $F \in \mathcal{B}(m', n')$  certainly satisfies  $F^{\circ p'}(a) = a$ . Given (20), since  $m \equiv m' \pmod{p'}$ , we can write  $m = m' + kp'$  for some  $k$ ; and it follows that  $F^{\circ m}(a) = F^{\circ m'}(a) = -a$ . On the other hand, given that  $\mathcal{B}(m', n') \subset \mathcal{B}(m, n)$ , choose some  $F \in \mathcal{B}_0(m', n')$ . Then  $F^{\circ j}(a) = -a$  if and only if  $j \equiv m' \pmod{p'}$ . But  $F$  must also belong to  $\mathcal{B}(m, n)$ , hence  $F^{\circ m}(a) = -a$ , which proves that  $m \equiv m' \pmod{p'}$ .  $\square$

**Lemma 5.7.** *For any divisor  $p'$  of  $p$  we can write*

$$\mathcal{B}(m, n) \cap \mathcal{S}_{p'} = \mathcal{B}_0(m', n'),$$

*where the integers  $m'$  and  $n'$  are uniquely determined by the conditions that*

$$m' + n' = p', \quad m' \equiv m, \quad \text{and} \quad n' \equiv n \quad \text{modulo} \quad p'.$$

*Proof.* This follows immediately from Lemma 5.6. In fact, for each  $p'$  there is a unique  $0 < m' \leq p'$  with  $m' \equiv m \pmod{p'}$ . Then  $n' = p' - m'$  must satisfy  $n' \equiv n \pmod{p'}$ .  $\square$

**Lemma 5.8.** *The set  $\mathcal{B}(m, n)$  is the disjoint union of the sets  $\mathcal{B}(m, n) \cap \mathcal{S}_{p'}$  as  $p'$  varies over all divisors of  $p$ . Since  $\mathcal{B}(m, n)$  has  $3^{p-1}$  elements, and since  $\mathcal{B}(1, 0)$  has  $\mathbf{d}_1 = 1$  element, it follows inductively from the defining formula*

$$3^{p-1} = \sum_{p'|p} \mathbf{d}_{p'}$$

*that  $\mathcal{B}_0(m, n)$  has  $\mathbf{d}_p$  elements.*

The proof is straightforward; and Theorem 5.4 follows immediately.  $\square$

**Theorem 5.9.** *Assuming the Mandelbrot Copy Conjecture MC1, it follows that the number of parabolic vertices in  $\mathbf{Tes}_q(\overline{\mathcal{S}}_p)$  is equal to  $3\mathbf{d}_q\mathbf{d}_p$  if  $p \neq q$ , but is equal to  $3\mathbf{d}_p^2 - p\mathbf{d}_p$  if  $p = q$ .*

*Proof.* We have shown that  $\mathcal{S}_p$  contains  $(p-1)\mathbf{d}_p$  components of Type B plus  $\mathbf{d}_p$  components of Type A, yielding a total of  $p\mathbf{d}_p$  components of Types A and D. Combining this with Lemmas 5.2 and 5.3, the conclusion follows.  $\square$

**Remark 5.10.** If we combine Theorem 5.9 with the Equations (16) and (18), then we can solve for the number  $\mathbf{f}$  of faces, yielding

$$\mathbf{f} = \begin{cases} 3 \mathbf{d}_q \mathbf{d}_p + 2 \mathbf{d}_p - p \mathbf{d}_p + \text{rank}(H_1(\mathcal{F}^\cup)) & \text{if } p \neq q > 1 \\ 3 \mathbf{d}_p^2 + 2 \mathbf{d}_p + \text{rank}(H_1(\mathcal{F}^\cup)) & \text{if } p = q > 1 ; \end{cases}$$

with similar formulas when  $q = 1$ . (Thus the  $N_p$  terms cancel out.) When  $p = q$  it seems possible that all faces are simply connected, so that the last term is always zero. But for  $p \neq q$  and  $p > 1$ , there are always faces surrounding the rabbit regions which are not simply connected by [BM, Corollary 4.3], so that the last term is always strictly positive.

**Counting Non-Simply Connected Faces.** To compute the rank of  $H_1(\mathcal{F}^\cup)$ , note first that the inclusion map

$$i : \mathcal{F}^\cup \rightarrow \overline{\mathcal{S}}_p$$

induces a homomorphism  $i_* : H_1(\mathcal{F}^\cup) \rightarrow H_1(\overline{\mathcal{S}}_p)$ . It follows that

$$\text{rank}(H_1(\mathcal{F}^\cup)) = \text{rank}(\text{kernel}(i_*)) + \text{rank}(\text{image}(i_*)). \quad (21)$$

Alternatively we can compute these two summands in terms of the **1-skeleton**  $X = \overline{\mathcal{S}}_p \setminus \mathcal{F}$  of  $\mathbf{Tes}_q(\overline{\mathcal{S}}_p)$ , that is, the union of all vertices and edges.

More generally, let  $S$  be any closed Riemann surface of genus  $\mathbf{g}$ , and let  $X$  be any non-vacuous finite graph which is embedded in  $S$ . (In our application,  $X$  will be the 1-skeleton and its complement will be the union  $\mathcal{F}^\cup$  of faces.)

**Theorem 5.11 (Lefschetz Duality).** *The kernel of the natural homomorphism*

$$h : H_1(S \setminus X) \rightarrow H_1(S) \quad (22)$$

*has rank equal to one less than the number of connected components of  $X$ . Furthermore the sum of the ranks of the images of the homomorphism (22) and of the corresponding homomorphism  $H_1(X) \rightarrow H_1(S)$  is always equal to the rank  $2\mathbf{g}$  of  $H_1(S)$ .*

*Proof.* Here coefficients in the rational field  $\mathbb{Q}$  are to be understood. Hence any cohomology group  $H^j(*)$  can be identified with the dual  $\text{Hom}(H_j(*), \mathbb{Q})$  of the corresponding homology group.

The Lefschetz Duality Theorem<sup>12</sup> then asserts that the following two exact sequences are dually paired to each other.

$$H_2(S) \rightarrow H_2(S, S \setminus X) \rightarrow H_1(S \setminus X) \rightarrow H_1(S) \rightarrow H_1(S, S \setminus X)$$

$$H_0(S) \longleftarrow H_0(X) \longleftarrow H_1(S, X) \longleftarrow H_1(S) \longleftarrow H_1(X)$$

That is, each group or homomorphism above is naturally isomorphic to the dual of the group or homomorphism below it. In particular, the second homomorphism above has rank equal

---

<sup>12</sup>See for example [Ha] or [Sp]. The Lefschetz Theorem is an amalgamation of Poincaré and Alexander duality.

to the rank of the kernel of the homomorphism (22). This is equal to the rank of the second homomorphism below, which is easily seen to be one less than the number of connected components of  $X$ .

On the other hand, the rank of  $H_1(S)$ , either above or below, is equal to the sum of the ranks of the homomorphisms to and from it. This implies that it is equal to the sum of the ranks of  $H_1(S \setminus X) \rightarrow H_1(S)$  and  $H_1(X) \rightarrow H_1(S)$ , as asserted.  $\square$

As an immediate corollary, if all faces of the tessellation are simply connected, then it follows that the 1-skeleton is connected. (It seems quite possible that all faces are simply connected whenever either  $p = q$  or  $p = 1$ ; but we have no proof of this.) Combining the above formulas, this would imply that the number of faces is precisely

$$\mathbf{f} = 3\mathbf{d}_p^2 + 2\mathbf{d}_p$$

when  $p = q > 1$ . However [BM, Corollary 4.3] implies that the 1-skeleton is not connected in all other cases.

For all cases with  $p, q \leq 3$  see Table 4. In four of these cases, the 1-skeleton is not connected, which means that there is at least one face which is not simply-connected. For example  $\mathbf{Tes}_2(\mathcal{S}_3)$  has 40 simply-connected faces, but the two faces surrounding the rabbit and co-rabbit have the topology of an annulus, so that the rank of  $H_1(\mathcal{F}^\cup)$  is two. Here is a table showing numbers of vertices, faces and edges for small values of  $p$  and  $q$ .

$q$	$p$	vertices $N_p + \mathbf{v}_{\text{par}}$	edges $\mathbf{e}$	faces $\mathbf{f}$	$\chi(\mathcal{S}_p)$ $2 - 2\mathbf{g}$	$\text{rank}(H_1(\mathcal{F}^\cup))$ $ \text{kernel}(h)  +  \text{image}(h) $
1	1	1+2	4	3	2	0+0
2	1	1+6	12	7	2	0+0
3	1	1+24	48	25	2	0+0
1	2	2+6	8	3	2	1+0
2	2	2+8	24	16	2	0+0
3	2	2+48	96	49	2	1+0
1	3	8+24	32	9	0	7+2
2	3	8+48	96	42	0	2+0
3	3	8+168	384	208	0	0+0

Table 4: Statistics of  $\mathbf{Tes}_q(\mathcal{S}_p)$  for small  $q$  and  $p$ . The two summands in the third column refer to ideal and parabolic vertices; while the two summands in the last column refer to the kernel and image of the homomorphism  $h : H_1(\mathcal{F}^\cup) \rightarrow H_1(\mathcal{S}_p)$ . Note that

$$\mathbf{v} - \mathbf{e} + \mathbf{f} = \chi(\mathcal{S}_p) + \text{rank}(H_1(\mathcal{F}^\cup))$$

in all cases.

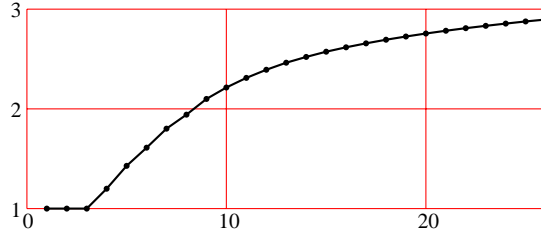


Figure 64: Graph of the ratio  $\mathbf{d}_p/N_p$  as a function of  $p$  (based on numbers from [DM-S]).

**Remark 5.12 (Average Multiplicity of the Escape Regions).** Another interesting number associated with  $\overline{\mathcal{S}}_p$  is the ratio  $r(p) = \mathbf{d}_p/N_p$  which measures the average of the multiplicities of the  $N_p$  escape regions. This seems to increase rather slowly as a function of  $p$ . (See Figure 64.) We have no idea of how to estimate its behavior for large  $p$ . (However, it seems reasonable to guess that the function  $p \mapsto r(p)$  is monotone, with slope tending to zero as  $p \rightarrow \infty$ . It also seem likely, but not at all certain, that it is unbounded.) The Euler characteristic of  $\overline{\mathcal{S}}_p$  can be computed as  $\chi = (1/r(p) + 2 - p)\mathbf{d}_p$ , so it follows that

$$p - 3 \leq -\chi(\overline{\mathcal{S}}_p)/\mathbf{d}_p < p - 2 \quad \text{for all } p.$$

Furthermore it follows that  $r(p) \rightarrow \infty$  as  $p \rightarrow \infty$  if and only if  $p + \chi(\overline{\mathcal{S}}_p)/\mathbf{d}_p$  converges to  $+2$  as  $p \rightarrow \infty$ .

Compare [DM-S, Table 1]; and note that  $\mathbf{d}_p = 3^{p-1} + O(3^{p/2})$ , so that  $3^{p-1}$  is a very good approximation to  $\mathbf{d}_p$  for large  $p$ .

## 6 Misiurewicz Maps and Similarity

Recall that we use the term Misiurewicz map for any  $F \in \mathcal{S}_p$  such that the orbit of the free critical point  $-a$  eventually maps to a repelling periodic orbit. Since  $F(2a) = F(-a)$ , the orbit of  $2a$  eventually maps to the same repelling periodic orbit. But the orbit of the free co-critical point  $2a$  for a Misiurewicz map can never contain a critical point. This leads to a great deal of local self similarity.

Consider for example Figure 65. Here both  $-a$  (at the landing point of the 5 and 11 rays) and  $2a$  (at the landing point of the 17 ray) map to the free critical value (at the landing point of the 15 ray), which maps to a repelling fixed point (at the landing point of the 9 ray which is fixed under tripling mod 18). It follows that the Julia set in a small neighborhood of  $2a$  is conformally isomorphic to the Julia set in a neighborhood of the free critical value, which is conformally isomorphic to the Julia set in the neighborhood of this repelling fixed point. On the other hand, since  $8 \mapsto 6 \mapsto 0$  under tripling mod 18, the tiny configuration at the endpoint of the 8 ray maps conformally onto the larger configuration at the end of the 6 ray, which maps conformally onto the much larger configuration at the end of the 0 ray.

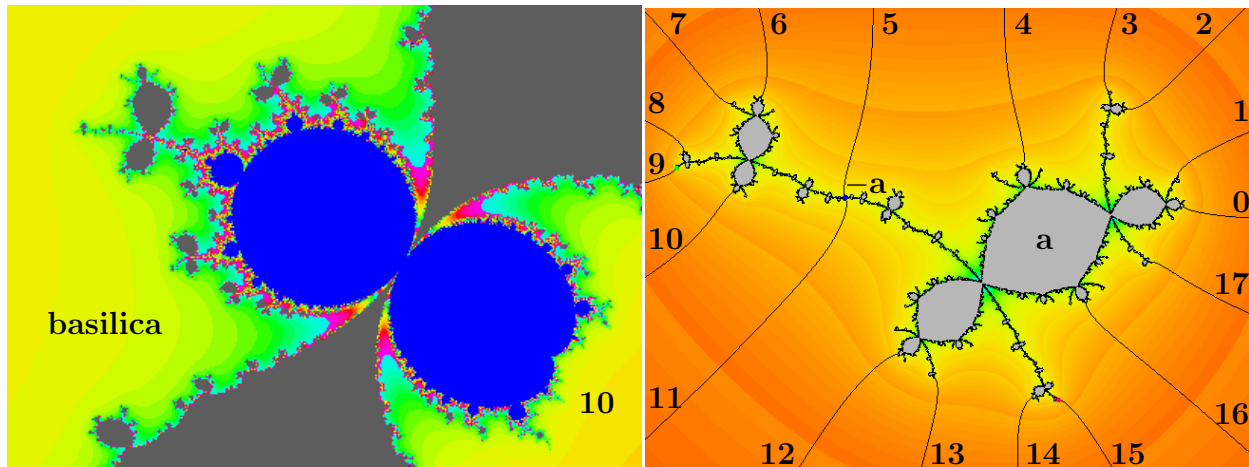


Figure 65: On the left a copy of  $\mathbb{M}$  in  $\mathcal{S}_2$ , between the basilica region to the left and the  $(1, 0)$  region to the right. The Chebyshev point is the landing point of the  $17/18$  parameter ray at the leftmost tip of this copy. (Compare Figure 15 in Section 3 for a picture showing the entire connectedness locus in  $\mathcal{S}_2$ .) On the right is the Julia set for this Chebyshev point. The common denominator 18 is to be understood for all angles. Here  $+a$  is in the largest component; while  $2a$  is at the landing point of the 17 ray; and  $-a$  is at the meeting point of the 5 and 11 rays. Both  $2a$  and  $-a$  map to the landing point of the 15 ray; which maps to the fixed point at the end of the 9 ray.

**Conjecture 6.1 (Tan Lei Similarity).** For quadratic maps, Tan Lei proved that, under increasing magnification, the connectedness locus  $\mathbb{M}$  around a Misiurewicz point  $F \in \mathbb{M}$ , and the filled Julia set of  $F$  at the corresponding repelling point, look more and more alike. (See [TL], [Ka2], [RL].)

We conjecture that the analogous statement holds in  $\mathcal{S}_p$ : Under iterated magnification, the connectedness locus around a Misiurewicz map  $F \in \mathcal{S}_p$  looks more and more alike the filled Julia set of  $F$  around the free co-critical point  $2a_F$  (up to a fixed scale change and rotation).

In fact, since the points in the forward orbit of  $2a$  all have locally conformally isomorphic Julia sets, we could very well substitute any one of these these points for  $2a$ . For example, in Figure 65, the neighborhood of the Chebyshev point in parameter space looks very much like a neighborhood of the post-critical fixed point in the Julia set.

For other examples, see Figures 66, and 67; as well as Figure 5 in Section 2. Also compare the right hand tip of Figure 6 with Figure 17 in Section 3.

Closely related is the observation that a dynamic ray of given angle for a Misiurewicz map  $F \in \mathcal{S}_p$  seems to land at the point  $2a_F$  if and only if there is a parameter ray in  $\mathcal{S}_p$  of the same angle which lands at  $F$ . Furthermore the dynamic and parameter rays land in the same cyclic order, even though the various parameter rays may be contained in different escape regions. (See Figure 66.)

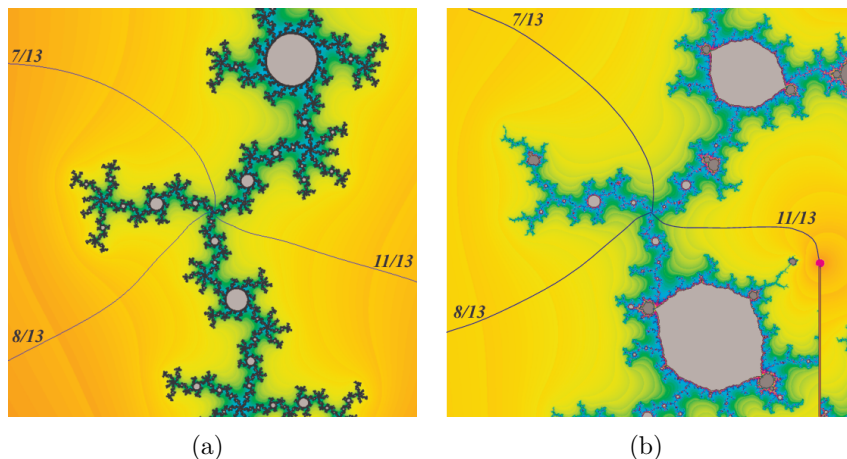


Figure 66: (a) Julia set picture of width 0.96 centered at  $2a$  for a Misiurewicz map  $F_0 \in \mathcal{S}_4$ . In this example,  $2a$  is a fixed point. (b) Corresponding parameter space picture, centered at  $F_0$  and magnified by the complex factor of  $\frac{ds}{dt}(F_0)$ . Here  $t$  is the usual canonical coordinate, and  $s(F) = 2a_F - z_F$  is a dynamically defined local coordinate. (See [BM, Corollary 6.4].) Estimated parameter rays are labeled by the parameter angle. The parameter values are  $a = -0.185084 - 0.358121i$ ,  $v = -0.629660 - 0.752726i$ . The two left parameter rays lie in the Kokopelli escape region, while the right hand ray lies in the 0010 region with multiplicity  $\mu_h = 2$ . (The vertical line on the right is a slit, terminating at the infinite point for this region.) Conjecturally the left and right figures would look more and more alike as we zoom in towards the central point. In other words, there is a Tan Lei type similarity between parameter space and dynamic plane around this point. (Compare Conjecture 6.1.)

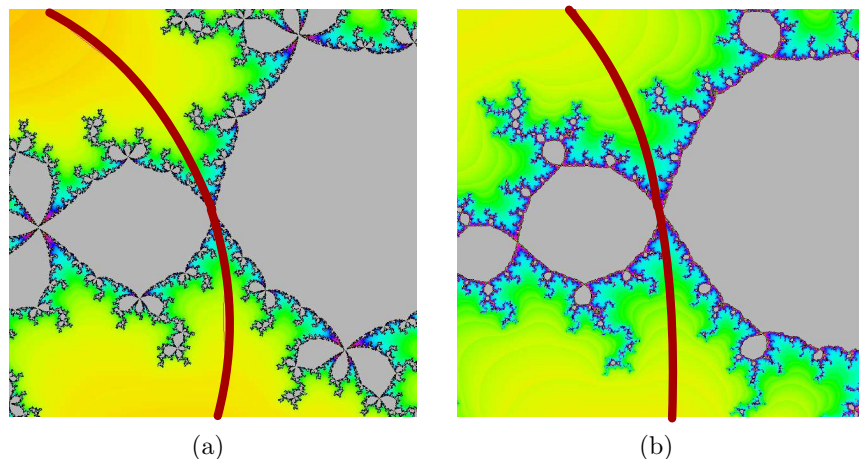


Figure 67: Another Misiurewicz example from  $\mathcal{S}_4$ , again with the dynamical picture in (a) and the parameter picture, magnified by a factor of  $ds/dt$ , in (b). In both figures, the rays of angle  $33/80$  and  $57/80$  land at the central point. In the dynamical picture, this point  $2a$  has period two. Note that  $11 \mapsto 33 \mapsto 19 \mapsto 57 \mapsto 11$  under tripling mod 80. In the parameter picture this central point lies between the “double-basilica” region above, and the 1010-region below. (Here the parameters are:  $a = -0.1996 - 0.0353i$  and  $v = 0.2284 + 1.0521i$ .)

We can make this similarity between Julia set and parameter space more explicit as follows. For  $F$  in a small neighborhood of any Misiurewicz point  $F_0 \in \mathcal{S}_p$ , it is not hard to see that there is a unique pre-periodic point  $z(F)$  which varies as a holomorphic function of  $F$ , with  $z(F_0) = 2a_{F_0}$ .

We further conjecture that the correspondence

$$F \mapsto s(F) = 2a_F - z(F)$$

is univalent throughout some neighborhood of  $F_0$ , so that  $s(F)$  provides a dynamically defined holomorphic local coordinate for  $\mathcal{S}_p$  throughout this neighborhood. Using this coordinate, we conjecture that, under iterated magnification,  $\mathcal{S}_p$  near  $F_0$  looks more and more like the dynamic plane for  $F_0$  near  $2a_{F_0}$ , without any need for a preliminary scale change and rotation.

In practice, since  $s(F)$  is defined only locally, it is more convenient to use this procedure to choose the correct preliminary scale change and rotation. This was done for Figures 66 and 67. (The computation was relatively easy since for these two cases  $2a_{F_0}$  itself is a periodic point, so that  $z(F)$  is also periodic.) For more on the study of self-similarity see [BY].)

## A Parabolic Landing Stability (in some cases)

In general, a parameter ray landing at a parabolic point will not deform continuously as we perturb the map. As an example, the zero ray for the quadratic map  $z \mapsto z^2 + 1/4$  will jump discontinuously under a small perturbation of the map. (Compare Figure 68.) Nevertheless, the actual landing point of the ray will vary continuously in the quadratic case, and for some higher degree cases.

We will say that a holomorphic one-parameter family of monic polynomial maps  $F_s$  of degree  $d > 1$  has only *one free critical point* if all but one of the critical points (if there is more than one) is periodic or eventually periodic; and if this one is a simple critical point. To simplify the notation, we will assume that the parameter  $s$  varies over some open subset of  $\mathbb{C}$ .

**Theorem A.1 (Parabolic Landing Stability Theorem).** Let  $\theta$  be an angle of period  $q$  under multiplication by  $d$ , and suppose that the dynamic ray of angle  $\theta$  for  $F_0$  lands at a parabolic point  $z_0$ . If there is only one free critical point, and if we exclude the special case where the  $\theta$  ray for  $F_s$  crashes into a critical point of  $F_s^{\circ q}$ , then the landing point for this ray varies continuously with  $s$  throughout some neighborhood of  $s = 0$ . In the exceptional case where this ray does crash into a critical point, the same statement is true for the limit rays as we approach  $\theta$  from the left or from the right. (The two limits differ; but converge to each other as  $s \rightarrow 0$ .)<sup>13</sup>

---

<sup>13</sup>This result contrasts with Douady and Hubbard's proof that repelling landing points always deform continuously under perturbation. See Lemma 2.9.

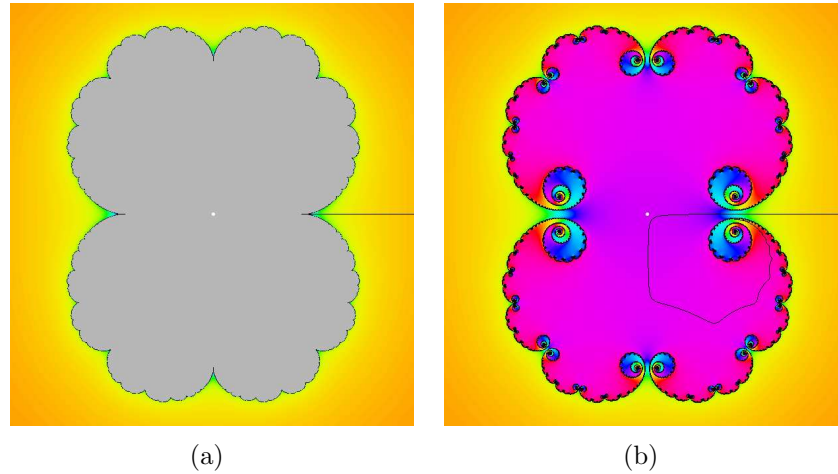


Figure 68: (a) The zero ray  $\mathcal{R}_{F_0}(0)$  for the quadratic map  $F_0(z) = z^2 + 1/4$  lands at the parabolic fixed point. (b) For suitable  $F$  close to  $F_0$ , the zero ray passes between the two fixed points, then ricochets off the critical point and off a sequence of precritical points, eventually landing on the lower fixed point.

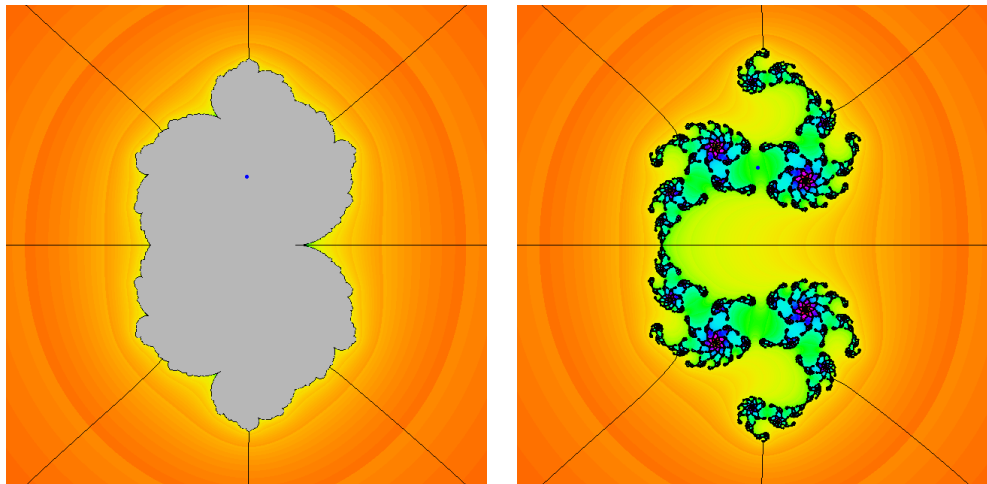


Figure 69: Julia sets for two maps in the family

$$F_s(z) = z^3 + z^2 + (1+s)z + s .$$

Note that the “one free critical point” condition is not satisfied. On the left: For  $s = 0$  the zero ray lands at a parabolic fixed point, while the  $1/2$  ray lands at a repelling fixed point. On the right, the case  $s = 0.2$ . For all  $s \geq 0$ , the two critical points are complex conjugates. For  $s > 0$  the parabolic fixed point splits into a pair of complex conjugate fixed points, and the zero ray squeezes through the gap between them to land at the same point as the  $1/2$  ray. Both critical orbits escape to infinity, so the Julia set is totally disconnected. The top critical point is marked in both figures.

Here the condition that there is at most one free critical point, or some similar condition, is essential. (See Figure 69.) For an example of the exceptional case, see Figure 70-left.

**Corollary A.2 (Upper Semi-Continuity of Orbit Portraits).** *Now suppose that the maps  $F_s$  are in  $\mathcal{S}_p$ , with degree  $\mathbf{d} = 3$ . If  $\theta$  and  $\theta'$  are periodic under tripling, and if the  $\theta$  and  $\theta'$  dynamic rays land together for maps  $F_s \in \mathcal{S}_p$  with  $s$  arbitrarily close to zero, then they land together for  $s = 0$ .*

*Proof.* This follows immediately. □

The proof of Theorem A.1 begins as follows. The angle  $\theta$ , of period  $q$  under multiplication by  $d$ , will be fixed throughout the discussion. Suppose that we have a one parameter family for which the Theorem is false. Then there exists some small neighborhood  $U$  of the point  $z_0$  and an infinite sequence of parameter points  $s_j$  converging to  $s = 0$  such that the landing point  $\hat{z}_j$  of the  $\theta$  ray  $\mathcal{R}_j$  for each  $F_{s_j}$  lies outside of  $U$ . After passing to an infinite subsequence, we may assume that these landing points converge to some point  $\hat{z} \notin U$ .

**Notations:** We will use the notation  $f_s$  for the iterate  $F_s^{\circ q}$  of degree  $\mathbf{d}^q$ . Evidently  $\hat{z}$  must be one of the finitely many fixed points of  $f_0$ . The parabolic point  $z_0$  is the root point of some number  $n \geq 1$  of parabolic basins which map to themselves under  $f_0$ . In general<sup>14</sup>  $n$  is some divisor of  $q$ , and  $z_0$  is a point of period  $q/n$  under  $F_0$ .

Let  $B$  be the union of the closures of these  $n$  basins. First note the following.

**Lemma A.3.** *The root point  $z_0$  is the only fixed point of  $f_0$  in the set  $B$ . Since  $\hat{z}$  is a fixed point not equal to  $z_0$ , it follows that  $\hat{z} \notin B$ .*

*Proof.* By a Theorem of Roesch and Yin [RY], every polynomial parabolic basin is a Jordan domain. Each of the  $n$  parabolic basins in  $B$  contains a single critical point of  $f_0$ , and hence maps onto itself with degree two. Thus each basin boundary must wrap around itself with degree two.

Let  $\Gamma$  be the boundary of one of the  $n$  parabolic basins in  $B$ . Since  $\Gamma$  is contained in the Julia set, it cannot contain any attracting points. Furthermore since  $F_0$  can have only one cycle of parabolic points, there cannot be any parabolic point other than the common root point in  $\Gamma$ . Thus we need only prove that there is no repelling fixed point in  $\Gamma$ .

If we think of  $f_0 : \Gamma \rightarrow \Gamma$  as a one-dimensional topological dynamical system, then the root point is a topologically repelling fixed point. But it is not hard to check that an orientation preserving circle map with  $k$  fixed points, all repelling, must have degree  $k + 1$ . (Each interval between two fixed points cannot map into itself, and hence must cover itself twice, and cover the rest of the circle once.) Since the degree is known to be two, it follows that  $k = 1$ ; and hence the root point is the only fixed point of  $f_0$  in  $B$ . □

Note the following statement:

Every polynomial map with a parabolic point can be approximated arbitrarily closely by a map of the same degree with disconnected Julia set.

---

<sup>14</sup>The only exception that we know is the map  $F(z) = z^3 + z$ , with  $q = 1$  but  $n = 2$ .

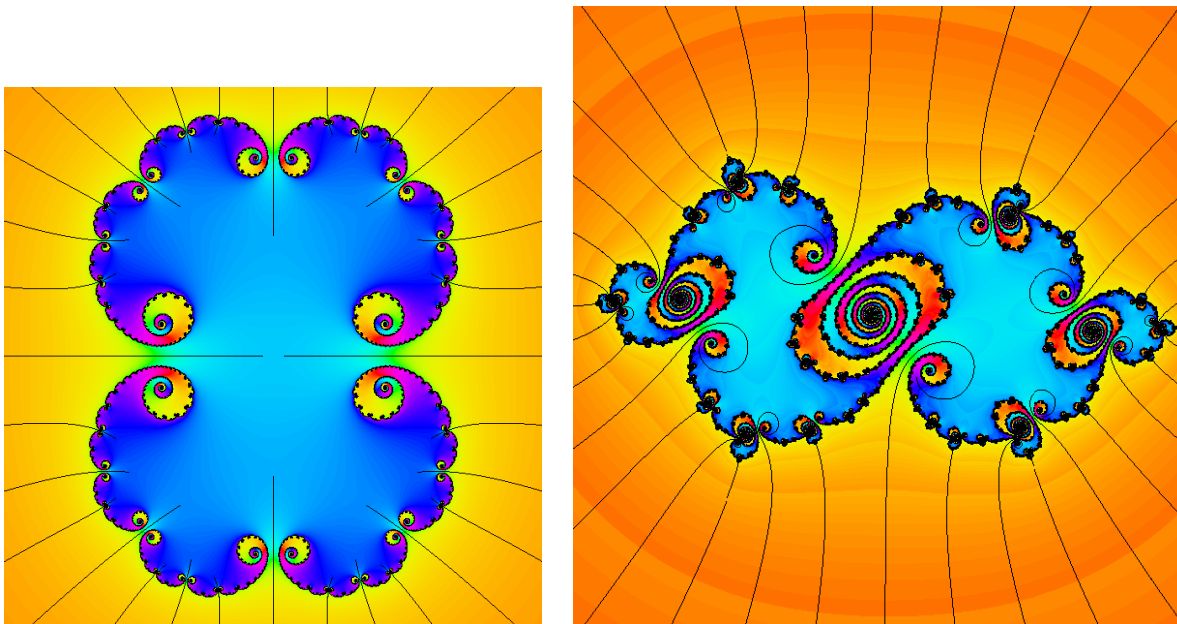


Figure 70: On the left: an approximation  $z \mapsto z^2 + 0.27$  to the standard cauliflower map. All rays of angle  $n/2^k$  penetrate from the outside into the central domain; but no rays from the inside pass to the outside. On the right: an approximation to the parabolic map  $z \mapsto z^3 - z$ , for which the  $1/4$  and  $3/4$  rays land at the central parabolic point. Again many rays from the outside penetrate to the interior; but no rays pass in the opposite direction. (The illustrated map is  $z \mapsto z^3 + (-1.00878700 + .160147 I)z + (-.097287 + .008229 I)$ .)

We are grateful to Misha Lyubich for pointing out that this follows from his paper [Ly], together with Mañé, Sad and Sullivan [MSS], and Levin [Le]. In fact it follows from these papers that the *bifurcation locus* (consisting of maps where the Julia set does not vary continuously in some neighborhood) is nowhere dense, and coincides with the closure of the set of parabolic maps. It also coincides with the set of maps which are *active*, in the sense that the family of iterated forward images of some critical point is not a normal family. A map in the connectedness locus is active if and only if its Julia set becomes disconnected under some small perturbation.

**Lemma A.4.** *Suppose that  $F$  is a small perturbation of a parabolic map  $F_0$  with a set  $B$  of parabolic basins of period  $q$ , as described above. Then there must be an angle  $\theta$  of period  $q$  under multiplication by  $d$  such that the dynamic ray of angle  $\theta$  for  $F_0$  lands at the parabolic root point, but the corresponding ray for  $F$  penetrates into the former parabolic basin, as illustrated in Figure 70. It follows that all iterated preimages of this ray under multiplication by  $d^q$  also penetrate. These preimages are everywhere dense among rays landing on  $B$ , and none of them is invariant under the action of  $F^{\circ q}$ .*

*Proof.* Since the ray is invariant under  $F^{\circ q}$ , it must either land at an  $F^{\circ q}$ -invariant point or else crash into a critical or precritical point. In either case, it must penetrate into the parabolic basin of  $F_0$ . (Compare Petersen and Zakeri [PZ].)  $\square$

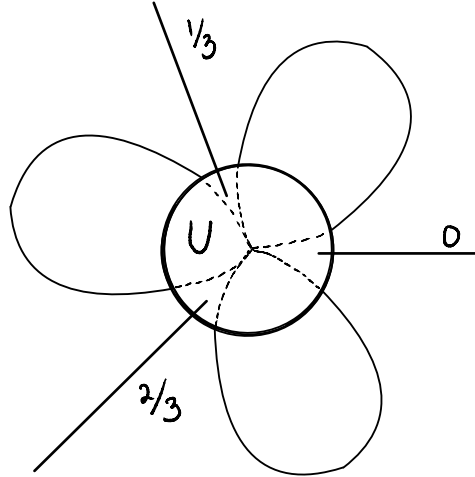


Figure 71: Cartoon of a parabolic map with rotation number  $1/3$ .

**Proof of Theorem A.1.** Figure 71 illustrates a typical example, with  $n = 3$ . Note that the  $n$  loops of  $B$  are contained in attracting petals, while the  $n$   $f_{s_j}$ -invariant rays enter through repelling petals. If  $f_{s_j}$  is close enough to  $f_0$ , then these invariant parameter rays will certainly cross into  $U$ , and must eventually land at some repelling fixed point of  $f_{s_j}$ . There are no such fixed points in  $B \setminus U$ , so if the landing point is not in  $U$  then they somehow escape from  $B$ . They certainly cannot go back out the way they came in, through one of the  $n$  repelling petals. The only other possibility is that they cross through the boundary of  $B$  in one of the  $n$  attracting petals. But this is impossible. In the limit as  $f_{s_j}$  tends to  $f_0$ , this boundary maps bijectively to itself without fixed points (other than the root point in  $U$ ). This looks impossible: If a ray first crosses out of  $B$  at a point  $b$  then it should already have crossed out previously near some pre-image of  $b$ .

Here is an alternative more explicit argument. If an  $f_{s_j}$ -invariant ray crossed from inside to the complement of  $B$ , then it would have to cross between two very close rays which are entering  $B$  from the outside, and which are moved somewhere else by  $f_{s_j}$ . This is clearly impossible; which completes the proof.  $\square$

## B Embedded Trees

By an *embedded tree* we will mean a contractible simplicial complex of dimension zero or one which is topologically embedded in  $\mathbb{C}$ . However two such trees will be regarded as completely equivalent if there is an orientation preserving homeomorphism of the plane which takes one to the other.

The (*weak*) *Hubbard tree*  $T$  of a critically finite polynomial map  $F$  is an embedded tree together with some additional structure. More precisely:

- (1) The underlying set  $|T|$  is the smallest subset of  $\mathbb{C}$  which contains all of the critical orbits, and also contains the regulated path (see [DH1] or [Po]) joining any two critical or postcritical points within the filled Julia set of  $F$ .

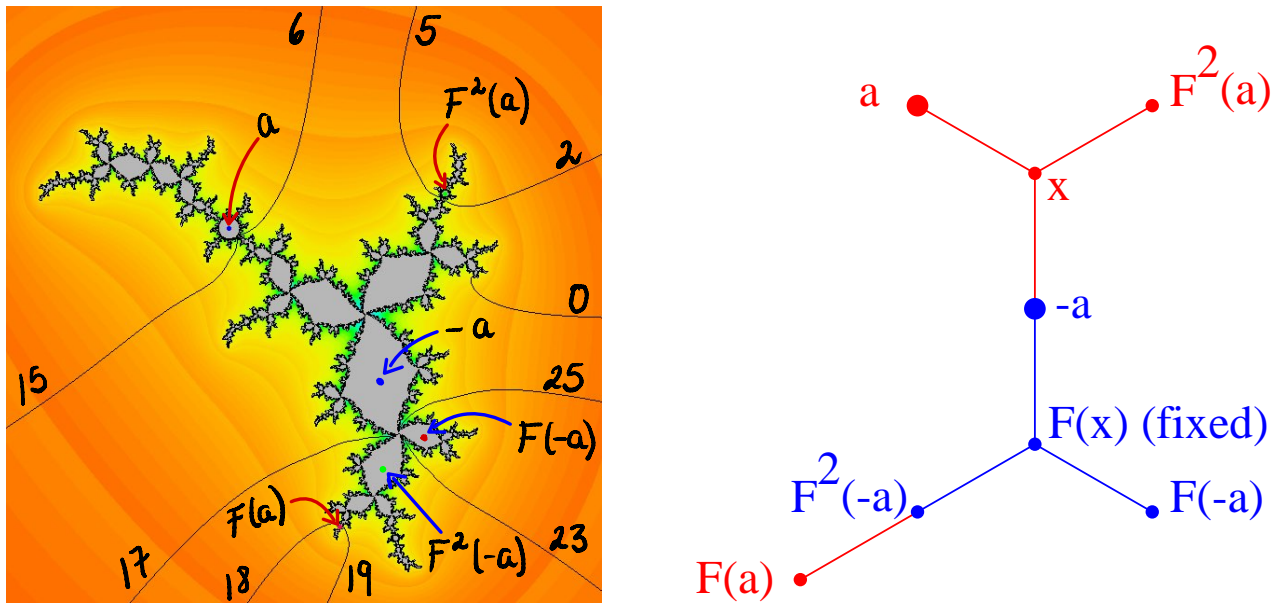


Figure 72: On the left, Julia set for the center point of the  $2/3$  limb of a Mandelbrot copy associated with the  $1/3$  rabbit. (All angles over  $26$ .) On the right, a corresponding Hubbard tree. For further discussion see Remark B.1 below.

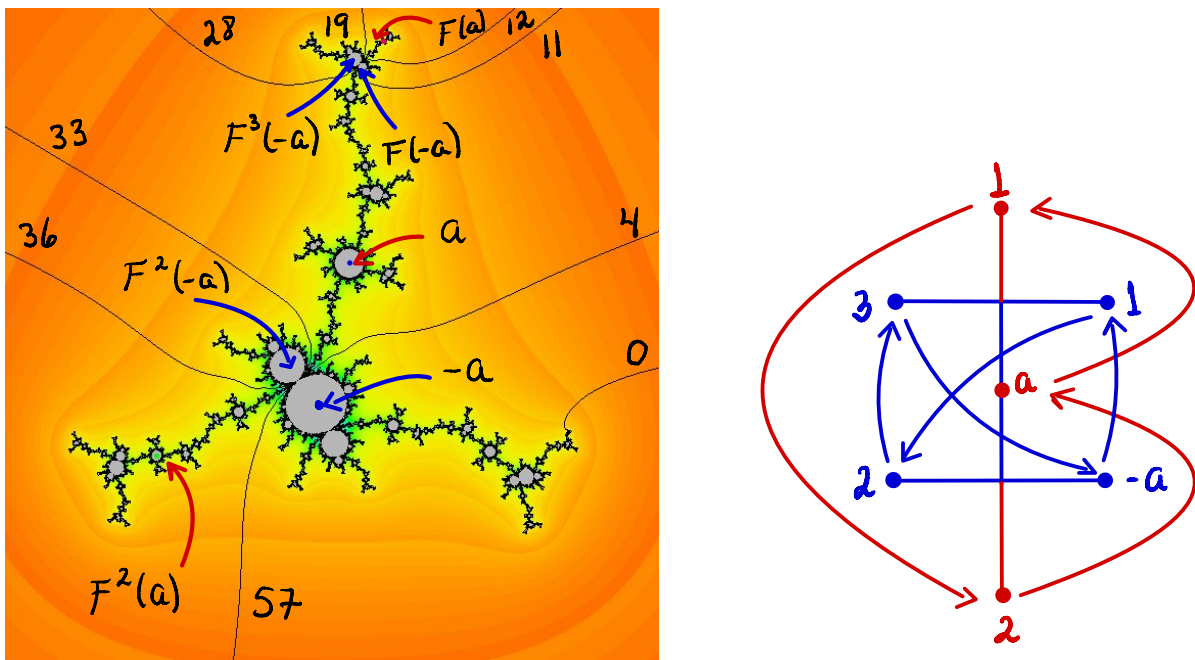


Figure 73: On the left, Julia set for the “basilica point” of a very small Mandelbrot copy in  $\mathcal{S}_3$ . (See Figure 61 in Section 4.) On the right, the corresponding Hubbard tree  $T$  is quite different from the previous one. The sub-tree  $T'$  is again colored blue. (All angles over  $80$ .)

- (2) The vertices of this tree are these critical or postcritical points, together with any branch points.
- (3) Furthermore:
  - (a) the map from vertices to vertices must be specified;
  - (b) the critical points must be labeled; and
  - (c) their multiplicity must be specified if it is greater than one.

**Note:** We are using this weak definition of Hubbard tree in order to relate maps of two different degrees. However this loses a basic property of more usual definitions (as given for example in [Po] or [M4]). This tree does not determine the map up to conformal conjugacy. For example the cubic maps  $z \mapsto z^3 + i$  and  $z \mapsto z^3 - i$  have the same weak tree, yet do not belong to the same conformal conjugacy class.

Figures 72 and 73 illustrate two examples for the tree  $T$  associated to a critically periodic point in a Mandelbrot copy. They suggest the following two statements:

1. The tree  $T'$  for the associated critically periodic point in  $\mathbb{M}$  naturally embeds as a subtree of  $T$ .
2. The “quotient”  $T/T'$  in which  $T'$  is collapsed to a point is naturally isomorphic to the tree  $T''$  for the main hyperbolic component of the copy  $M$ .

However, even if both of these statements are true, we would still be far from knowing how to construct the tree  $T$  for any given component of any Mandelbrot copy in  $\mathcal{S}_p$ .

**Remark B.1.** Here are further comments about Figures 72 and 73.

In Figure 72, the tree  $T'$  for the associated quadratic map is colored blue, while the rest of the cubic tree is colored red. Note that the blue part has rotation number  $2/3$ . If we collapse the blue part to a point, we essentially get the tree  $T''$  for the main hyperbolic component. However there is a minor technicality: When we collapse  $T'$  to a point, both vertices of the edge joining the branch point  $x$  to  $-a$  map to the same point. This is not allowed in a Hubbard tree, so we must also collapse this edge to this point. In this way we get the required tree for the principle hyperbolic component, with rotation number  $1/3$ .

## References

- [AK] M. Arfeux and J. Kiwi. *Irreducibility of periodic curves in cubic polynomial moduli space*. Proceedings of the London Mathematical Society **127** (3) (2023) 792–835. <https://doi.org/10.1112/plms.12553>

- [BH1] B. Branner and J. H. Hubbard. *The iteration of cubic polynomials part I: The global topology of parameter space*. Acta Math., **160** (1988) 143–206.
- [BKM] A. Bonifant, J. Kiwi and J. Milnor. *Cubic polynomial maps with periodic critical orbit, part II: escape regions*. Conform. Geom. Dyn. **14** (2010) 68–112. *Errata*: Conform. Geom. Dyn. **14** (2010) 190–193. (Also available in: “Collected papers of John Milnor. VII. Dynamical systems (1984–2012),” ed. A. Bonifant. Amer. Math. Soc. (2014) 477–526.)
- [BMS] A. Bonifant, J. Milnor and S. Sutherland. *Parabolic implosion and the relative Green’s function*. In preparation,
- [BM] A. Bonifant and J. Milnor. *Cubic polynomial maps with periodic critical orbit, part IV: Zero-kneading regions*. In preparation.
- [BY] A. Bonifant and B. Young. *Self-similarity of Misiurewicz maps in the cubic parameter curves*. In preparation.
- [DM-S] L. DeMarco and A. Schiff. *The geometry of the space of critically periodic curves in the space of cubic polynomials*. Exp. Math. **22** (2013) 99–111.
- [DH1] A. Douady and J. H. Hubbard. *Exploring the Mandelbrot set. The Orsay Notes* (1983). (Available in <http://www.math.cornell.edu/~hubbard/OrsayEnglish.pdf>)
- [DH2] A. Douady and J. H. Hubbard. *A proof of Thurston’s topological characterization of rational functions*. Acta Math. **171** (1993) 263–297.
- [DH3] A. Douady and J. H. Hubbard. *On the dynamics of polynomial-like mappings*. Ann. Sci. Éc. Norm. Sup. **18** (1985) 287–344.
- [EE] J.-P. Eckmann and H. Epstein. *Scaling of Mandelbrot sets generated by critical point preperiodicity*. Comm. Math. Phys. **101** (1985) 283–289.
- [H1] P. Haïssinsky. *Chirurgie parabolique*. C. R. Acad. Sci. Paris, **327** (1998) 195–198.
- [H2] P. Haïssinsky. *Déformation  $J$ -équivalence de polynômes géométriquement finis*. Fundamenta Math. **163** (2000) 131–141.
- [Ha] A. Hatcher. “Algebraic Topology.” Cambridge U. Press 2002.
- [Ka1] T. Kawahira. *Note on dynamically stable perturbations of parabolics*. **1447** Complex Dynamics, Kyoto University Research Information Repository, RIMS Kokyuroku, August (2005) 90–107.
- [Ka2] T. Kawahira. *Zalcman functions and similarity between the Mandelbrot set, Julia sets, and the tricorn*. Analysis and Mathematical Physics **10** (2020) 1–18.
- [Le] G.M. Levin. *Irregular values of the parameter of polynomial mappings*. Uspekhi Mat. Nauk SSSR **36** (6) (1981) 219–220.

- [Ly] M. Yu. Lyubich. *Some typical properties of the dynamics of rational maps*. Russian Math. Surveys **38** (5) 154–155. <https://doi.org/10.1070/RM1983v038n05ABEH003515>
- [MSS] R. Mañé, P. Sad and D. Sullivan. *On the dynamics of rational maps*. Ann. Sci. École Norm. Sup. **16** (2) (1983) 193–217. <http://eudml.org/doc/82115>
- [Mc] C. McMullen. *The Mandelbrot set is Universal*. pp. 1–17 of “The Mandelbrot Set, Theme and Variations”, London Math. Soc. Lecture Note Series **274**, Cambridge U. Press 2000.
- [M1] J. Milnor. *Hyperbolic components in spaces of polynomial maps*, with an appendix by A. Poirier. *Contemp. Math.*, **573** “Conformal dynamics and hyperbolic geometry,” Amer. Math. Soc. (2012) 183–232. (Also available in: “Collected papers of John Milnor. VII. Dynamical systems (1984–2012),” ed. A. Bonifant. Amer. Math. Soc. (2014) 527–576.)
- [M2] J. Milnor. *Periodic orbits, external rays, and the Mandelbrot set*. “Géométrie Complexe et Systèmes Dynamiques.” Astérisque **261** (2000) 277–333. (Also available in: “Collected papers of John Milnor. VII. Dynamical systems (1984–2012),” ed. A. Bonifant. Amer. Math. Soc. (2014) 171–229.)
- [M3] J. Milnor. “Dynamics in One Complex Variable.” 3rd edition, Princeton University Press, 2006.
- [M4] J. Milnor. *Cubic Polynomial Maps with Periodic Critical Orbit, Part I*. “Complex Dynamics Families and Friends”, ed. D. Schleicher, A K Peters (2009) 333–411. (Also available in: “Collected papers of John Milnor. VII. Dynamical systems (1984–2012),” ed. A. Bonifant. Amer. Math. Soc. (2014) 409–476.)
- [Po] A. Poirier. *Hubbard Trees*. Fund. Math. **208** (2010) 193–248.
- [PZ] C. Petersen and S. Zakeri. *Periodic points and smooth rays*. Conf. Geom. and Dyn. **25** (2021) 170–178.
- [RL] J. Rivera-Letelier. *On the continuity of Hausdorff dimension of Julia sets and similarity between the Mandelbrot set and Julia sets*. Fund. Math. **170** (2001) 287–317.
- [RY] P. Roesch and Y. Yin. *The boundary of bounded polynomial Fatou components*. C. R. Math. Acad. Sci. Paris **346** (2008) 877–880.
- [Sch] D. Schleicher. *Rational external rays of the Mandelbrot set*. Asterisque **261** (2000) 405–443.
- [Si] J. H. Silverman. *An algebraic approach to certain cases of Thurston rigidity*. Proc. of the Amer. Math. Soc. **140** (10) (2012) 3421–3434.

- [Sp] E. Spanier. “Algebraic Topology”, McGraw-Hill, 1966.
- [TL] Tan\_Lei. *Similarity between the Mandelbrot set and Julia sets*. Comm. Math. Phys. **134** (1990) 587–617.

## List of Figures

1	Dynamic plane for a map $F \in \mathcal{E}_h$ . . . . .	5
2	Julia set for the landing map of the zero parameter ray in the “basilica” escape region of $\mathcal{S}_2$ . . . . .	6
3	Parabolic example of period one. . . . .	8
4	Perturbed figure 3. . . . .	9
5	A Misiurewicz example. . . . .	10
6	Simpler Misiurewicz example. . . . .	10
7	Julia sets showing rays crashing together . . . . .	13
8	The standard cauliflower . . . . .	13
9	Julia parabolic map in $\mathcal{S}_3$ . . . . .	16
10	Mandelbrot set showing some critically periodic points . . . . .	18
11	Small Mandelbrot copy in $\mathcal{S}_3$ with walls . . . . .	20
12	Detail of $\mathcal{S}_3$ . . . . .	24
13	Julia sets for a Type A component and the attached Type D components. . . . .	24
14	A weakly self-dual Julia set of Type B (2, 2) . . . . .	25
15	$\mathbf{Tes}_1(\overline{\mathcal{S}}_2)$ . . . . .	28
16	Four parabolic maps in $\mathcal{S}_2$ . . . . .	30
17	$\mathbf{Tes}_2(\overline{\mathcal{S}}_2)$ . . . . .	31
18	Cartoon of $\mathbf{Tes}_2(\overline{\mathcal{S}}_2)$ . . . . .	32
19	Pictures of $\mathbf{Tes}_1(\overline{\mathcal{S}}_1)$ and $\mathbf{Tes}_2(\overline{\mathcal{S}}_1)$ . . . . .	33
20	Pictures of $\mathbf{Tes}_3(\overline{\mathcal{S}}_1)$ . . . . .	33
21	Julia set of parabolic map in $\mathcal{S}_2$ , with kneading walls. . . . .	34
22	Part of the parameter curve $\mathcal{S}_5$ . . . . .	35
23	Julia set for Figure 22 . . . . .	36
24	Bottom part of $\mathcal{S}_1$ and top left of $\mathcal{S}_2$ . . . . .	38
25	Julia sets for maps in $\mathbf{Tes}_5(\overline{\mathcal{S}}_5)$ of components in Figure 22 . . . . .	41
26	Julia sets in parameter rays $11/24 \pm \epsilon$ . . . . .	42
27	Julia sets on parameter rays $7/12 \pm \epsilon$ . . . . .	42
28	Detail of Figure 27 . . . . .	49
29	Julia for a Misiurewicz map $F$ in $\mathcal{S}_1$ . . . . .	51
30	Period 3 orbit portraits of $\overline{\mathcal{S}}_3$ between 010– and airplane . . . . .	52
31	$\mathbf{Tes}_1(\overline{\mathcal{S}}_3)$ . . . . .	53
32	Part of period one tessellation of $\mathcal{S}_3$ . . . . .	53
33	$\mathbf{Tes}_2(\overline{\mathcal{S}}_3)$ . . . . .	54
34	Part of period two tessellation of $\mathcal{S}_3$ . . . . .	54

35	$\mathbf{Tes}_3(\overline{\mathcal{S}}_3)$ . . . . .	57
36	Part of period three tessellation of $\mathcal{S}_3$ . . . . .	57
37	$\mathbf{Tes}_3(\overline{\mathcal{S}}_3)$ -airplane . . . . .	58
38	Orbit portraits top right quadrant airplane region in $\mathbf{Tes}_3(\overline{\mathcal{S}}_3)$ . . . . .	59
39	Cartoon for the Two Ray Case . . . . .	61
40	Copy of Type M (5, 3) which lies <i>along</i> the boundary between the 010- region	61
41	Cartoon of the 3 ray case . . . . .	62
42	Little Mandelbrot copy of period $q = 5$ which lies in a primary wake in the airplane region of $\mathcal{S}_3$ . . . . .	64
43	Julia set for 3-ray case between the 110 and 010- regions of $\mathbf{Tes}_3(\overline{\mathcal{S}}_3)$ . .	64
44	3-ray case in part of $\mathbf{Tes}_4(\overline{\mathcal{S}}_4)$ . . . . .	65
45	Cartoon illustrating an adjacent pair of 3-ray triples, satisfying condition (1). . .	66
46	Cartoon illustrating two adjacent escape regions with 3-ray triples, satisfying con- dition (3). . . . .	66
47	A-centered face . . . . .	68
48	Angular distances around an A-centered face . . . . .	69
49	B-centered face . . . . .	71
50	off-center A component . . . . .	72
51	Off-center B component . . . . .	73
52	Cartoon of 4-ray case . . . . .	73
53	Orbit portrait as parabolic point splits into a pair of periodic repelling points	75
54	Detail of the 1/3-rabbit region in $\mathcal{S}_3$ . . . . .	76
55	Part of $\overline{\mathcal{S}}_4$ . . . . .	77
56	Two rings . . . . .	77
57	Cartoon illustrating the ring around the 1/4-rabbit region in $\mathcal{S}_4$ . . . . .	78
58	Angles and grand orbits for Figure 56-left, with notation as in Figure 57. . . . .	78
59	On the left: two four ray points separated by an A component. On the right: separated by a B component . . . . .	79
60	Julia set for the root point of an A component in a 1/3-rabbit, with angles modulo 78, illustrating the tables above. . . . .	81
61	Period 4 orbit portraits for Mandelbrot copy across the boundary between 010+ and airplane region . . . . .	83
62	Small Mandelbrot copy of period 4 between the airplane and 100+ regions in $\mathcal{S}_3$ . . . . .	84
63	Two transverse curves . . . . .	88
64	Graph of the ratio $\mathbf{d}_p/N_p$ as a function of $p$ . . . . .	92
65	Parameter space and Julia set for a Chebyshev map in $\mathcal{S}_2$ . . . . .	93
66	External rays in Julia set and parameter space for a Misiurewicz map . . . . .	94
67	Misiurewicz example from $\mathcal{S}_4$ in both dynamical and parameter planes . . . .	94
68	Pictures of the zero ray $\mathcal{R}_{F_0}(0)$ for the quadratic map $F_0(z) = z^2 + 1/4$ and for $F$ close to $F_0$ . . . . .	96
69	Julia sets for two maps in the family $F_s(z) = z^3 + z^2 + (1 + s)z + s$ . . . .	96
70	Approximation to the standard cauliflower map . . . . .	98
71	Cartoon of a parabolic map with rotation number 1/3. . . . .	99

72	Julia set for the center point of the $2/3$ limb of a Mandelbrot copy associated with the $1/3$ rabbit and a corresponding Hubbard tree . . . . .	100
73	Julia set for the basilica point . . . . .	100

Araceli Bonifant  
Mathematics Department,  
University of Rhode Island,  
Kingston, R.I., 02881.  
e-mail: bonifant@uri.edu

John Milnor  
Institute for Mathematical Sciences,  
Stony Brook University,  
Stony Brook, NY. 11794-3660.  
e-mail: jack@math.stonybrook.edu